NTNU
Norwegian University of
Science and Technology

# Energy Efficient Monitoring using Kalman Filter

A case study on environmental variables
collected from solar panels

Anne-Line Evenstad Dahlen

Master of Science in Physics and Mathematics
Submission date: June 2018
Supervisor: Jo Eidsvik, IMF

Norwegian University of Science and Technology
Department of Mathematical Sciences

# Preface

This thesis concludes my final part of studies at the Norwegian University of Science and Technology (NTNU) in the field of applied mathematics. The work was carried out during spring 2018 at the Department of Mathematical Science.

I would like to express my gratitude towards my supervisor, Jo Eidsvik, for our weekly meetings and beneficial discussions. The support has been really valuable, and it has been truly nice to know that all sorts of questions are welcomed.

The problem description was developed in collaboration with Jo and with great assistance from Frank Alexander Kraemer, that also provided with the solar panel data from NTNU. I would like to thank Frank for his provision with domain knowledge on sensors and their application. The joint meetings were really helpful as he provided with an additional angle on encountered problems.

It is with mixed feelings I submit this thesis, marking an important achievement and closure of my student life. Nevertheless, I am ready to endeavour the next chapter!

Trondheim, June 2018
*Anne-Line Evenstad Dahlen*

# Abstract

An Internet of Things (IoT) environment uses information gathering and sharing to draw conclusions, make decisions and predict future occurrences. The technology connects devices such as mobile phones and sensors in private homes and elsewhere into a network of communication with joint operational purpose. Continuously collecting information is often infeasible due to factors such as sensor-availability, memory capacity and power efficiency. Decision making within the IoT network is however based on accurate variable information and a reduction in the measurement frequency must be done thoughtfully. Additionally, a system with battery-powered devices that simultaneously harvest energy from the environment by e.g. solar panels can contribute with surplus energy to the IoT network. Continuous measurements would limit the accumulated energy contribution, and we therefore seek to replace the measurements by predictions, allowing greater accumulated energy surplus to be transferred.

This thesis presents solutions for making energy efficient data collection from solar panels with battery-powered sensors by applying a monitoring algorithm. Decisions within the algorithm are based on event- and self-triggering controls by looking at the value contribution at each data-collecting time step. Energy surplus is measured as the accumulated effort to avoid battery discharge, and prediction accuracy is computed as a joint probability where uncertainty increases with the consecutive number of predictions. A multivariate Seasonal Autoregressive Moving Average (SARMA) model is fitted with temperature and humidity data collected from solar panels at NTNU and transformed to a state space representation. The conversion is used to obtain predictions from a multivariate Kalman filter, which is an approach to on-line filtering and prediction problems. Because there are two objectives to be satisfied, a multicriteria constraint with weighted average on prediction accuracy and energy surplus is applied to analyse the performance. After monitoring, a trade-off between the objectives is needed, since, the result depends on the decision makers preference, which could be either to have confident data collection or high amount of accumulated energy surplus.

# Sammendrag

Et tingenes internett (IoT) system bruker informasjonsinnhenting og -deling til å trekke konklusjoner, ta avgjørelser og forutsi fremtidige hendelser. Denne teknologien forbinder enheter som mobiltelefoner og sensorer i og utenfor private hjem i et kommunikasjonsnettverk med et felles operasjonelt mål. Kontinuerlig datainnhenting er begrenset av faktorer som sensortilgjengelighet, lagringskapasitet og strømforsyning. Fordi beslutningstaking i IoT-systemet baserer seg på nøyaktig variabel-informasjon, må en reduksjon i målefrekvens være gjennomtenkt. Et batteridrevet system som henter inn energi fra omgivelsene som f.eks. solceller kan i tillegg bidra med overskuddsenergi til IoT-nettverket, men kontinuerlig måling begrenser det akkumulerte energibidraget. Det er dermed ønskelig å erstatte målinger med prediksjoner, slik at et større energioverskudd kan overføres.

Denne masteroppgaven presenterer løsninger for å etablere energieffektiv datainnsamling fra solcellepaneler med batteridrevne sensorer ved å anvende en overvåkningsalgoritme. Avgjørelser i algoritmen er basert på hendelses- eller selvbestemte triggerpunkter og ser på verdibidraget ved hvert tidssteg i datainnsamlingen. Energioverskudd er målt som akkumulert energibidrag til nettverket uten batteriutladning, og prediksjonsnøyaktighet beregnes som en simultan sannsynlighet hvor usikkerheten øker med antall etterfølgende prediksjoner. En multivariat sesongavhengig Autoregressive Moving Average modell er tilpasset innhentet data om temperatur og luftfuktighet fra solceller på NTNU, og konvertert til en tilstandsromrepresentasjon. Transformasjonen blir så anvendt av et Kalmanfilter som er en metode for å filtrere og predikere under overvåkningen. Fordi det er to målsettinger som skal tilfredsstilles anvendes et multikriterie med vektet gjennomsnitt på prediksjonsnøyaktighet og energioverskudd for å analysere oppførselen til systemet. Etter overvåkningen er det behov for å gjøre en avveining, hvor det er en beslutningstaker som vil bestemme om det er ønskelig med sikker datainnsamling eller høyt akkumulert energioverskudd.

# Contents

# List of Tables

# List of Figures

Chapter 1

# Introduction

Internet of Things (IoT) is an emerging technology that tries to connect the knowledge we have of the physical world into an internet-based information architecture (Teixeira et al., 2011). The goal of such a system is to make the different parts of the IoT architectures interact and communicate with each other, so they mutually can build a better understanding of the system as a whole, and operate towards a common goal. This characterisation of IoT as a sensor-based system collecting information is the principle used daily by most of our electrical equipment that is connected to the Internet. Ideally we would like to collect information continuously and extract knowledge from all of the gathered data. However, collecting data continuously could be infeasible because of constraints on memory and power (Bandyopadhyay and Sen, 2011). The latter will commonly be connected to energy consumption and thus, collecting data will also be related to power expenses. A solution to this problem could be to collect, analyse and store information, as an on-line monitoring approach, where a decision maker can decide whether to continue gathering more information or postpone the collection until later (Eidsvik et al., 2017). In this context, monitoring means a process that collects, observes and checks the performance or quality of a system over a period of time.

Considering battery-powered devices, much effort has been made to accomplish efficient usage of energy in batteries, in order to support an enduring operation. One approach is to explore the possibility of harvesting energy from the environment, where solar cells is an example of a harvesting node that can be used (Kansal et al., 2007). Including a sensor network with several nodes would impact the energy usage and workload in the total system. Thus, a power management system designed with a specified goal, to minimise the energy consumption, is important to satisfy constraints to the system (Sinha and Chandrakasan, 2001).

One practical example where energy monitoring can be applied is with employment of IoT in private homes. Such homes become smart when allowing intelligent automatic administration of collected analysed data. This could improve the living conditions with categories such as room brightening and thermal comfort (Al-Kuwari et al., 2018). Figure 1.1 presents the principle behind a simple smart house where environmental information on temperature

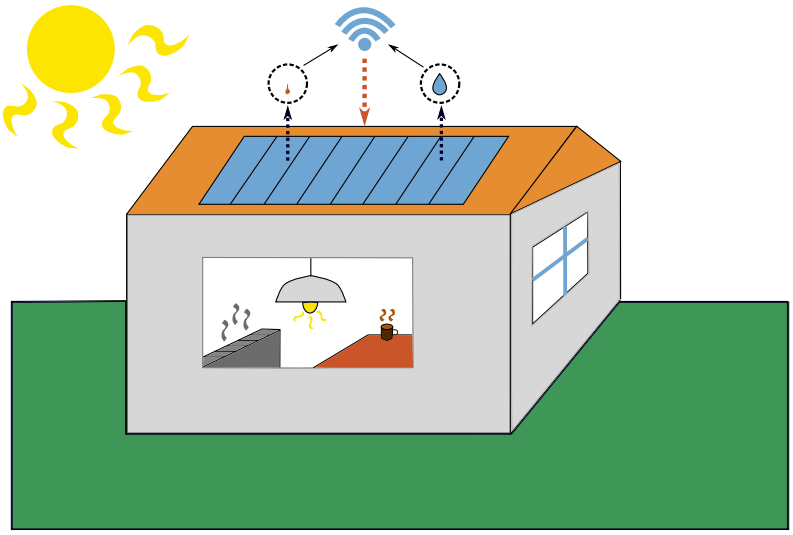

**Figure 1.1:** Smart house with roof-mounted solar panels. Information, such as temperature and humidity, collected into a cloud by the solar panels, is analysed and used to optimise the indoor environment by adjusting heating and lighting.

and humidity is collected and the battery percentage in the solar panel is charged by sunlight. Information is collected based on triggering events and shared in a cloud that further decide where to apply this knowledge. Hence, with the collected information on energy surplus and environmental information, heating and brightening within the house can be arranged. Based on the two presented goals, restricting data collection and requiring efficient use of energy, it is important to have a model to consider the value of information that is collected and how this can help us to plan ahead and draw conclusions about the future (Eidsvik et al., 2015).

In this thesis temperature and humidity data have been collected from a solar panel stationed in Trondheim. Based on these observations a model has been fitted and used to draw conclusions about future temperature and humidity, in addition to acquire the greatest amount of energy surplus from the solar panels. The predictions have been applied to the principles of event- and self-triggered control presented by Heemels et al. (2012). The triggering is established with respect to goals that can be interesting to certain industries and technology equipment such as health care services (Xu et al., 2014) or smart houses, which is from the basis for the principles of IoT explained by Weber and Weber (2010). The problem that will be addressed in this thesis is to find methods that restrict devices from repeatedly linear savings, collect data when needed, and transfer energy surplus to other instances.

The implemented on-line monitoring model with the event- and self-triggering control is built on predictions that have been computed from estimation and filtering methods. Grosswindhagera et al. (2011) propose the Kalman filter as one efficient way of predicting time series data. These processes have to be represented on a multivariate state space form as both humidity and temperature observations are considered. Hence, in this thesis a multivariate Seasonal Autoregressive Moving Average (SARMA) model have been adapted to the observations from the solar panels in Trondheim and phrased into state space representation.

Firstly the background and a brief analysis of the data will be presented in Chapter 2 and 3. Then the theory behind multivariate SARMA models and how to select appropriate values in the models is presented in Chapter 4. This chapter also presents the fitted model to the temperature and humidity observations. The motivation behind this project was primarily to find smart and efficient methods of on-line monitoring. Though, to arrive at this, the theory and approach of predicting humidity and temperature observations have to be presented. After this presentation, Chapter 5 describes the Kalman filter, seasonal Kalman filter, and how to define a bivariate seasonal Kalman filter. Chapter 6 present two different objectives with respect to *i)* energy surplus and *ii)* prediction accuracy. The objectives have been combined into a multicriteria optimisation problem with a weighted average. Three instances with distinctive event- and self-triggering situations based on how the objectives are weighted will be presented before testing to find an optimal solution with both constraints fulfilled. Finally, the project is wrapped up in Chapter 7 with closing remarks around the performance of the models and filtering methods. Some ideas for further investigation will also be considered.

Chapter 2

# Background

Data are collected from Libellium Waspmotes Solar panels placed at the rooftop at the Norwegian University of Science and Technology (NTNU) in Trondheim. The solar panels are pointing in two different directions, north and south, and have in total 8 solar panels conducting measurements. For clarity, the solar panels are merged together and form one data set, respectively for their direction. Thus, when talking about different solar panels it means either solar panels facing north or south. Figure 2.1 presents a picture of how the solar panels are placed and how they look like. During operation the solar panels are exposed to real weather conditions such as temperature, humidity and pressure, and the panels have sensor nodes providing data on the mentioned weather conditions as well as energy-related variables such as battery status on the panels. The data are measured irregularly over a 9-10 month period ending in January 2018.

The raw data variables will first be presented by exploring the distribution of number of


**Figure 2.1:** Picture of the north- and south-facing solar panels placed at the rooftop at NTNU. Photo courtesy of Frank Alexander Kraemer.

observations and correlations between some of the variables. The analysis and processing is conducted in R with developed source code for this particular instance. Information and observations obtained from the raw and processed data from NTNU is presented in this chapter and in Chapter 3.

## 2.1 Variables

The raw data variables that will be investigated further in this thesis are temperature, humidity, pressure and battery percentage. Temperature and pressure are measured in °C and atm respectively. The two other variables are measured as a ratio presented as a percentage. Relative humidity explains the ratio of water vapour in the air compared to the maximum possible concentration and battery percentage indicate the battery status where $100\%$ is a fully charged battery.

Table 2.1 presents summary statistics of the variables with data collected in September. The computed mean and standard deviation for both panels are deviating from each other with little consistency. The difference in standard deviation for temperature is only about $1°$C, while higher for the other variables.

**Table 2.1:** Presenting computed average $\mu$ and standard deviation $\sigma$ for the variables with data measured in September. Here index with 1 is computed for data observed at the north-facing panel while 2 are for the south-facing.

| Variable | Unit | $\mu_1$ | $\mu_2$ | $\sigma_1$ | $\sigma_2$ |
|---|---|---|---|---|---|
| Temperature | [°C] | 13.07 | 13.22 | 4.29 | 3.21 |
| Relative Humidity | [%] | 61.89 | 70.90 | 25.40 | 17.14 |
| Pressure | [atm] | 88196.59 | 100631.60 | 31153.64 | 1472.22 |
| Battery | [%] | 52.96 | 90.64 | 14.35 | 8.30 |

The minimum temperature in September is calculated to be $0°$C and $5.36°$C for north- and south-facing panels respectively. The temperature calculations from September are not coherent with the weather statistics from The Norwegian Meteorological Institute and NRK (2018) as minimum observed temperature in September is above $5°$C. Similarly, the calculated minimum humidity in September is $0\%$ and $34.47\%$ for north- and south-facing panels. Normal behaviour for relative humidity during a day is between $50 - 100\%$, and $0\%$ would mean that there is no water in the air which is not possible (Smith et al., 2018). From these observations and the irregularities observed in Table 2.1 it appears that the raw data contains some values with abnormal behaviour.

## 2.2 Visualising Data

During an operational time of a year, the north- and south-facing solar panel have large differences on number of observations. The north-facing panel have measured observations $92502$ times while the south-facing panel have measured $180486$ times. The distribution of the number of measurements in the respective solar panels for each month is presented in Figure 2.2. It can be seen that observations are more frequent in months that normally have higher temperatures. Because the solar panels are rotated in opposite directions it is expected that the two of them will have some differences in the number of observations. Differences are especially notable during winter when temperature is lower. One explanation could be the consumption of solar energy which during the winter will be higher towards south, because of decreased hours of daylight and how much the sun has risen. From Figure 2.2 it can be seen that the number of observations in June and July are almost the same for both panels. The total number of observations for these months are $45649$ and $48596$ for the north- and south-facing panels respectively. Thus, it can be presumed that measurements mostly have been conducted at the same time.

It is known that the battery may discharge at extreme temperatures (Waspmote Technical Guide v7.6, 2018). Figure 2.2 shows that the number of measurements in colder months are less than warmer months, and it can be assumed that operating the sensors at such times is more difficult. Nevertheless, it is still important to have information about the environment and to save battery until needed. One of the trigger points in this thesis are chosen with respect to the prediction accuracy and to get enough information about boundary observations. Therefore, the month that will be studied further in this project are the coldest month with enough observations. The number of observations in September are above $10000$ for both stations and is thus the most preferred month to look further into.

Figure 2.3 presents the distribution of the number of observations during September, with Figure 2.3a and 2.3b as observations respectively in the north- and south-facing panels. Ob-

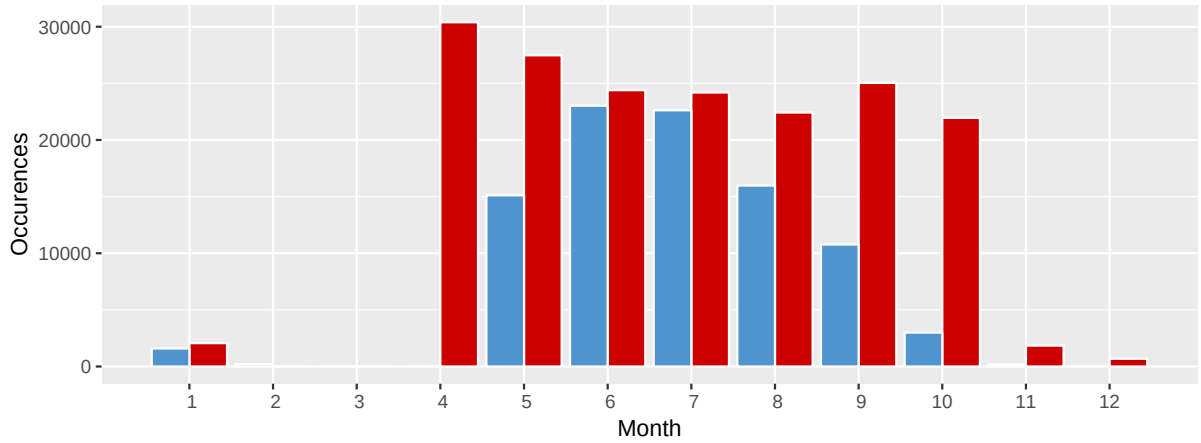


**Figure 2.2:** Data from north and south Waspmote are plotted with the number of occurrences in each month. South is plotted in red while north in blue.

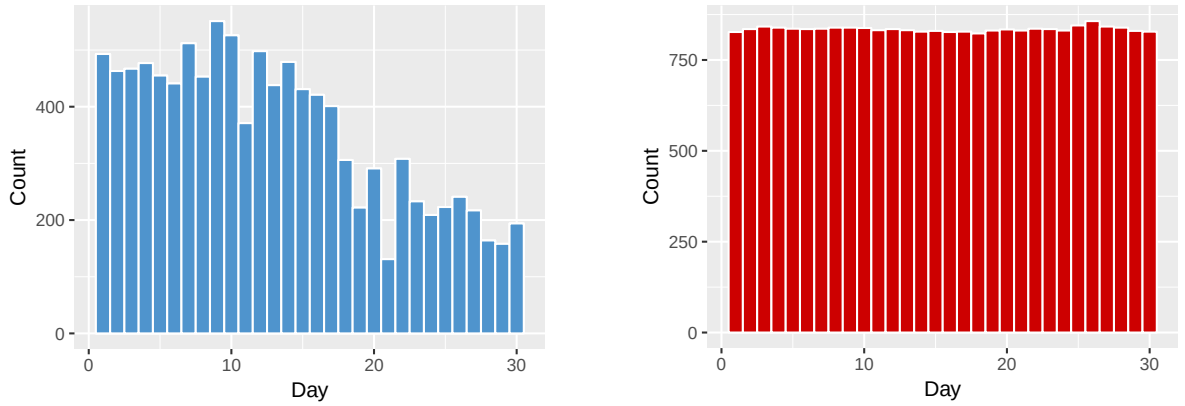


**(a)** **(b)**

**Figure 2.3:** Number of occurrences of data points in September each day, where **(a)** is from the north-facing solar panel while **(b)** is the south-facing solar panel.

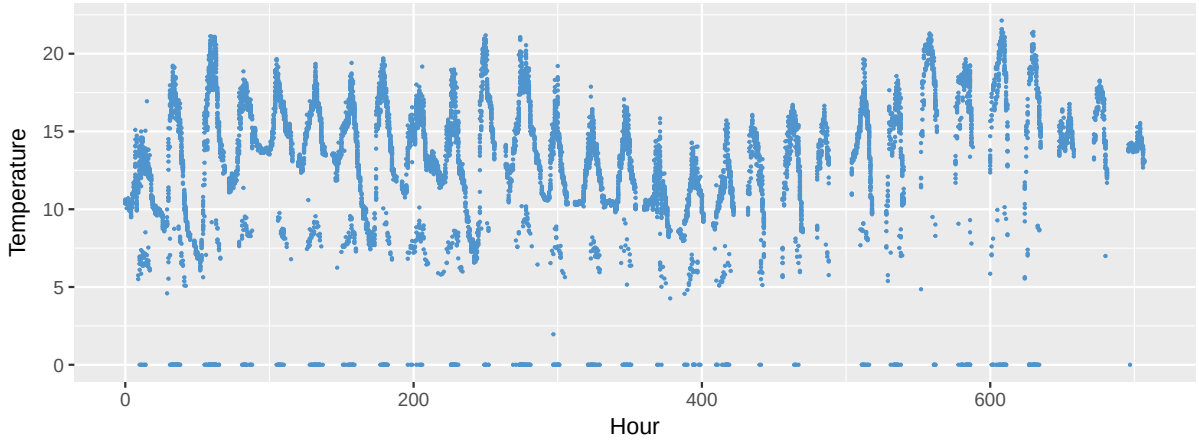


**(a)**

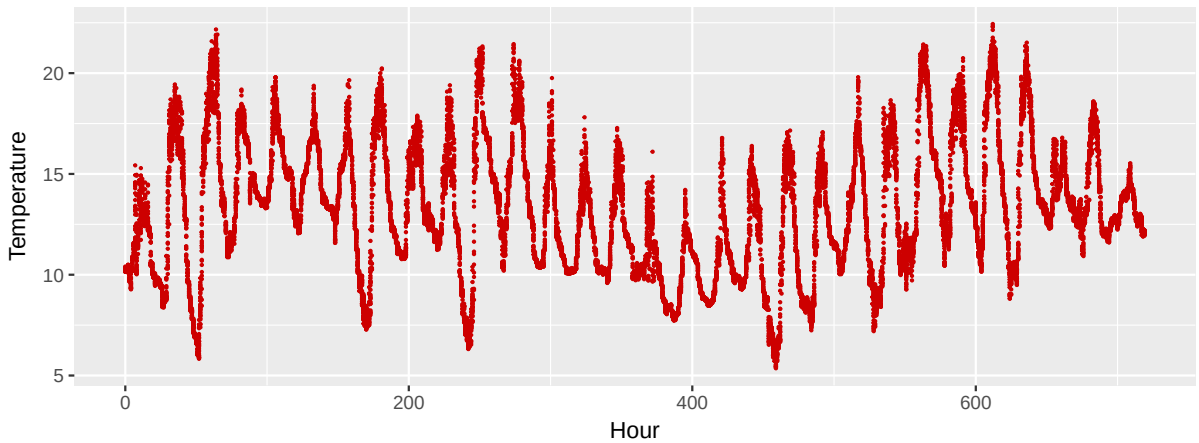


**(b)**

**Figure 2.4:** Temperature data from Waspmotes are plotted hourly for observations collected in September. North-facing solar panel, here **(a)**, is plotted in blue and south-facing panel, here **(b)**, is plotted in red. Number of observations are respectively with 10774 and 25040.

servations in the south-facing panel are uniformly distributed with more than 750 observations each day, while the number of observations in the north-facing panel have a general diminishing trend finishing below 200 observations at the final day. The total number of observations during this month are 10774 for the north-facing panel and 25040 for the south-facing panel. Because of the large number of observations and also the difference in the number of observations, visualising the collected data at each solar panel are presented in separate figures. Figure 2.4 present the performance in September, with the north- and south-facing solar panels plotted in Figure 2.4a and 2.4b respectively. The temperature data is plotted hourly for 720 hours, meaning, if there are multiple observations conducted during an hour then the observations are plotted at the same hour with their respective temperature. It can be seen that observations from the north-facing solar panel have more noise as there are oscillations between each measurement. In addition to reaching 0°C several times there are also some observations forming a shadow below the leading trend of the data. The remark from Figure 2.3a with the reduced number of observations in the end of September is confirmed in Figure 2.4a as observations are sparsely distributed. However, generally both sensors have the same behaviour when only looking at the observations following the superior trend in Figure 2.4a. Figure 2.4b does not include temperature observations below 5°C. Thus, there are some inconsistency with the raw data, which also was stated from Table 2.1.

In addition to temperature, Table 2.1 also presents the variables humidity, pressure and battery percentage. To see how these variables interact with each other their correlations with observations from September are computed and visualised in Figure 2.5. Interestingly the correlations from both solar panels are quite different from each other and have dissimilar size of correlation. Some are also correlated with inverted sign. One important remark is that the correlation with humidity and temperature is insignificant in the north-facing solar panel, while south-facing has a considerable correlation between these variables.

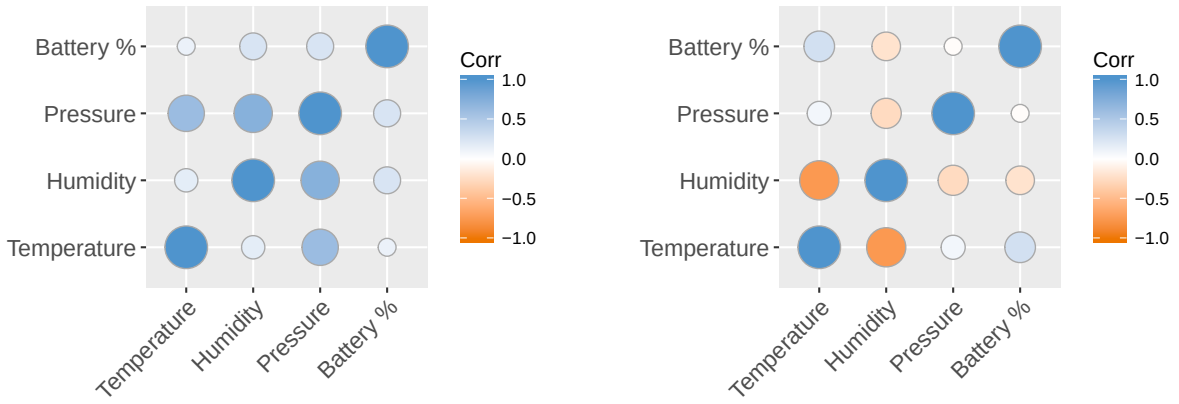


**Figure 2.5:** Correlation between temperature, humidity, pressure and battery percentage with all of the data collected in September. Here **(a)** is from the north-facing solar panel while **(b)** is collected from the south-facing solar panel.

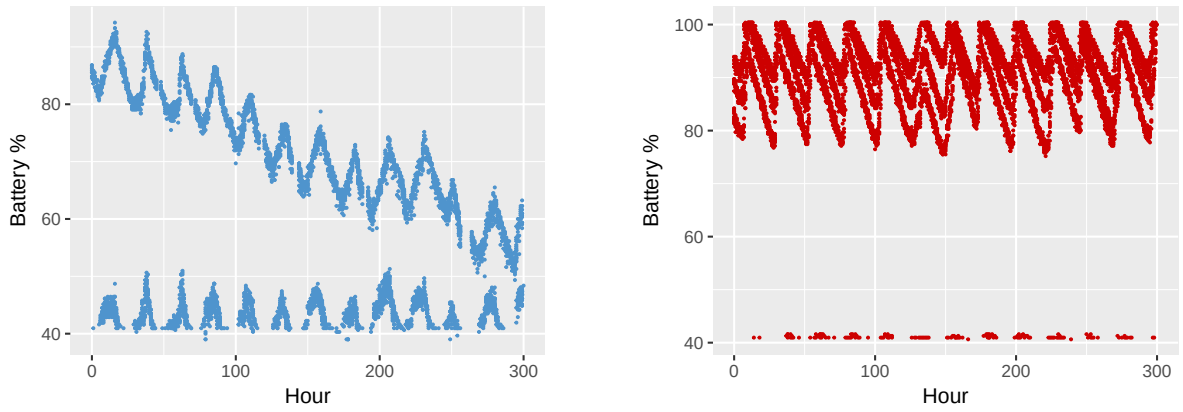


**(a)** **(b)**

**Figure 2.6:** Battery percentage for the 300 first hours of data collected in September. Here **(a)** is from the north-facing solar panel while **(b)** is the south-facing solar panel.

The data measured in September is obtained from solar panels which are solely operated on battery recharged by the environment. Behaviour of the battery percentages measured at the first $300$ hours in September for both panels are presented in Figure 2.6. In Figure 2.6b the percentage is increasing and decreasing almost like a sine wave. While in Figure 2.6a, the wave is also linearly declining. The seasonal trend seen for both batteries correspond to when the battery is charging or the system is consuming energy. In addition, the observed battery percentages for both solar panels have several instances of oscillations reaching battery percentage at $40\%$.

In Table 2.1 it was pointed out that computed mean and variance from both solar panels are deviating from each other. Additionally, the variance for all variables is too large to be realistic. When visualising data from the north- and south-facing solar panels it appears to include unreasonable observations with inconsistent correlations. Therefore, the measured data will be adapted into a processed data set that can be used further in the monitoring. In the following chapter some data analysis and adjustment to the data will be conducted.

Chapter 3

# Data Analysis

Before advancing into model adaption and on-line monitoring it is necessary to perform some analysis and modification on the data. First of all, it is essential to diminish the variance for all variables which will be obtained by removing outliers and errors. Secondly, sensor data from both solar panels should be consistent as this verifies the environmental information.

Moreover, it is useful to have one observation each hour which is achieved by interpolating in the processing step. As a result of this adaption and the information acquired previously, the data that will be used further is comparable with the observations from the solar panels.

## 3.1 Processing Data

The aim of processing the data set is to develop a multivariate sequence with observations every hour explaining the behaviour of the variables as good as possible. It was presented in Figure 2.4a that there are variations between the observations. When comparing temperature data from both solar panels in Figure 2.4, observed maximum temperature is consistent between the panels. Thus, the misgiving observations around $0°$C in the north-facing solar panel should be removed in the processing.

Additionally, when studying frequencies of observations during a day, the number of observations appeared to decrease towards the end of the month. Figure 3.1 presents the number of observations for respectively the $10$th and $20$th of September. While Figure 3.1a have at least one observation each hour, Figure 3.1b reveals that some hours lack observations. Thus, it appears that there is a need for some interpolation to complete the hourly sequence of observations.

The implemented method to construct the processed data set, looks at the first four observations in each hour and chooses the highest measured temperature. If the number of observations is less than four, it chooses the highest of the accounted temperatures. This method is a result of the observations from Figure 2.4a with temperatures at $0°$C and observations shadowing the superior trend. However, if there is no observations at a given hour this is constructed using lin-

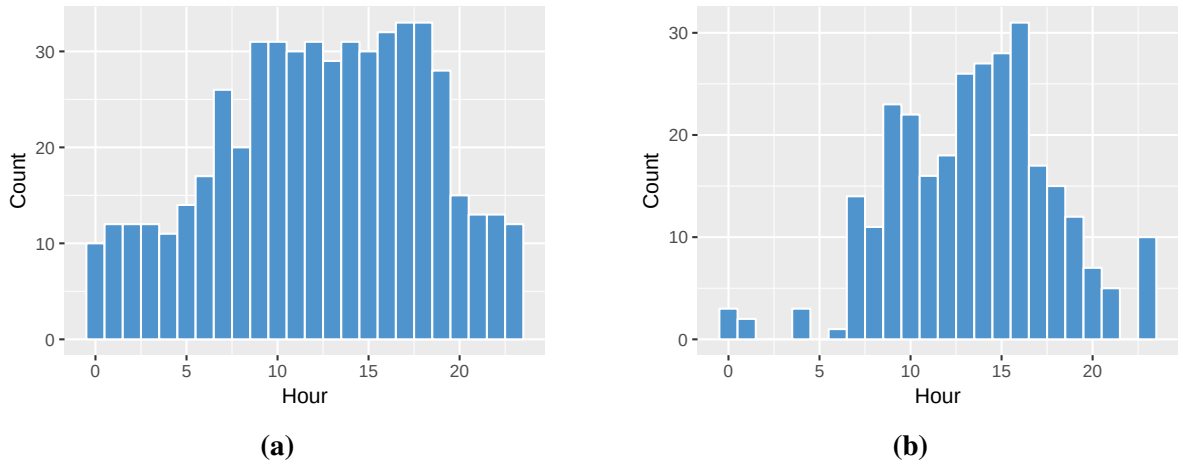


**Figure 3.1:** Number of occurrences of data points in the 10th and 20th of September, where **(a)** is from the 10th while **(b)** is the 20th.

ear interpolation. The processed temperature data after interpolation can be seen in Figure 3.2. Here both solar panels are plotted together as time interval for both observations are equal and with less data points. The behaviour of the processed data is consistent with little difference. The processed data have only been plotted until the 20th of September because of the reduced number of observations in the end of the month as seen in Figure 2.3a, 2.4a and 3.1b.

To visualise the deviation between the two solar panels, temperature observations from Figure 3.2 are subtracted and presented in Figure 3.3. Here observations from the south-facing panel are subtracted with the north-facing which have a standard deviation of $\sigma_{\text{Diff}} = 0.35$. It turns out that temperature measurements in the north-facing solar panel are higher as mean value, $\mu_{\text{Diff}} = -0.11$ is below $0$. It could be assumed that there is a calibrating difference between the two solar panels from a bias in temperature measurements during September, and a hypothesis test testing $\mu_{\text{Diff}} = 0$ would not be rejected as it is within the confidence interval.

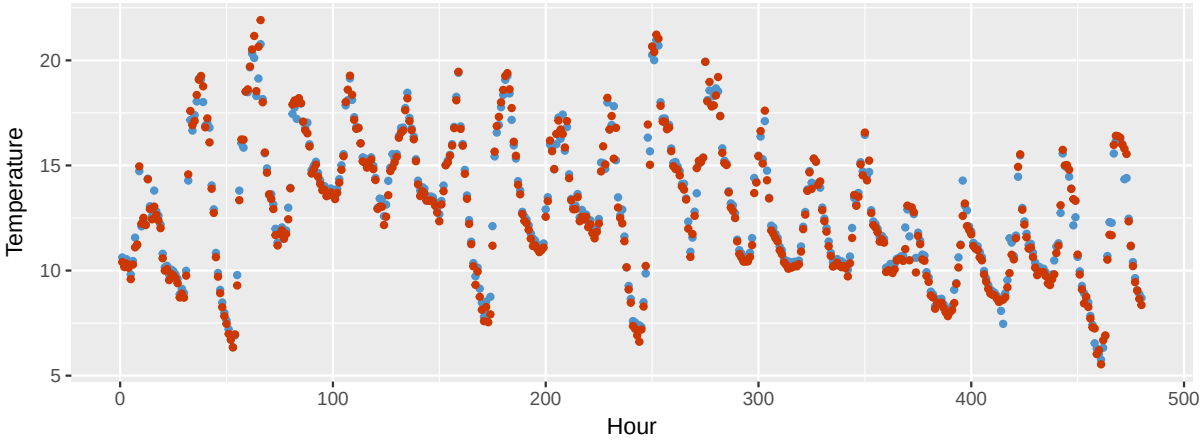


**Figure 3.2:** Temperature data constructed with respect to data collected from Waspmotes in September. The data from north-facing solar panel is plotted in blue while south-facing panel in red. Here data are plotted until the 20th of September.

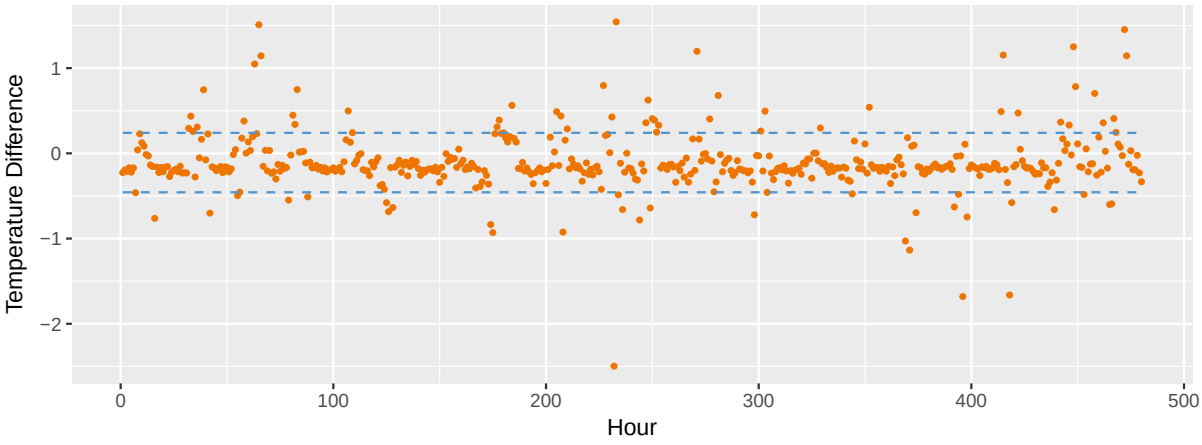


**Figure 3.3:** Observations from September from south-facing solar panels are subtracted with observations from the north-facing solar panels. Here the result is plotted in orange over a time span of 480 hours and the dotted blue lines are the standard deviation $\sigma_{\text{Diff}} = \pm 0.35$ computed from the subtracted temperatures.

It can be seen that the battery percentage in the north-facing panels in Figure 2.6a is oscillation while decreasing linearly towards zero. This is because the workload on the sensor is greater than normal operation and causes a reduction on the battery percentage. From the south-facing solar panel in Figure 2.6b it can be observed that reduction on battery percentage during night is the workload when there is no energy contribution from the environment. To obtain a sustainable battery and a consistency between the two solar panels, the workload in the north-facing solar panel should be adjusted. Figure 3.4 presents the linear decreasing battery and an adjusted battery percentage. This adjustment is updated with respect to a linear slope, $y = a + \frac{b-a}{480}x$, computed with the minimum and maximum value from the measured percentages, respectively as $a = 36.76$ and $b = 91.65$, and $x \in \{1, \ldots, 480\}$. The new adjusted battery

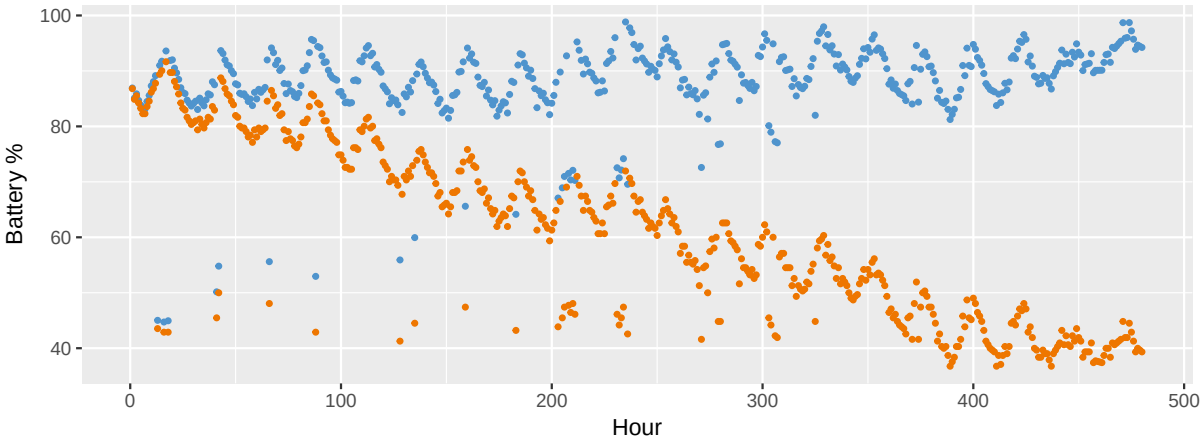


**Figure 3.4:** The adjusted battery percentage for the solar panel in direction north. The plotted points in orange are the measured percentage while blue points show the adjusted after adding the line $y = a + \frac{b-a}{480}x$, where $a$ and $b$ is respectively the minimum and maximum value from the measured percentage and $x \in \{1, \ldots, 480\}$.

performance is now similar to the workload and charging as observed in the south-facing solar panel. The relationship between the batteries is presented in Figure 3.5. The best fit would be

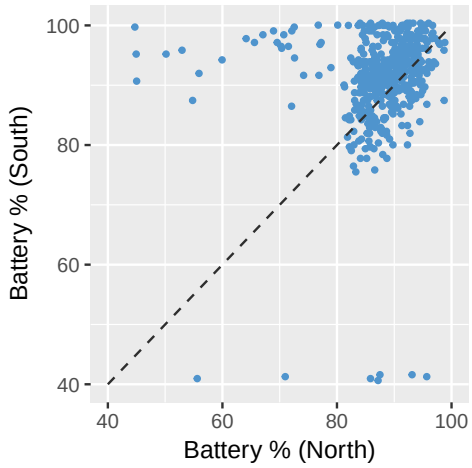


**Figure 3.5:** Battery percentage for north- and south-facing solar panels are plotted against each other with blue points. Here battery percentage for the north-facing panel is plotted on $x$-axis while south-facing is plotted on $y$-axis. The black dotted line would be the best fit on the data, implying that they are identical.

to have all observations on the straight line, meaning that observations are identical. In this case most of the observations lie between $80 - 100\%$ giving a huge accumulation to the top right corner. This is expected based on the observations from Figure 2.6 and 3.4.

To see how the variables after adaption interact with each other, the correlations are computed and presented in Figure 3.6. The correlations are still unequal, but when comparing this with the correlations obtained in Figure 2.5 these correlations are more in accordance with each other. One important modification is that humidity with the processed data is equally correlated

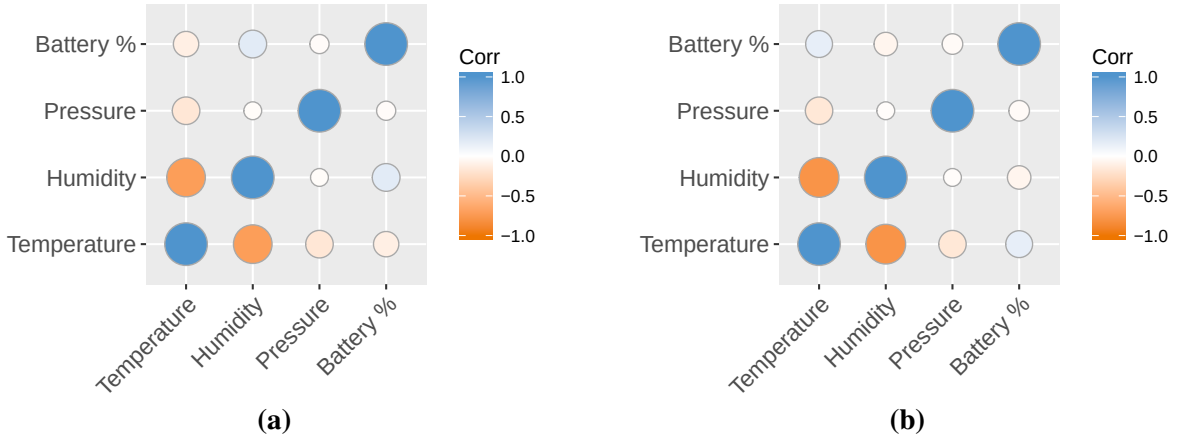


**Figure 3.6:** Correlation of temperature, humidity, pressure and battery percentage from the processed data. Figure **(a)** is from the north-facing solar panel while **(b)** is the south-facing solar panel.

with temperature for both solar panels, which was not the case with the raw data. Some of the correlations are still opposite correlated, but with little weight. The correlations between pressure and the other variables in Figure 3.6 are $0$ or insignificance. Thus, pressure will not be considered further when constructing the predictive models.

For additional verification mean and variance with the processed data are computed and presented in Table 3.1. In Figure 3.3 the mean was computed to $\mu_{\text{Diff}} = -0.11$ which is coherent with the results in this table. The problem in Table 2.1 was mostly related to the large variance and inconsistency with the two solar panels. This is not the case with these measurements as the variance is smaller and expectations are more similar.

**Table 3.1:** Presenting computed $\mu$ and $\sigma$ for the variables with the new processed data. Here index with $1$ is computed for data observed at the north-facing panel while $2$ are for the south-facing.

| Variable | Unit | $\mu_1$ | $\mu_2$ | $\sigma_1$ | $\sigma_2$ |
|---|---|---|---|---|---|
| Temperature | [°C] | 13.00 | 12.89 | 3.17 | 3.29 |
| Relative Humidity | [%] | 73.51 | 74.87 | 19.72 | 18.13 |
| Battery | [%] | 87.93 | 91.21 | 7.23 | 8.07 |

Based on these observations it appears that the processed data from the north- and south-facing solar panels are more consistent. Because battery percentage in the north-facing solar panel have a slightly higher correlation with temperature and humidity this data set will be used when adapting models and performing on-line monitoring.

It could be suggested to reduce the number of measurements at the sensors. This would help when adapting models in the future and reduce the accumulation of measurements. Furthermore, when talking about north- and south-facing solar panels it applies to the new processed data if no other is specified.

Chapter 4

# Time Series

Time series are data collected over time with each observation depending on time of measure. The data can explain growth or trends, and examples include changing stock prices or temperature observations. Previous observations can be used as guidance for decision making, by forecasting new events. Combining numerous observations into a multivariate representation might increase the insight of the development.

This chapter will start by explaining the Seasonal Autoregressive Moving Average (SARMA) model, which is a method widely used when forecasting future behaviour on time series. Where a seasonal time series is data with a repetitive pattern occurring at regular intervals. The next section will look into properties of the time series and how to select suitable weights when choosing forecasting models. The methods will first consider the univariate instance before introducing the bivariate procedure with temperature and humidity observations. After the general theory has been explained the data will be analysed and an appropriate multivariate seasonal autoregressive moving average model will be fitted.

The SARMA model is often used in order to get an understanding of the data, and to predict future behaviour. Additionally, since SARMA models can be transformed into state space representation it is suitable for the prediction model, Kalman filter (Durbin and Koopman, 2001). Before model fitting it is important to understand the behaviour and dependencies of the variables. Following this, a suitable bivariate model with preferred weights can be used when implementing a model for the on-line monitoring.

## 4.1 Seasonal Autoregressive Moving Average Model (SARMA)

There are various methods to use when predicting in time series. Two attractive methods are *autoregressive* (AR) and *moving average* (MA) models, where both depend linearly on the past data points. Adding a new data point into the model will cause a removal of the last, such that only the specified amount of data points will be considered in the model. To distinguish between them, AR looks at the previous values in the data while MA uses a linear combination

of independent variables of previous time steps. Combining these methods gives the *autoregressive moving average* (ARMA) model. Considering an ARMA model, then a data point $X_t$ at time $t$ can be formulated as,

$$X_t = \phi_1 X_{t-1} + \phi_2 X_{t-2} + \ldots + \phi_p X_{t-p} + Z_t - \theta_1 Z_{t-1} - \theta_2 Z_{t-2} \ldots - \theta_q Z_{t-q}, \tag{4.1}$$

where $X_{t-i}$ is the $i$'th previous data point, $\phi_i$ for $i = 1, 2, ..., p$ and $\theta_j$ for $j = 1, 2, ..., q$ are parameters respectively of the AR and MA model, where $p$ corresponds to the lagged factor for AR and $q$ is the order of the MA model. The ARMA model can then be written as ARMA$(p, q)$. We assume in this project that $X_t$ is a mean zero and variance as $\sigma^2_{X_{t-i}}$, and $Z_{t-j}$ is Gaussian independent and identically distributed with zero mean and variance $\sigma^2_Z$ (Everitt, 2014). One can shift the process to another mean level, or include a non-stationary mean, for instance by using covariates. For the model to be stationary and invertible there are certain requirements on $\phi_i$ and $\theta_j$ which in return increases the certainty and possibilities when forecasting future values (Brockwell and Davis, 2002). Some special cases with these requirements will be discussed further below.

The simplest models would be the AR$(0)$ and MA$(0)$. However, this would imply that there are no dependencies in the process. Increasing the models to AR$(1)$ and MA$(1)$ would give a dependence with the previous data point and the equations can be written as,

$$\text{AR}(1): \quad X_t = \phi_1 X_{t-1} + Z_t \tag{4.2}$$

$$\text{MA}(1): \quad X_t = \theta_1 Z_{t-1} + Z_t. \tag{4.3}$$

Here, $\phi_1 \neq 0$ and $\theta_1 \neq 0$ correspond to how dependent $X_t$ is to the variables at the previous time values. The two models have been simulated in R and are presented in Figure 4.1 and 4.2 for parameters either as **a)** $\phi_1 = \theta_1 = 0.5$ or **b)** $\phi_1 = \theta_1 = 0.98$.

Let us first consider the first case with AR$(1)$ presented in Figure 4.1. A model is stationary if the mean and variance is independent of time. Assuming a stationary model, then $\text{Var}[X_t] = \text{Var}[X_{t-1}]$. The expected value and variance for the AR(1) model from Equation (4.2) are formulated as,

$$\begin{aligned}
\text{E}[X_t] &= \phi_1 \text{E}[X_{t-1}] + \text{E}[Z_t] \\
&= 0 \\
\text{Var}[X_t] &= \phi_1^2 \text{Var}[X_{t-1}] + \text{Var}[Z_t] \\
&= \phi_1^2 \text{Var}[X_{t-1}] + \sigma_Z^2 \\
\Rightarrow \sigma_Z^2 &= (1 - \phi_1^2)\sigma_X^2.
\end{aligned} \tag{4.4}$$

Here the mean is zero and the variance is independent of time. Because $\sigma_Z^2 > 0$ it follows that $1 - \phi_1^2 > 0$, and thus we have the requirement, $|\phi_1| < 1$ to make the model stationary. In

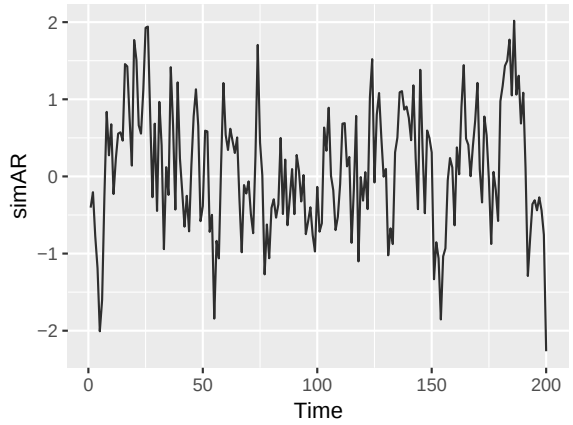


**(a)** AR$(1)$ model with $\phi_1 = 0.5$, with simulated values in the interval [-2,2].

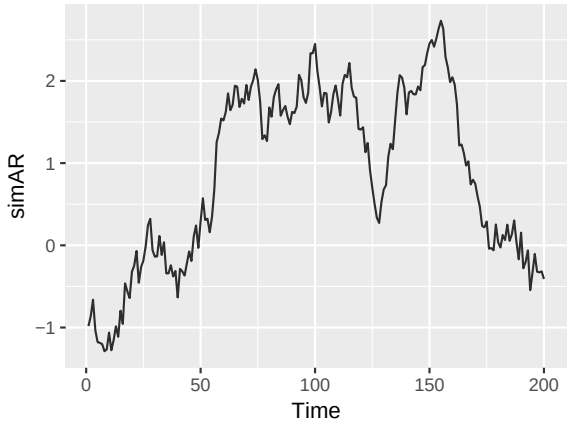


**(b)** AR$(1)$ model with $\phi_1 = 0.98$, with simulated values in the interval [-1,3].

**Figure 4.1:** Simulated data over 200 time units for AR$(1)$ models, with respect to Equation (4.2).

addition to being stationary, an AR model is always invertible because it can be expressed on finite form, meaning that $p < \infty$ (Brockwell and Davis, 2002).

Considering the two models with different values of $\phi_1$. In Figure 4.1a the simulated values are quite jagged with little dependency. Moving to Figure 4.1b, the dependency with the previous data is higher and have little variation between the simulated variables. The variance in Equation (4.4) with the values of $\phi_1$ gives,

$$\begin{aligned} \phi_1 = 0.5, \quad \sigma_Z^2 = 0.56\sigma_X^2 \\ \phi_1 = 0.98, \quad \sigma_Z^2 = 0.04\sigma_X^2. \end{aligned}$$

This is also representative for what can be seen in Figure 4.1, the simulations are stable within the interval of $[-2, 2]$ and $[-1, 3]$. However, the variability between each time step in Figure 4.1a is high because the variance for the white noise is multiplied with a large factor. In Figure 4.1b the variability between each time step is smaller as the factor is only $0.04$. Of course, on could enforce $\sigma_Z^2$ to be the same in both cases. Then $\sigma_X^2$ would be much smaller for the case with small $\phi_1$.

Further, addressing the other model in Equation (4.3), simulations with two values for $\theta$ are presented in Figure 4.2. A MA model, when $\sum_{j=-\infty}^{\infty} |\theta_j| < \infty$, is always stationary, hence MA$(1)$ is stationary (Brockwell and Davis, 2002). When $|\theta_1| < 1$ the model is said to be invertible. It can be difficult to see if a model is invertible or not, but when a MA model is invertible it means that this model can be converted and expressed as an AR model. In this case, from Equation (4.2) and (4.3), the inverted equation then becomes,

$$X_t = Z_t + \theta_1 X_{t-1} - \theta_1^2 X_{t-2} + \theta_1^3 X_{t-3} - \dots.$$

In order to keep the dependency within close the closest point should have more significance

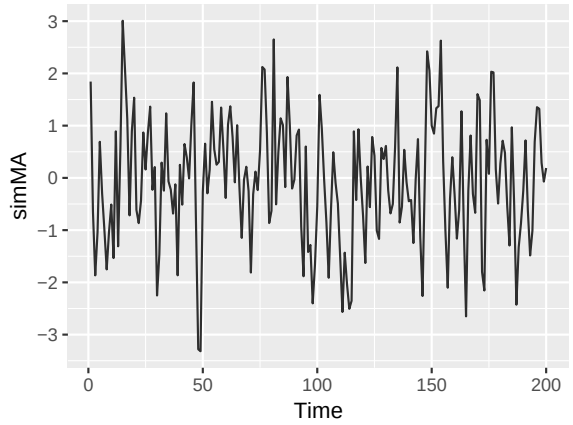


**(a)** MA$(1)$ model with $\theta_1 = 0.5$, with simulated values on the interval [-3,3].

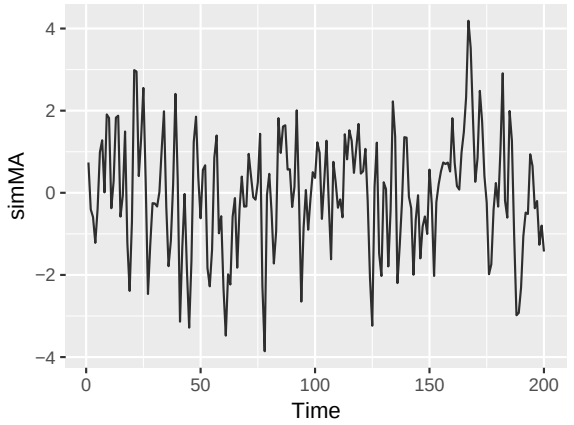


**(b)** MA$(1)$ model with $\theta_1 = 0.98$, with simulated values on the interval [-4,4].

**Figure 4.2:** Simulated data over 200 time units for MA$(1)$ models, with respect to Equation (4.3).

$|\theta_1| < 1$, if not the weight will increase when moving infinitely (Wei, 2006). Thus we have the requirements on $\theta_1$, and also an invertible model. In conclusion, the AR and MA models will be stationary and invertible if fulfilling the requirements $|\phi_1| < 1$ and $|\theta_1| < 1$.

The data might have observations with repetitive and periodic intervals, explained as a seasonal behaviour. Figure 3.2 gives an example of data containing a seasonal trend. If the data include seasonality it can be modelled as a seasonal ARMA process. This SARMA model is written as ARMA$(p, q) \times (P, Q)_s$, where $p$ and $q$ are the same as previously explained, and capital letter corresponds to the same effect in the seasonality with $s$ as the periodic order. Figure 4.3 shows two simulated SAR$(1) \times (1)$ models with a $24$ hour seasonality term added to the model. The equation for the SAR$(1) \times (1)$ model can be expressed as,

$$\text{SAR}(1) \times (1): \quad X_t = \phi_1 X_{t-1} + \phi_{24} X_{t-24} - \phi_1 \phi_{24} X_{t-25} + Z_t, \tag{4.5}$$

where $\phi_1$ and $\phi_{24}$ are respectively the previous and $24$ hour seasonal dependency for the current point $X_t$. The model will also be slightly dependent on the data that are $25$ hours behind, as the two dependencies are multiplied together to give an additional lagged value. However, as $\phi_1$ and $\phi_{24}$ are both smaller than $1$, the $25$ hour dependence will be of a smaller size and not that significant. In Figure 4.3 the values for $\phi_1$ and $\phi_{24}$ are the same as previously given in Figure 4.1, **a)** $\phi_1 = \phi_{24} = 0.5$ and **b)** $\phi_1 = \phi_{24} = 0.98$. The simulated models are stationary and invertible, as the constraints on $\phi_1$ and $\phi_{24}$ still holds. Solving Equation (4.5) with respect to the white noise variance this becomes,

$$\sigma_Z^2 = \left(1 - \phi_1^2 - \phi_{24}^2 + \phi_1^2 \phi_{24}^2\right) \sigma_X^2.$$

The simulations in Figure 4.3 are stationary with a higher variability between time steps in Figure 4.3a. Because Figure 4.3b have a smaller variability the seasonality is better presented

in this model. There are visible peaks for every $24$hour, while in Figure 4.3a it seems to be more random and with almost the same behaviour as in Figure 4.1a. However, the SAR$(1)\times(1)$ model in **a)** is not as jagged as in the AR$(1)$ model.

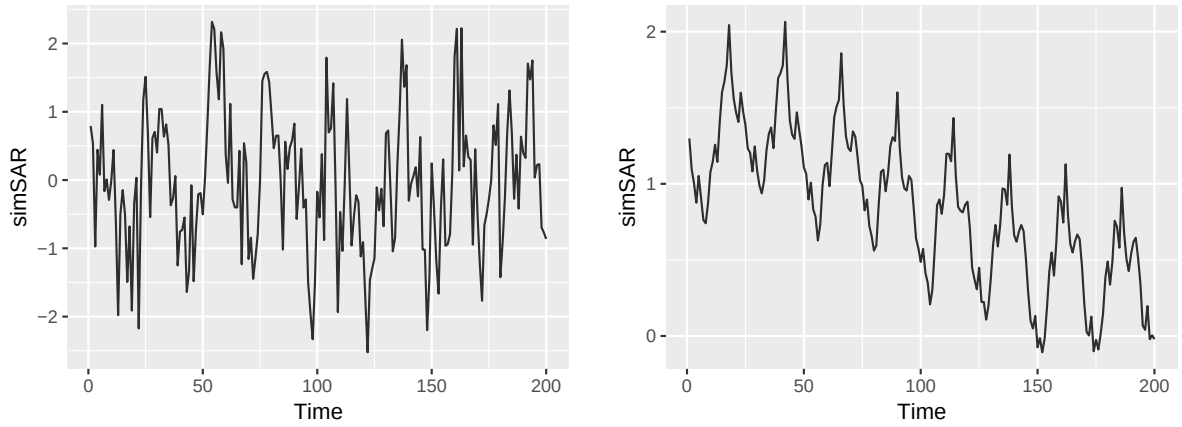


**(a)** SAR$(1) \times (1)$ model with $\phi_1 = \phi_{24} = 0.5$. **(b)** SAR$(1) \times (1)$ model with $\phi_1 = \phi_{24} = 0.98$.

**Figure 4.3:** Simulated data over 200 time units for SAR$(1) \times (1)$ with respect to Equation (4.5).

Considering a seasonal process $X_t$, writing this on a general form with respect to an AR and MA term, the equation becomes,

$$\Phi(B^s)\phi(B)X_t = \Theta(B^s)\theta(B)Z_t, \tag{4.6}$$

$\phi(B)$, $\theta(B)$, $\Phi(B)$ and $\Theta(B)$ can all be expressed as,

$$\begin{aligned}
\Phi_P(B^s) =& 1 - \Phi_1 B^s - \Phi_2 B^{2s} - \ldots - \Phi_P B^{Ps} \\
\phi_p(B) =& 1 - \phi_1 B^1 - \phi_2 B^2 - \ldots - \phi_p B^p \\
\Theta_Q(B^s) =& 1 - \Theta_1 B^s - \Theta_2 B^{2s} - \ldots \Theta_Q B^{Qs} \\
\theta_q(B) =& 1 - \theta_1 B - \theta_2 B^2 - \ldots - \theta_q B^q,
\end{aligned}$$

where $\phi(B)$, $\theta(B)$, $X_t$ and $Z_t$ are the same as in Equation (4.1) with $p = q = 1$, $\Phi(B)$ and $\Theta(B)$ are the dependency with respect to the seasonality. $B$ are the so called back shift operator which indicate if $X_t$ is dependent on the $i$'th previous point, i.e. $BX_t = X_{t-1}$, $B^2X_t = X_{t-2}$, etc.. $\Phi(B)$ and $\Theta(B)$ have the same constraints as were presented for $\phi(B)$ and $\theta(B)$, as they also need stationary and invertible requirements on the model (Wei, 2006). In addition, $\phi(B)$, $\theta(B)$, $\Phi(B)$ and $\Theta(B)$ can be expressed on respectively $p$'th, $q$'th, $P$'th and $Q$'th degree polynomials. Now $B$ is changed with $z$, and establish the polynomials for $\phi(z)$, $\theta(z)$, $\Phi(z)$ and $\Theta(z)$. This can be used when computing for the causality and invertibility requirements, $|\phi(z)| \neq 0$ and $|\Phi(z)| \neq 0$ with $|z| \leq 1$ (Brockwell and Davis, 1991).

From Equation (4.5) we had $\phi_1$ and $\phi_{24}$, with the latter value weighting on the seasonality

$s = 24$. With Equation (4.5) and (4.6), SAR$(1) \times (1)$ becomes,

$$\begin{aligned}(1 - \Phi_1 B^{24})(1 - \phi_1 B)X_t &= Z_t \\ (1 - \phi_1 B - \Phi_1 B^{24} + \Phi_1 \phi_1 B^{25})X_t &= Z_t.\end{aligned}$$

The simulated AR(1) and MA(1) models defined in Equation (4.2) and (4.3) have known dependencies, $p = q = 1$. However, when data, such as the data from the solar panels in this project, are given, the values of $q$ and $p$ will have to be determined based on information stored in the data. The following methods are used when analysing the behaviour, and selecting preferred values.

## 4.2 Data Analysis of Time Series, and Relation to ARMA

### 4.2.1 Autocovariance and Autocorrelation Function (ACF)

The models presented, AR$(1)$, MA$(1)$ and SAR$(1) \times (1)$, have all been assigned a weight and dependency with the simulated data. This is normally not the situation and we will have to find the dependencies within the temperature and humidity data. Hence, the idea of finding a useful ARMA$(p, q) \times (P, Q)$ model is to identify suitable values for $p$, $q$, $P$ and $Q$, and associated parameter weights on $\phi_1, ...$, $\theta_1, ..$, $\Phi_1, ...$ and $\Theta_1, ....$ The identification is based on information possessed in the data, and autocorrelation function (ACF) is one method that can estimate some of the underlying dependency within the data. The autocorrelation is a scaled version of the autocovariance function. Considering two different times, $t$ and $t + k$ for observation $X_{t+i}$, $i = 0, k$, then the covariance and correlation are given as,

$$\begin{aligned}\gamma_k &= \text{Cov}[X_t, X_{t+k}] = \text{E}[(X_t - \mu)(X_{t+k} - \mu)] \\ \rho_k &= \frac{\text{Cov}(X_t, X_{t+k})}{\sqrt{\text{Var}[X_t]}\sqrt{\text{Var}[X_{t+k}]}} = \frac{\gamma_k}{\gamma_0}.\end{aligned} \tag{4.7}$$

Here, $\gamma_k$ and $\rho_k$ represents the covariance and correlation between $X_t$ and $X_{t+k}$ from the same process and are called the autocovariance function and autocorrelation function (Madsen, 2008). The higher value the autocorrelation becomes the more dependent are the different times.

In Section 4.1 it was pointed out that an AR$(1)$ model with $\phi$ closer to $1$ means the current observation is highly dependent on the previous time, and this can be observed in Figure 4.4a and 4.4b. The dotted blue lines are computed as bounds of $\pm 1.96 n^{-1/2}$ with $n = 200$ (Brockwell and Davis, 1991). The latter figure have a slowly decaying curve and reaches the horizontal line after $25$ lags, while in the first figure the line is reached after $6$ lags. From Wei (2006) a model can be assumed to have weights in an AR model if it is either tailing off exponentially or decaying as a damped sine wave pattern. In this case, the two AR$(1)$ models are tailing of exponentially. The performance of the two MA$(1)$ models are presented in Figure 4.4c and 4.4d.

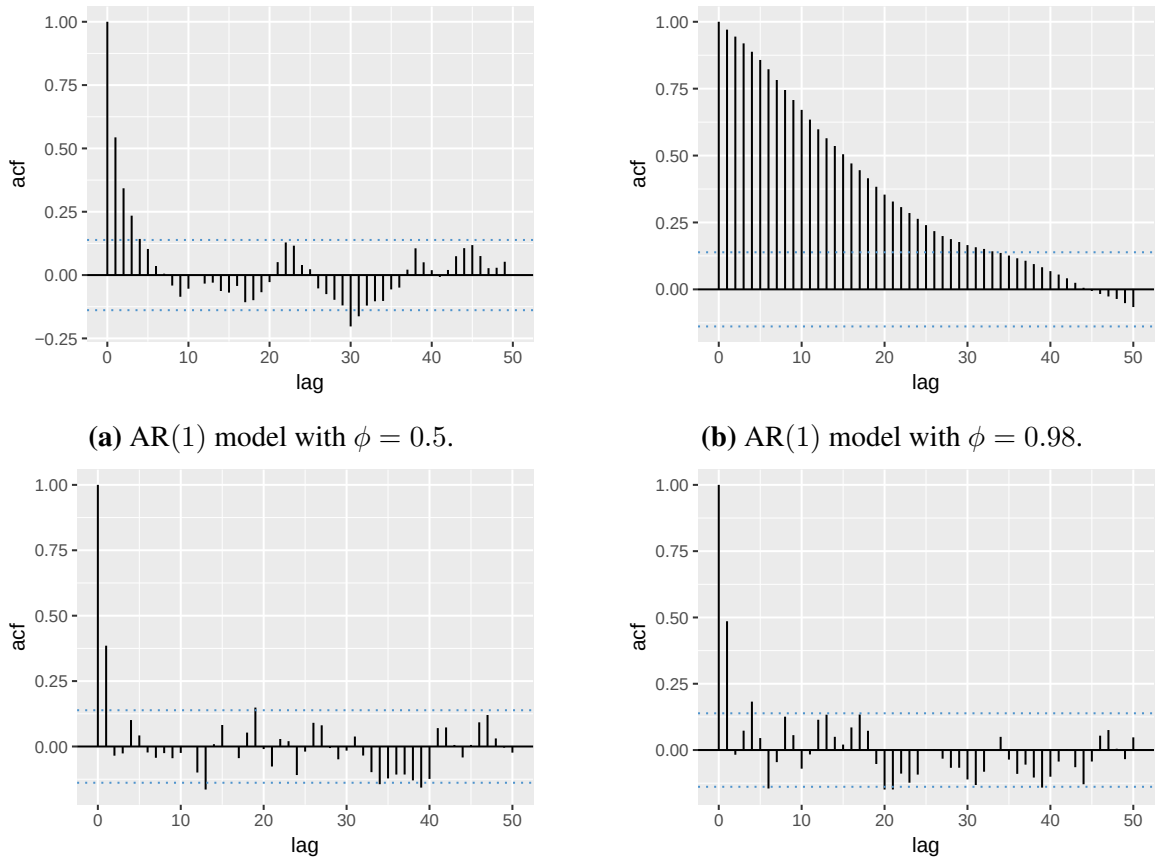


**(a)** AR$(1)$ model with $\phi = 0.5$.

**(b)** AR$(1)$ model with $\phi = 0.98$.

**(c)** MA$(1)$ model with $\theta = 0.5$.

**(d)** MA$(1)$ model with $\theta = 0.98$.

**Figure 4.4:** Autocorrelation functions plotted with the simulated data for AR$(1)$ and MA$(1)$ models, with different weights of dependency. The horizontal dotted blue lines are the coverage probability of 95% confidence interval computed as $\pm 1.96n^{-1/2}$ with $n = 200$.

In these figures it can be seen that the first two lags have high values while in the following lags almost all of them are within the interval, meaning the correlation is insignificant for $q + 1$. In this case $q + 1$ would be 2, as the two preceding lags are placed at 0 and 1. This was expected because of the initialised simulated MA(1) model.

### 4.2.2 Partial Autocorrelation Function (PACF)

It can also be useful to look at the Partial Autocorrelation Function (PACF) when looking at the dependency between two observations, $X_t$ and $X_{t+k}$. The PACF at lag $k$, $\alpha(k)$, can be considered as the conditional correlation between the two observations and are defined as,

$$\begin{aligned}\alpha(1) =& \text{Corr}(X_{t+1}, X_t) = \rho(1) \\ \alpha(k) =& \text{Corr}(X_{t+k+1} - P_{\bar{sp}\{1,X_2,\ldots,X_{t+k}\}}X_{t+k+1}, X_{t+k} - P_{\bar{sp}\{1,X_2,\ldots,X_{t+k}\}}X_{t+k}) \qquad k \geq 2,\end{aligned} \tag{4.8}$$

where $P_{\bar{sp}\{1,X_2,\ldots,X_{t+k}\}}$ are the projection of $X_{t+i+1}$, for $i = 0, k$, spanned in $\{1, X_2, \ldots, X_{t+k}\}$.

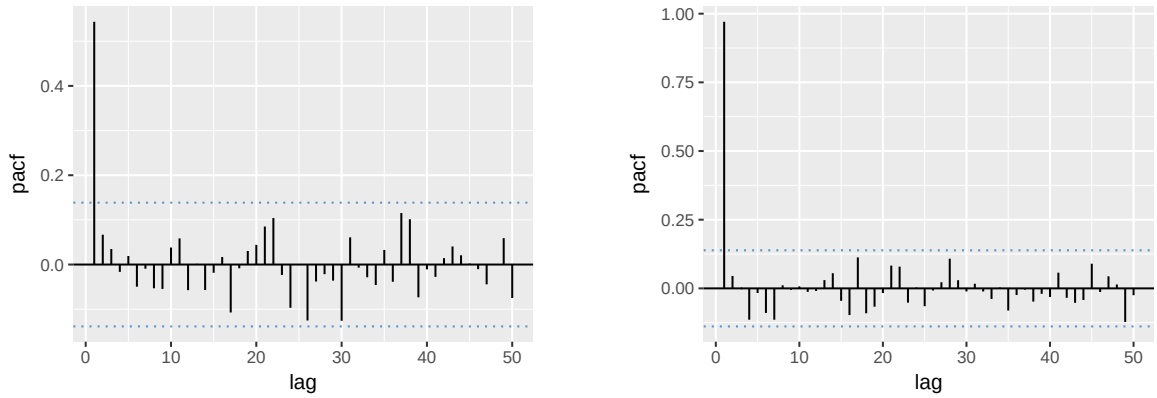


**(a)** AR$(1)$ model with $\phi = 0.5$.




**(b)** AR$(1)$ model with $\phi = 0.98$.

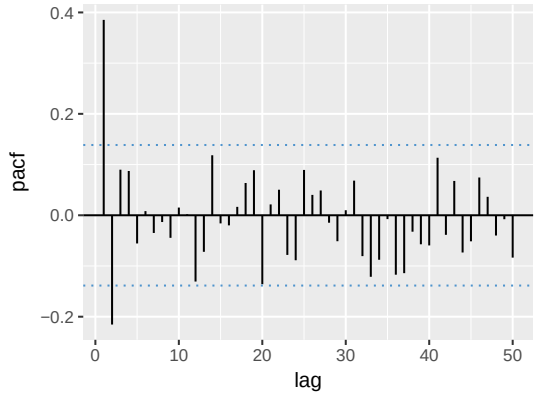


**(c)** MA$(1)$ model with $\theta = 0.5$.

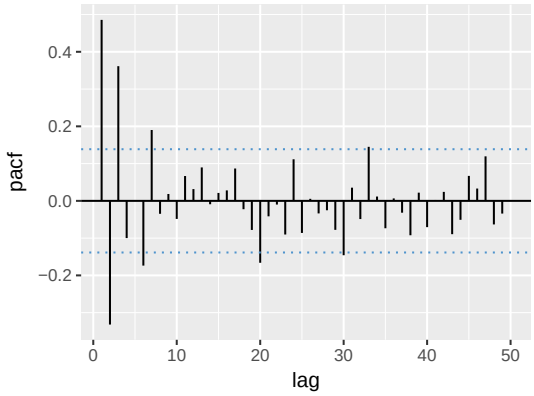


**(d)** MA$(1)$ model with $\theta = 0.98$.

**Figure 4.5:** Partial autocorrelation functions plotted with the simulated data for AR$(1)$ and MA$(1)$ models, with different weights of dependency. The horizontal dotted blue lines are the coverage probability of 95% confidence interval computed as $\pm 1.96 n^{-1/2}$ with $n = 200$.

The PACF is the correlation of two residuals obtained after regressing $X_{t+k}$ and $X_t$ on the intermediate observations $X_{t+1}, \ldots, X_{t+k-1}$, when $k \geq 2$ (Brockwell and Davis, 1991). The same observations explained in the previous section with MA and ACF can be used when looking at lags and values for $p$ in AR-models. In Figure 4.5a and 4.5b the lags after 1 are below the confidence interval and can be considered as insignificant. For an AR$(1)$ model the theoretical PACF is 0 for lags $k \geq 2$. Thus, we have an AR$(1)$ model for both simulations with different $\phi_1$. When it comes to Figure 4.5c and 4.5d the lags decline exponentially towards the boundary, and are behaving as MA-models (Wei, 2006).

### 4.2.3 ACF and PACF with SARMA model

In the two previous sections, Section 4.2.1 and 4.2.2, ACF and PACF have been considered for AR$(1)$ and MA$(1)$ models. The remaining model that were presented in Section 4.1 is the SAR$(1) \times (1)$ model which have a seasonality term that will give an impact to the behaviour of ACF and PACF. The same principles presented in Equation (4.7) and (4.8) are used and the

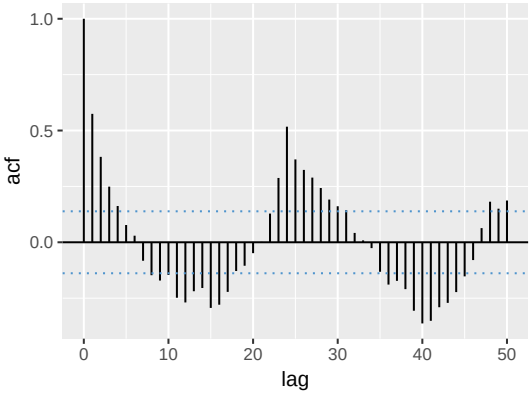


**(a)** ACF of SAR$(1) \times (1)$ model with $\phi = 0.5$.

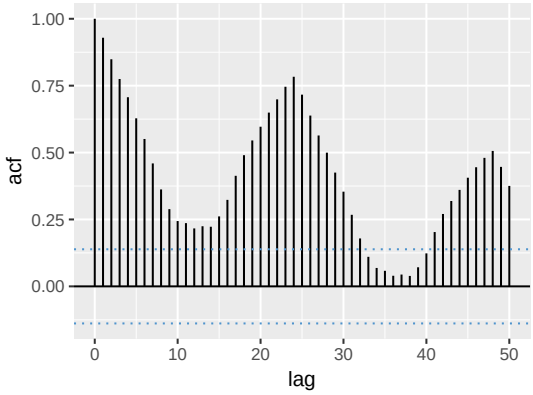


**(b)** ACF for SAR$(1) \times (1)$ model with $\phi = 0.98$.

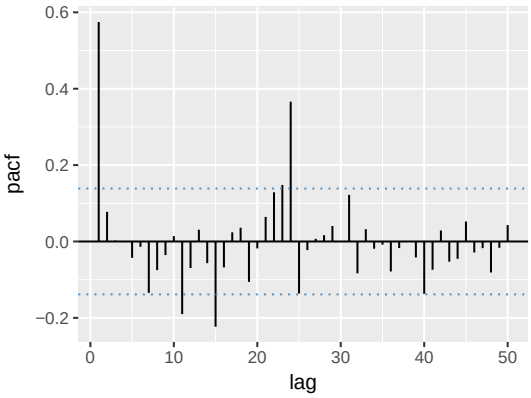


**(c)** PACF for SAR$(1) \times (1)$ model with $\phi = 0.5$.

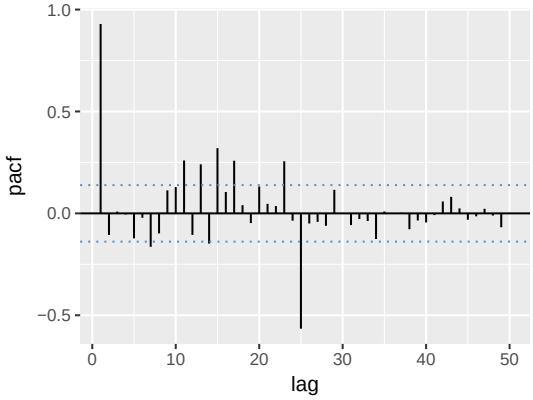


**(d)** PACF for SAR$(1) \times (1)$ model with $\phi = 0.98$.

**Figure 4.6:** Autocorrelation and partial autocorrelation functions are plotted with the simulated data for SAR$(1) \times (1)$ models, with different weights of dependency. The horizontal dotted blue lines are the coverage probability of 95% confidence interval computed as $\pm 1.96 n^{-1/2}$ with $n = 200$.

computed ACF and PACF for a SAR$(1) \times (1)$ can be seen in Figure 4.6.

It can be seen that there is a seasonality term that should be kept in consideration because all four figures have an increased value after 24 lags. The size and number of lags that are increased depends on how correlated the different times are with each other. Take for example, SAR$(1) \times (1)$ in Figure 4.6b. This model have lags with higher dependency with lags tailing off slower compared to the lags in Figure 4.6a. Looking at Figure 4.6c and 4.6d both give an indication that $p = 1$ as the lags at $p \geq 2$ are insignificant compared to the size in the first lag.

The observations presented in Section 4.1 and 4.2 demonstrate convenient methods to understand the data and processes to formulate models. At first it is important to look at the data to get a picture of the behaviour and if there is any seasonal behaviour that should be considered. After this the ACF and PACF can be plotted and studied to find suitable values for $p$ and $q$. These observations will give guidance and limit the model fitting. The appropriate model will further on be used for predicting future behaviours of the data in the monitoring.

## 4.3 Multivariate SARMA model and Cross-Correlation

The theory presented in the previous sections is presented with respect to univariate observations. When considering the outcome of several variables in a univariate model for each of them could be presented independently. However, if these variables are correlated and seasonal, considering two separate univariate models would most likely ignore important dependencies (Härdle and Simar, 2015). One could therefore select appropriate weights and use a seasonal multivariate ARMA model to deal with the dependency within the outcome. Figure 4.7 demonstrates two highly correlated simulated times series. The performance of the simulations are following each other closely which is expected as $\rho = 0.9$.

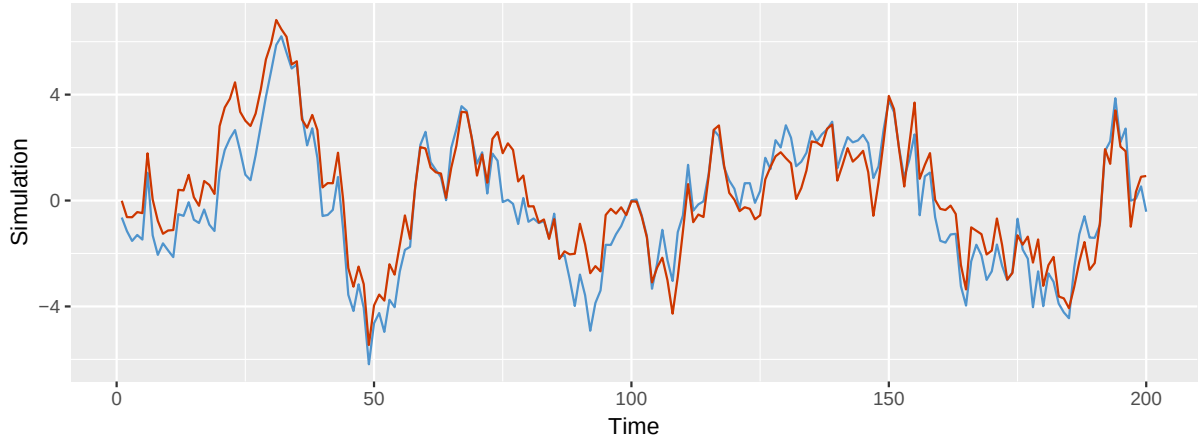


**Figure 4.7:** Simulated multivariate time series that are correlated with factor $\rho = 0.9$. Both simulations have $\phi = 0.9$.

The theory presented in Section 4.1 and 4.2 is still relevant, and will be extended for multivariate instances. Simulations are presented as a bivariate instance because model fitting will eventually be applied on temperature and humidity data from Chapter 3. Nevertheless, the theory can be increased to $m$-variate instances.

### 4.3.1 Multivariate SARMA

From Section 4.1, instead of considering $X_t$ as one data point, it should be defined as a vector representation of several variables. Let $\mathbf{X}_t$ be a $m$-variate vector at time $t$. Then, a multivariate ARMA$(p, q) \times (P, Q)$ model can be formulated as,

$$\mathbf{\Phi}(B^s)\boldsymbol{\phi}(B)\mathbf{X}_t = \mathbf{\Theta}(B^s)\boldsymbol{\theta}(B)\mathbf{Z}_t, \tag{4.9}$$

which is almost the same as Equation (4.6). However, $\mathbf{\Phi}(B^s)$, $\boldsymbol{\phi}(B)$, $\mathbf{\Theta}(B^s)$ and $\boldsymbol{\theta}(B)$ could previously be reformulated and defined as linear polynomials. In the multivariate process these equations are matrix-valued polynomials with $m \times m$ matrices, where $m$ is the number of

variables. In addition, $\mathbf{Z}_t$ is the multivariate white noise, $\mathbf{Z}_t \sim \text{WN}(0, \Sigma_{\text{White}})$ (Brockwell and Davis, 1991).

For simplicity, disregard the seasonality term in Equation (4.9) and define separate $m$-AR$(1)$ and $m$-MA$(1)$ models. With $m = 2$, $\mathbf{X}_t = [x_1, x_2]_t^T$ and $\mathbf{Z}_t = [z_1, z_2]_t^T$ the bivariate models become,

$$
\begin{aligned}
2-\text{AR}(1): \quad & \begin{bmatrix} x_1 \\ x_2 \end{bmatrix}_t = \begin{bmatrix} \phi_{11}^{(1)} & \phi_{12}^{(1)} \\ \phi_{21}^{(1)} & \phi_{22}^{(1)} \end{bmatrix} \begin{bmatrix} x_1 \\ x_2 \end{bmatrix}_{t-1} + \begin{bmatrix} z_1 \\ z_2 \end{bmatrix}_t \\
2-\text{MA}(1): \quad & \begin{bmatrix} x_1 \\ x_2 \end{bmatrix}_t = \begin{bmatrix} \theta_{11}^{(1)} & \theta_{12}^{(1)} \\ \theta_{21}^{(1)} & \theta_{22}^{(1)} \end{bmatrix} \begin{bmatrix} z_1 \\ z_2 \end{bmatrix}_{t-1} + \begin{bmatrix} z_1 \\ z_2 \end{bmatrix}_t .
\end{aligned}
$$

On a compressed form the equations can be written as,

$$2-\text{AR}(1): \quad \mathbf{X}_t = \boldsymbol{\phi}_1 \mathbf{X}_{t-1} + \mathbf{Z}_t \tag{4.10}$$

$$2-\text{MA}(1): \quad \mathbf{X}_t = \boldsymbol{\theta}_1 \mathbf{Z}_{t-1} + \mathbf{Z}_t. \tag{4.11}$$

The off diagonal elements in both models represents how much one variable can be explained by the other variables at different times. The diagonal elements explain the dependency with their respective variables. Equation (4.10) and (4.11) can be merged together and extended to a seasonal multivariate model as in Equation (4.9).

The requirements to keep a multivariate SARMA model stationary and invertible are based on the previous requirements for an AR- and MA-model. Nevertheless, as we are extending to matrix-polynomials the definitions should be presented on this form. Chapter 3 and 11 in Brockwell and Davis (1991) provide with necessary criteria and proof for a multivariate ARMA model to have *causal* and *invertible* representation. The requirements are defined as,

$$\text{Causality Criterion:} \quad \det \boldsymbol{\phi}(z) \neq 0 \quad \forall z \in \mathbb{C} \text{ s.t. } |z| \leq 1 \tag{4.12}$$

$$\text{Invertibility Criterion:} \quad \det \boldsymbol{\theta}(z) \neq 0 \quad \forall z \in \mathbb{C} \text{ s.t. } |z| \leq 1. \tag{4.13}$$

Changing $\boldsymbol{\phi}(z)$ and $\boldsymbol{\theta}(z)$ with respectively $\boldsymbol{\Phi}(z)$ and $\boldsymbol{\Theta}(z)$ contribute with necessary requirements for the seasonal polynomial. Thus, Equation (4.12) and (4.13) present the requirements on causality and invertibility for a multivariate SARMA model.

### 4.3.2 Auto- and Cross-Correlation

As presented in Section 4.2.1, autocorrelation measure how a series is correlated with itself at distinctive lags, and would visualise which lags are more dependent on each other. This would suggest which lags should be included in the SARMA model to predict future values. It is still relevant to apply this on a multivariate model, to see how each feature is dependent with itself. Furthermore, as the observations are correlated with each other, an auto and cross-correlation

should be studied to see the degree of correlation, and at which lags the series are most correlated. From Section 4.2.1 the autocorrelation $\rho_k$ at lag $k$ is defined as in Equation (4.7). Extending and defining $\Gamma(k)$ and $\mathrm{P}(k)$ as respectively the autocovariance and autocorrelation matrices. Then Harvey (1990) presents $\Gamma(k)$ and $\mathrm{P}(k)$ at lag $k \geq 0$ as,

$$\begin{aligned} \Gamma(k) =& \boldsymbol{\phi}^k \Gamma(0) \\ \mathrm{P}(k) =& D_0^{-1} \Gamma(k) D_0^{-1}, \end{aligned} \tag{4.14}$$

where $\boldsymbol{\phi}$ is the same as presented earlier and $D_0^2 = \mathrm{diag}[\gamma_{11}(0), \ldots, \gamma_{mm}(0)]$ with $m$ corresponding to the $m$-variate model. The cross-correlation between the $ij$'th element in $\mathrm{P}(k)$ at lag $k$ becomes,

$$\rho_{ij}(k) = \frac{\gamma_{ij}(k)}{\sqrt{\gamma_{ii}(0)\gamma_{jj}(0)}}. \tag{4.15}$$

The same application and determination considering model selection of an AR($p$) and MA($q$) model is used for a multivariate model. In addition, cross-correlation will help in determining which and how much features are correlated with each other. Figure 4.8 presents the auto- and cross-correlated function for the simulated bivariate ARMA$(1, 0)$ model from Equation (4.9) and Figure 4.7. The simulated data is exponentially decreasing towards the dotted blue lines. Because of the heavy weight on $\phi$ the closer to lag $1$ the more correlated are time lags with each other. As $\rho = 0.9$ it can be seen that the first lags in the off diagonal plots are high as the two features are correlated. Additionally, there are no contribution from a MA-model which make sense as $\theta$ in the simulated data is $0$.

### 4.3.3 Partial Auto Cross-Correlation

Partial autocorrelation in a univariate setting looks at how the time series at one lag is correlated with itself at other previous lags, i.e. how $X_t$ alone is correlated with $X_{t-1}$ and not looking at how $X_{t-1}$ is explained by other previous correlations as well. Thus, extending this to a multivariate model would compute the partial autocorrelation with a matrix with $m$ number of features. The partial autocorrelation on matrix form are similar to Equation (4.14), except linear dependence at intervening lags are removed. Wei (1985) define it as,

$$\mathrm{P}(k) = D_v(k)^{-1} V_{v,u}(k) D_u(k)^{-1}, \tag{4.16}$$

where $D_v(k)^{-1}$ and $D_u(k)^{-1}$ are the diagonal matrices presented in Section 4.3.2 with the $i$'th diagonal element as the square root of respectively the $i$'th element in $\mathrm{var}(v_{k-1,t})$ and $\mathrm{var}(u_{k-1,t+k})$. $V_{v,u}$ is the covariance between $v_{k-1,t}$ and $u_{k-1,t+k}$, which are residuals from a regression of $X_t$ and $X_{t+k}$ after removing the linear dependence on the vectors at the intervening

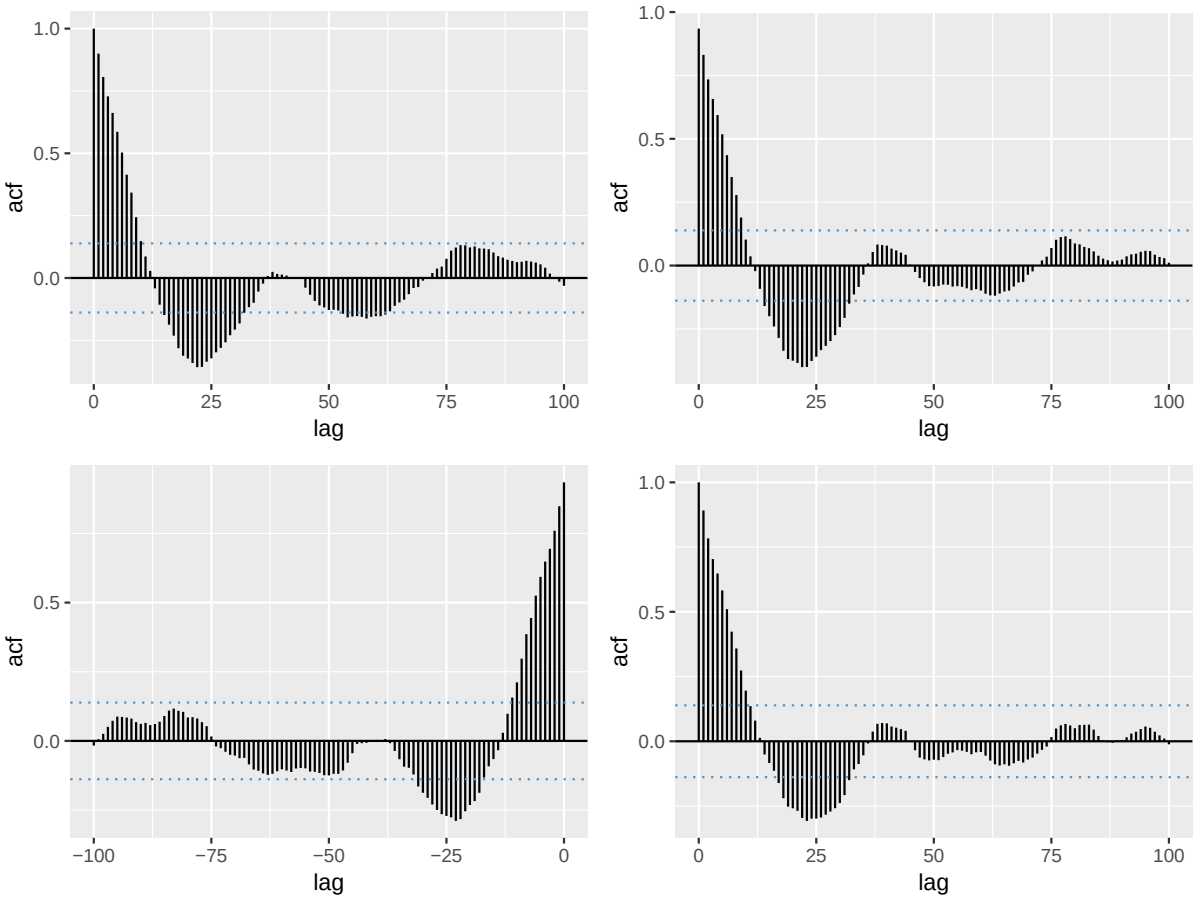


**Figure 4.8:** Auto- and cross-correlation functions are plotted with simulated bivariate data that are correlated with $\rho = 0.9$. The data are simulated with $\phi = 0.9$ and $\theta = 0.1$. Plotted figures placed diagonal from top left are ACF with itself while figures placed diagonal left bottom are the cross-correlation. The horizontal dotted blue lines are the coverage probability of 95% confidence interval computed as $\pm 1.96 n^{-1/2}$ with $n = 200$.

lags, $X_{t+1}, \ldots, X_{t+1-k}$ (Wei, 1985, 2006).

Figure 4.9 presents the partial auto- and cross-correlation for the simulated data in Figure 4.7. In Section 4.2.2 values for respectively an AR($p$) model can be verified by looking at the partial autocorrelation. In the diagonal plots we have high values at the first lag, indicating that the simulations certainly have dependency with the previous lag which suggests that we have an AR(1) model for both simulations. The partial cross-correlation on the off-diagonal elements suggest how much information in one simulation is explained by the other. It can be seen that there are some lags outside the confidence interval, but this behaviour can be considered as random as there are no clear trend of these occurrences.

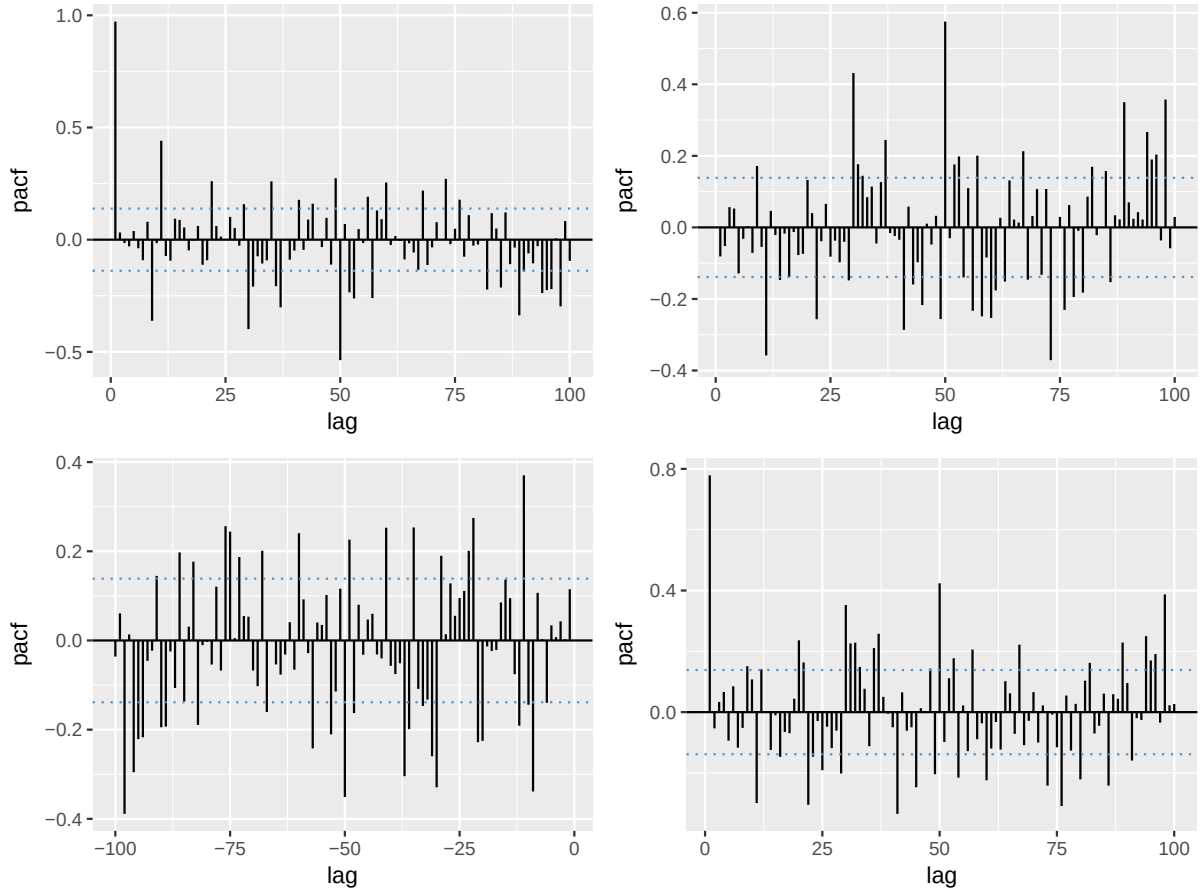


**Figure 4.9:** Partial auto- and cross-correlation functions are plotted with simulated bivariate data that are correlated with $\rho = 0.9$. The data are simulated with $\phi = 0.9$ and $\theta = 0.1$. Plotted figures placed diagonal from top left are PACF with itself while figures placed diagonal left bottom are the partial cross-correlation. The horizontal dotted blue lines are the coverage probability of 95% confidence interval computed as $\pm 1.96 n^{-1/2}$ with $n = 200$.

## 4.4 Model Fitting on Data

The principles presented in Section 4.2 and 4.3 are applied to the data presented in Chapter 3. To establish suitable values for $p$ and $q$, ACF and PACF are plotted to analyse the dependence between hours. After identifying the preferred values for the data different models will be fitted to analyse the prediction quality of the model and its performance. The optimal model will be selected based on computed log likelihood, Akaike Information Criterion (AIC) and Residual Sum of Squares (RSS).

### 4.4.1 ACF and PACF

ACF and PACF are plotted in Figure 4.10 and 4.11 for humidity and temperature data measured in September. Figure 4.10 shows that the data have a seasonal trend for each $24$ hour in both observations, $s = 24$. Addition to the seasonality, the data are tailing of as an exponential

decay. This imply that the data should include an AR term. The cross-correlation term seems to imply that there are some correlation between the observations, which was expected based on the analysis from Figure 2.5.

In Figure 4.11 temperature and humidity data cut off after different lags. Considering temperature, the data cut-off right after lag $1$, whereas humidity after lag $3$. This indicate that the model should have at most $p \leq 3$. Lag $3$ is close to the boundary of the confidence interval and thus it could be assumed that $p \leq 2$. The cross-correlation term when temperature is correlated with humidity have little significance. However, the cross-correlation between humidity and temperature have some lags outside the confidence interval, and it can be assumed that there might be some dependency with the variables when constructing models.

To include MA terms into the model the observations in ACF and PACF should be the opposite as was presented for AR, meaning a cut-off in PACF and tail-off in ACF (Wei, 2006). As this is not the case in Figure 4.10 and 4.11 it can be assumed that $q = 0$. Therefore, these observations suggest that the temperature and humidity data is a seasonal AR model with $p \leq 2$.

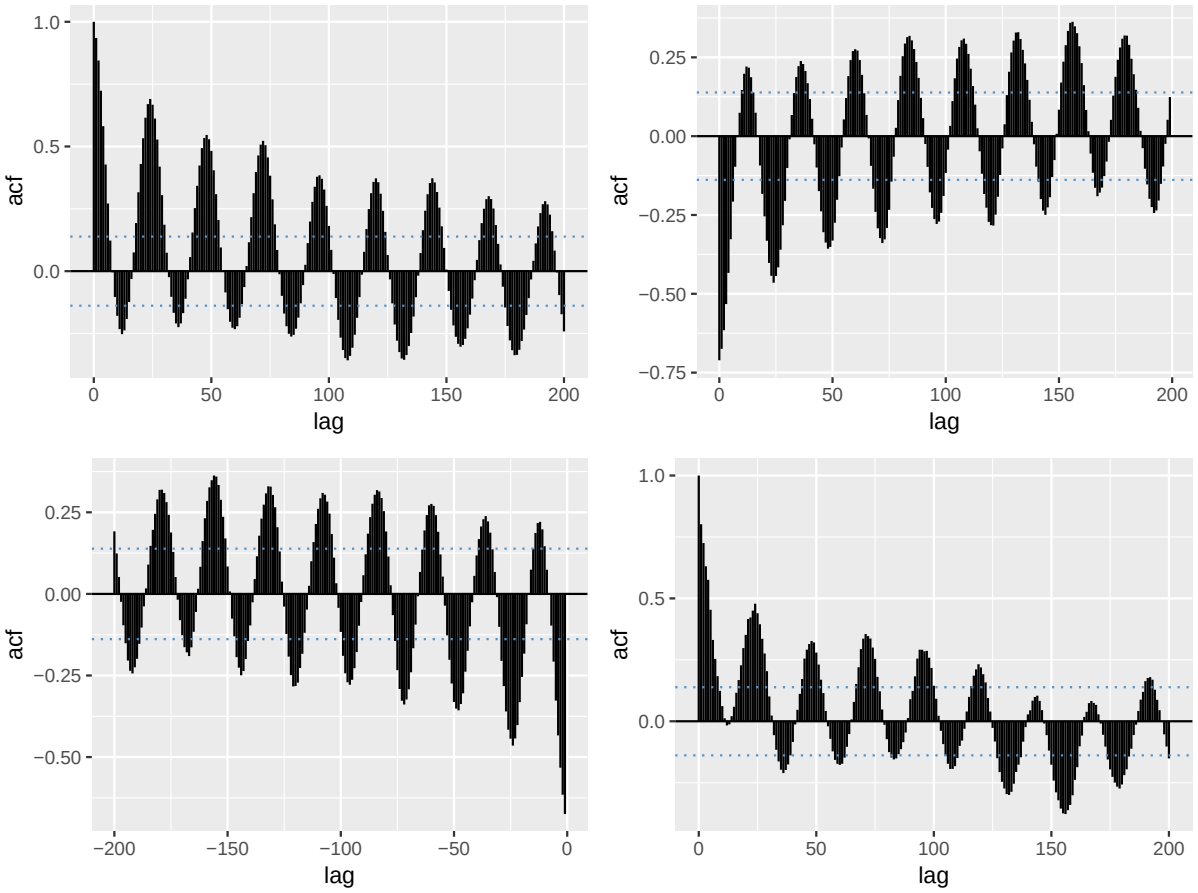


**Figure 4.10:** Auto- and cross-correlation functions are plotted with humidity and temperature data collected at NTNU in September. ACF for each observation are plotted on the diagonal while cross-correlation are on the off-diagonal. Temperature are plotted top left and humidity bottom right. The horizontal dotted blue lines are the coverage probability of 95% confidence interval computed as $\pm 1.96 n^{-1/2}$ with $n = 200$.

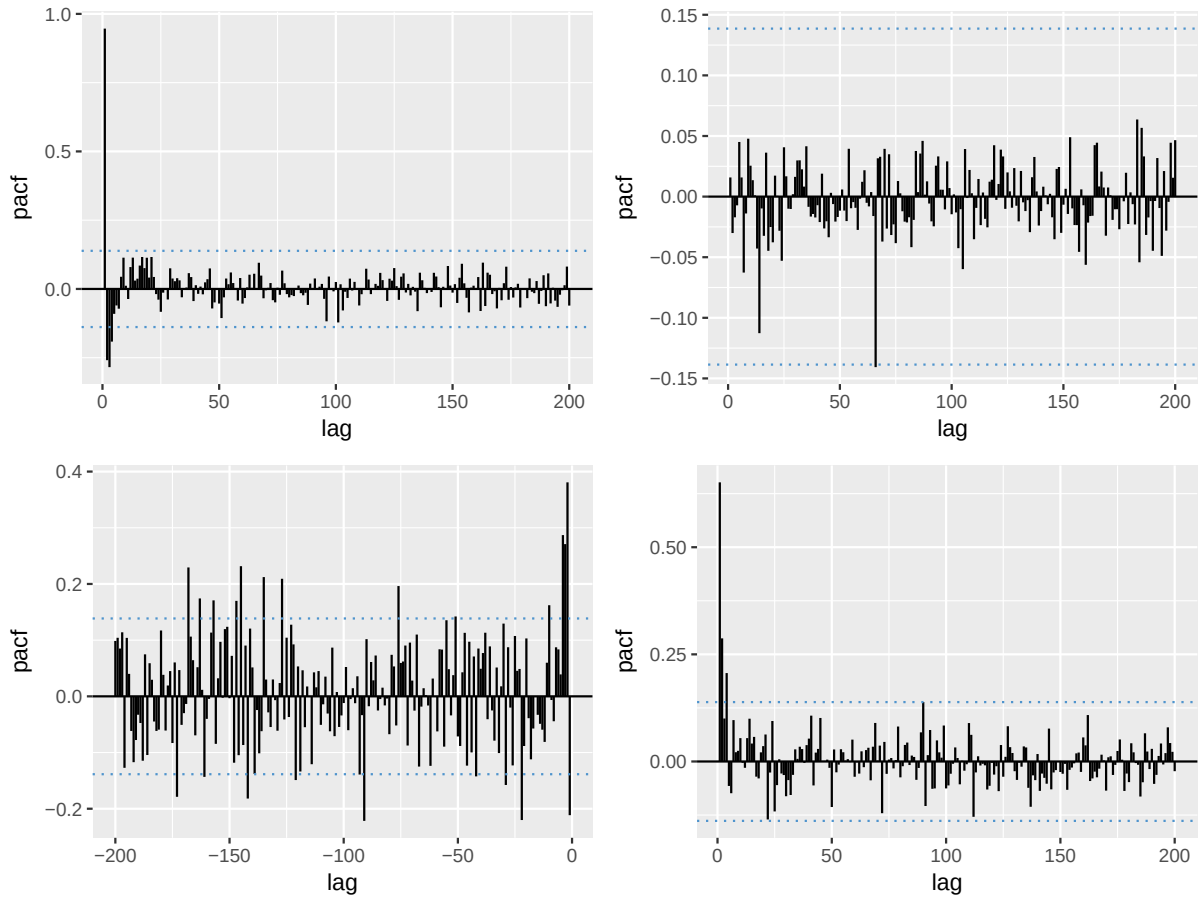


**Figure 4.11:** Partial auto- and cross-correlation functions are plotted with humidity and temperature data collected at NTNU in September. PACF for each observation are plotted on the diagonal while cross-correlation are on the off-diagonal. Temperature are plotted top left and humidity bottom right. The horizontal dotted blue lines are the coverage probability of 95% confidence interval computed as $\pm 1.96 n^{-1/2}$ with $n = 200$.

### 4.4.2 Model Fitting

In this thesis two different ways of verifying the model fitting will be considered. One is to see how the model explains the variation in the data which it is fitted on, while the other looks at how well the model predicts new data. Various models are fitted with the principles behind Occam's razor and computed log-likelihood, Aikaike Information Criterion(AIC) and Residual Sum of Squares(RSS). The log-likelihood and AIC measure of how well the model explains the variation and RSS its predictive performance. The observations in Figure 4.10 and 4.11, and suggested values of $p$, $q$ and $s$, gives an indication of how large the models should be. Hence, the previous observation helps to narrow possibilities into a limited course of action. In Figure 4.12, 4.13 and 4.14 some models with different $p$, $q$, $P$ and $Q$ are presented. Table 4.1 summarise the results from these figures and also include additional results from other models.

When evaluating the model performance, the estimated error needs to be unbiased of the model fitting. Therefore, to construct the preferred and final model data from the 100 first

observations collected in September is selected. These observations are separated into data used for model fitting and validation. Models are fitted with the function marima included in **marima** R package. To verify the performance of the model, respecting how it explains the variation in the data, log-likelihood and AIC is computed,

$$\text{loglik} = \sum_{i=1}^{N} \log P(\hat{\boldsymbol{\mu}}|Y = y_i), \tag{4.17}$$

$$\text{AIC} = -\frac{2}{N}\text{loglik} + 2\frac{d}{N}. \tag{4.18}$$

Where $P(\hat{\boldsymbol{\mu}}|Y = y_i)$ is the conditional probability when $\hat{\boldsymbol{\mu}} = f(\hat{\boldsymbol{\phi}}, \hat{\boldsymbol{\theta}})$, $y_i$ as observations at time $i$, $N$ is number of observations and $d$ correspond to number of fitted parameters (Hastie et al., 2001). However, log-likelihood compute the sum over all probabilities leaving aside the complexity of the model. Therefore, using AIC that include a penalising factor gives more weight to models with large $d$. In R this is obtained with dmvnorm from **emdbook** package used with estimated $\hat{\boldsymbol{\mu}}$ and $\hat{\boldsymbol{\Sigma}}$ computed from the marima-model.

To verify the model performance, when considering the prediction accuracy, the observed data is used to compare with the predicted values. This is computed as,

$$\text{RSS} = \sum_{i=1}^{m} (y_i - \hat{y}_i)^2, \tag{4.19}$$

with $y_i$ and $\hat{y}_i$ respectively as the observed and predicted value and summing over $m$ total number of predictions. Equation (4.19) is a general representation and can be used for validating both temperature and humidity. In addition to compute RSS for both observations the averaged RSS is also calculated. The preferred model, with respect to model fitting and validation, will be the one having smallest values of AIC and averaged RSS. Table 4.1 presents results of various combinations of $p$ and $q$, with $p, q \leq 1$. Isolating performance on the AIC and RSS gives ARMA$(1,1) \times (1,1)$ and ARMA$(0,0) \times (1,0)$ as preferred models with AIC$= -20.95$ and $\text{RSS}_{\text{Avg}} = 1053.45$ respectively. The models and their performance are plotted in Figure 4.12. Even though ARMA$(0,0) \times (1,0)$ performed well with the prediction accuracy it appears that the model explains the variation bad, and have the second worst AIC in Table 4.1. Considering ARMA$(1,1) \times (1,1)$, this model explains the data variation finest. Nonetheless, when considering the model complexity, there are other less complex models with a similar prediction accuracy. Therefore, some of the other models should be studied for additional verification. Figure 4.13 presents two simple models without seasonality, ARMA$(1,0) \times (0,0)$ and ARMA$(0,1) \times (0,0)$. Both instances have high $\text{RSS}_{\text{Avg}}$ and AIC, seen in Table 4.1. Performance of the predictions are also bad as they do not capture the seasonal behaviour. Thus, models with dependency purely on the previous time are even worse than the models presented in Figure 4.12.

**Table 4.1:** Presenting performance of different adapted models. Output of results from R with AIC, log-likelihood and RSS from Equation (4.17), (4.18) and (4.19) are presented.

| Model | LogLik | AIC | $RSS_{Temp}$ | $RSS_{Humi}$ | $RSS_{Avg}$ |
|---|---|---|---|---|---|
| $ARMA(1,0) \times (0,0)$ | $-170.11$ | $-13.53$ | 338.34 | 2198.06 | 1268.20 |
| $ARMA(0,1) \times (0,0)$ | $-194.00$ | $-15.44$ | 5494.76 | 325870.08 | 165682.42 |
| $ARMA(1,1) \times (0,0)$ | $-171.92$ | $-13.59$ | 367.57 | 2176.29 | 1271.93 |
| $ARMA(2,0) \times (0,0)$ | $-172.83$ | $-13.67$ | 362.03 | 2206.96 | 1284.50 |
| $ARMA(2,1) \times (0,0)$ | $-178.84$ | $-14.07$ | 571.23 | 5932.06 | 3251.64 |
| $ARMA(0,0) \times (1,0)$ | $-152.10$ | $-12.09$ | 308.24 | 1798.66 | **1053.45** |
| $ARMA(0,0) \times (0,1)$ | $-194.73$ | $-15.50$ | 904.28 | 19145.40 | 10024.84 |
| $ARMA(0,0) \times (1,1)$ | $-151.18$ | $-11.93$ | 1200.78 | 2194.34 | 1697.56 |
| $ARMA(1,0) \times (1,0)$ | $-210.63$ | $-16.69$ | 498.61 | 2919.20 | 1708.91 |
| $ARMA(0,1) \times (0,1)$ | $-192.94$ | $-15.28$ | 5494.08 | 65598.47 | 35546.27 |
| $ARMA(1,1) \times (1,0)$ | $-241.70$ | $-19.10$ | 311.29 | 4500.00 | 2405.65 |
| $ARMA(1,1) \times (0,1)$ | $-181.02$ | $-14.24$ | 55.71 | 6409.54 | 3232.63 |
| $ARMA(1,1) \times (1,1)$ | $-265.94$ | $\mathbf{-20.95}$ | 315.21 | 2948.71 | 1631.96 |

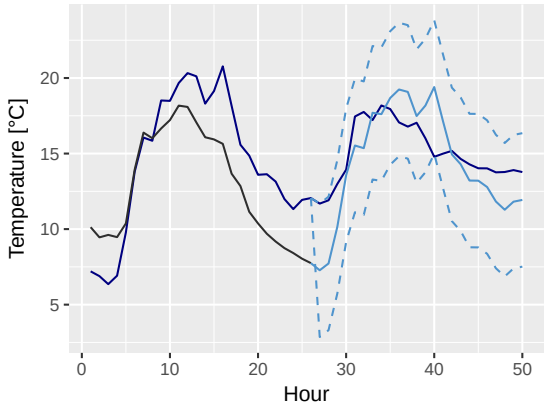


**(a)** Temperature, $ARMA(0,0) \times (1,0)$

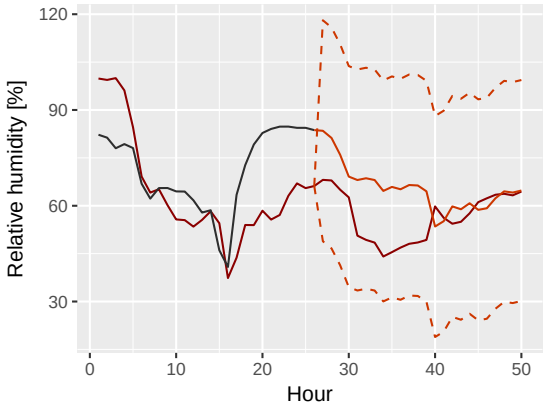


**(b)** Humidity, $ARMA(0,0) \times (1,0)$

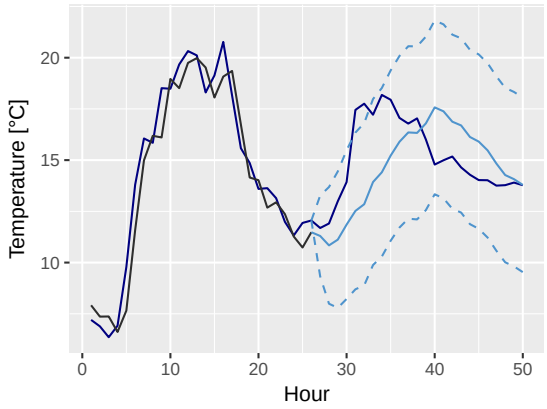


**(c)** Temperature, $ARMA(1,1) \times (1,1)$

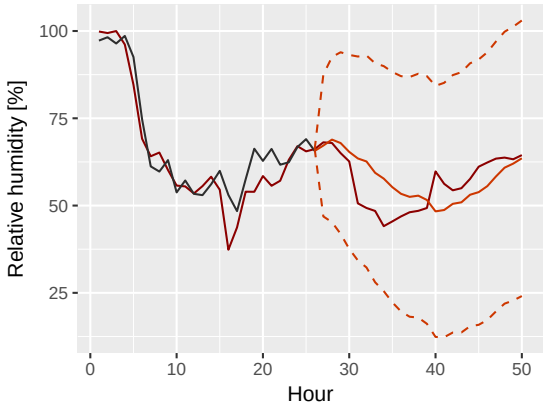


**(d)** Humidity, $ARMA(1,1) \times (1,1)$

**Figure 4.12:** Models selected with AIC and RSS from results in Table 4.1. Selected model with AIC is plotted to the bottom while the averaged RSS is plotted to the top. Dotted lines are the 95% prediction interval, black lines are the performance of the model, the dark colours are observations and light colours are predictions.

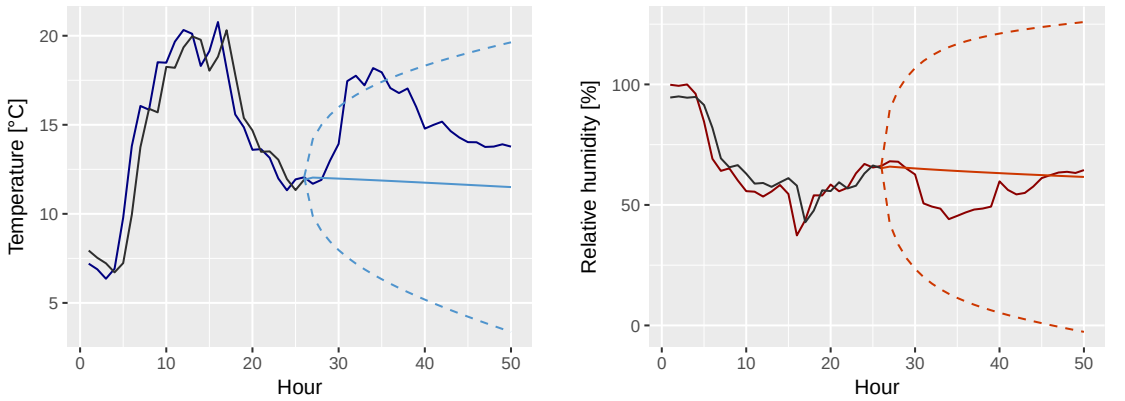


**(a)** Temperature, ARMA$(1,0) \times (0,0)$ **(b)** Humidity, ARMA$(1,0) \times (0,0)$

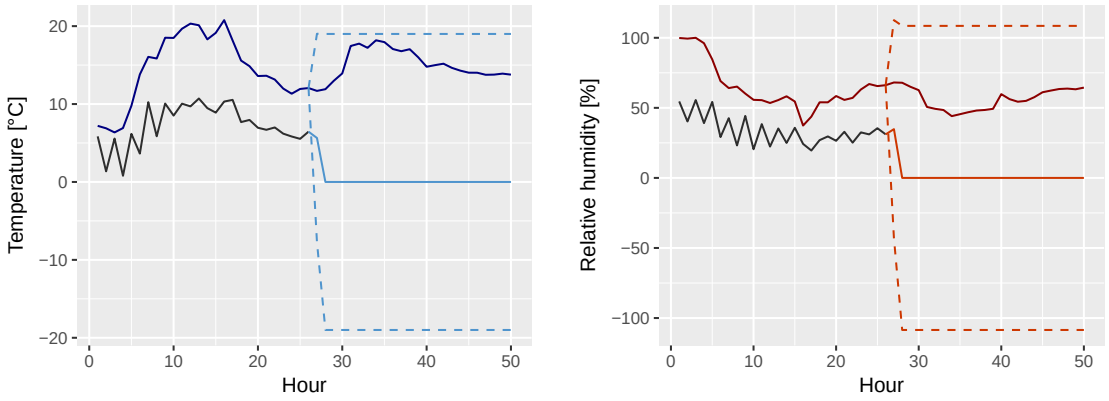


**(c)** Temperature, ARMA$(0,1) \times (0,0)$ **(d)** Humidity, ARMA$(0,1) \times (0,0)$

**Figure 4.13:** Model performance when inspecting simple models. Dotted lines are the 95% prediction interval, black lines are the performance of the model, the dark colours are observations and light colours are predictions.

From Table 4.1 the second best model with respect to AIC is ARMA$(1,1) \times (1,0)$. However, $\text{RSS}_{\text{Avg}}$ is high, and would not contribute to a well enough model. The next best is ARMA$(1,0) \times (1,0)$ with AIC $= -16.69$. In this model $\text{RSS}_{\text{Avg}} = 1708.91$ which is close to the $\text{RSS}_{\text{Avg}}$ for ARMA$(1,1) \times (1,1)$. Figure 4.14a and 4.14b present the performance of ARMA$(1,0) \times (1,0)$, and have the same behaviour as ARMA$(1,1) \times (1,1)$. Therefore, Occam's razor and $\text{RSS}_{\text{Avg}}$ would suggest ARMA$(1,0) \times (1,0)$ as the best possible model.

It was assumed from PACF in Figure 4.11, that the data should be a seasonal AR model with $p \leq 2$. Figure 4.14 compares the current most suitable model, ARMA$(1,0) \times (1,0)$, with an increased model ARMA$(2,0) \times (1,0)$. The two models have both similar behaviour to the observed temperature and humidity. Table 4.2 present the performance of the two models. The increased model have an AIC slightly better, however, $\text{RSS}_{\text{Avg}}$ is huge. The preferred model with respect to AIC and $\text{RSS}_{\text{Avg}}$ is still ARMA$(1,0) \times (1,0)$.

When fitting ARMA$(1,0) \times (1,0)$ in marima it is possible to adjust the degree of penalty. This penalty is used in order to reduce the complexity of the model. To verify the penalty size, data from the 96 first observations were divided into 4 different data set with 24 hours in each.

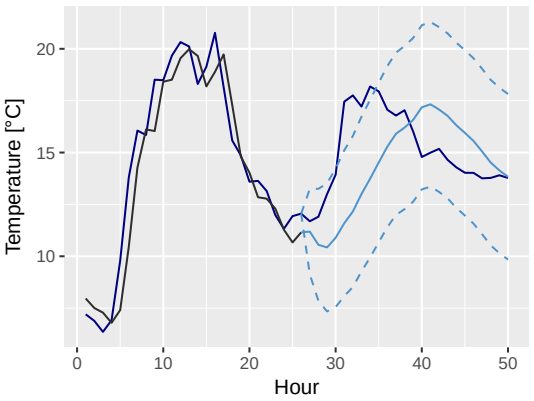


**(a)** Temperature, ARMA$(1,0) \times (1,0)$

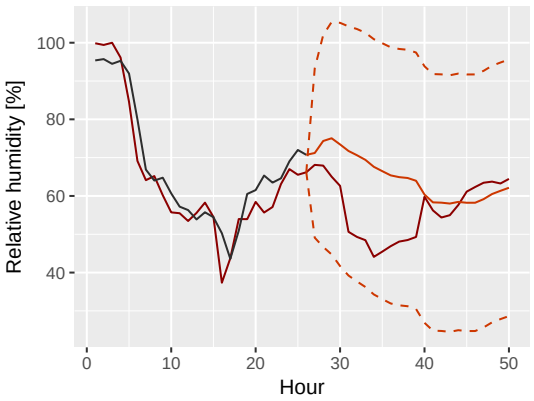


**(b)** Humidity, ARMA$(1,0) \times (1,0)$

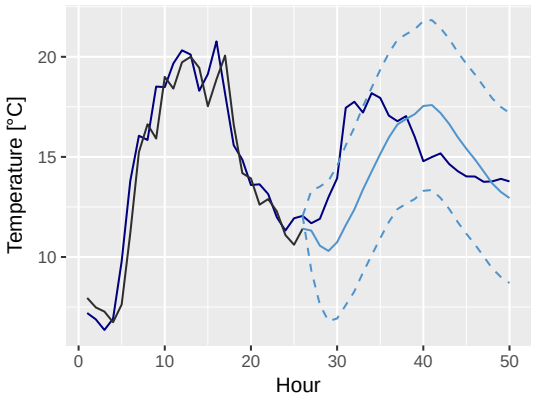


**(c)** Temperature, ARMA$(2,0) \times (1,0)$

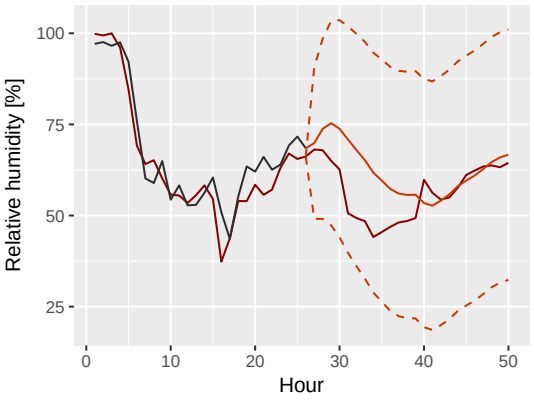


**(d)** Humidity, ARMA$(2,0) \times (1,0)$

**Figure 4.14:** Comparing model performance when $p$ is increased. Dotted lines are the 95% prediction interval, black lines are the performance of the model, the dark colours are observations and light colours are predictions.

**Table 4.2:** Presenting performance of different adapted models. Output of results from `R` with AIC, log-likelihood and RSS from Equation (4.17), (4.18) and (4.19) are presented.

| Model | LogLik | AIC | $\text{RSS}_{\text{Temp}}$ | $\text{RSS}_{\text{Humi}}$ | $\text{RSS}_{\text{Avg}}$ |
|---|---|---|---|---|---|
| ARMA$(1,0) \times (1,0)$ | $-210.63$ | $-16.69$ | 498.61 | 2919.20 | 1708.91 |
| ARMA$(2,0) \times (1,0)$ | $-226.36$ | $-17.87$ | 356.84 | 4671.29 | 2514.07 |

This is because time series are dependent on the order they are measured and information would be lost if changing the order of time steps. Nevertheless, data can be divided into subgroups as the data have a seasonality of 24 hours. Models will be fitted with three subgroups forming the training data, while the latter subgroup will test the performance of the fitted model and compute $\text{RSS}_{\text{Avg}}$. Each penalty factor, $f_{\text{pen}} \in \{0, 2, 4, 6, 8, 10, 12, 14\}$, is calculated four times to let all subsets form test data. The computed averaged $\text{RSS}_{\text{Avg}}$ for $f_{\text{pen}}$ are presented in Table 4.3.

**Table 4.3:** Presenting performance of ARMA$(1,0) \times (1,0)$ when different intensity on the penalty factor $f_{\text{pen}}$. Output are the averaged $\text{RSS}_{\text{Avg}}$ from the four different test data formed from the 96 first observations collected in September.

| $f_{\text{pen}}$ | $\text{RSS}_{\text{Avg}}$ |
|---|---|
| 0 | 1673.575 |
| 2 | 1525.989 |
| 4 | 1527.445 |
| 6 | 1503.274 |
| 8 | 1503.274 |
| 10 | 1401.485 |
| 12 | 1550.395 |
| 14 | 1550.395 |

The preferred model with respect to intensity of penalty factor would give the lowest $\text{RSS}_{\text{Avg}}$, which in this case is with $f_{\text{pen}} = 10$. Thus, ARMA$(1,0) \times (1,0)$ with $f_{\text{pen}} = 10$ is the model that will be used further when adapting the seasonal Kalman filter in Chapter 5 and monitoring in Chapter 6.

Chapter 5

# Filtering

Filtering is one common approach used in time series when predicting variables or estimating new observations that will occur in the future. When the variables are non-observable the model should look at an approach for describing the latent system. State space representations are based on the Markov property, meaning that the future of an observation is independent of the past knowledge, given the current state. In our case, with seasonality, it looks at previous data points in a specified time window (Wei, 2006). Additionally, extending into multivariate data would mean that all variables should be considered in the time window.

Kalman filter is one method that uses state space representation when estimating and forecasting for future states. Thus, this section will start with explaining the state space representation before introducing the Kalman filter for an univariate non-seasonal model. After explaining the theory the model is first increased into a seasonal model before extending the Kalman filter into a multivariate seasonal model. This is to make sure that the results obtained in Section 4.4.2 can be used in the on-line monitoring with temperature and humidity data.

## 5.1 State Space

Models built on the relationship between input and output are said to have an *external* description of the system. However, extracting information from the system can be challenging and not that transparent. In such manner would a state space representation that study the dynamics of the system and use the *internal* description of the system be more beneficial (Madsen, 2008).

A system with this challenge, and represented on state space form, have an observed random variable $Y_t$ that want to estimate the hidden unknown variable $X_t$. The relationship between $X_t$ and $Y_t$ is investigated with the *statistical inversion*. With the Bayesian way of thinking, this means that we want to compute the joint *posterior distribution* of all the states $\mathbf{x}_{0:T} = \{\mathbf{x}_0, \dots \mathbf{x}_T\}$, given all of the measurements $\mathbf{y}_{1:T} = \{\mathbf{y}_1 \dots \mathbf{y}_T\}$, and can be accomplished by using Bayes rule (Särkkä, 2002). If this were to be used in a dynamical system for on-line monitoring, computing the distribution would soon be complex and difficult. This is

because each time a new observation is registered the distribution need to be computed, which generate an increased complexity when escalating the time step. One solution is to only look at the marginal distribution of the current state and apply *Markov sequence* to the dynamic state model. The properties of a Markov sequence is that it only looks at the present state and not the past history when predicting future states (Everitt, 2014). A probabilistic way of expressing the state space model using density functions can be as,

$$\begin{aligned} \mathbf{x}_0 &\sim p(\mathbf{x}_0) \\ \mathbf{x}_t &\sim p(\mathbf{x}_t|\mathbf{x}_{t-1}) \\ \mathbf{y}_t &\sim p(\mathbf{y}_t|\mathbf{x}_t), \end{aligned} \tag{5.1}$$

where $\mathbf{x}_0$ is the initial distribution, $\mathbf{x}_t$ is the dynamical model described as a first-order Markov sequence and $\mathbf{y}_t$ is the measurement where conditional independence is assumed to hold for the measurement model i.e. $p(\mathbf{y}_t|\mathbf{x}_1, \dots \mathbf{x}_t, \mathbf{y}_1 \dots \mathbf{y}_{t-1}) = p(\mathbf{y}_t|\mathbf{x}_t)$ (Särkkä, 2002).

With some modifications a linear state space representation can be formulated on a matrix-vector form, with a system and observation equation,

$$\text{System equation:} \quad \mathbf{X}_t = \mathbf{A}\mathbf{X}_{t-1} + \mathbf{e}_{1,t} \tag{5.2}$$

$$\text{Observation equation:} \quad \mathbf{Y}_t = \mathbf{C}\mathbf{X}_t + \mathbf{e}_{2,t}. \tag{5.3}$$

Here $\mathbf{X}_t$ is a stochastic $m$-dimensional state vector based on latent states, $\mathbf{Y}_t$ is the observation vector. Both $\mathbf{e}_{1,t}$ and $\mathbf{e}_{2,t}$ are noise terms, respectively for the system and observation, and are random vectors described by,

$$\begin{aligned} \mathrm{E}[\mathbf{e}_{1,t}] &= \mathrm{E}[\mathbf{e}_{2,t}] = 0 \\ \mathrm{C}[\mathbf{e}_{1,t}, \mathbf{e}_{1,s}] &= \begin{cases} \mathrm{Var}[\mathbf{e}_{1,t}] = \boldsymbol{\Sigma}_1, & \text{for } s = t \\ 0, & \text{for } s \neq t \end{cases} \qquad (5.4) \\ \mathrm{C}[\mathbf{e}_{2,t}, \mathbf{e}_{2,s}] &= \begin{cases} \mathrm{Var}[\mathbf{e}_{2,t}] = \boldsymbol{\Sigma}_2, & \text{for } s = t \\ 0, & \text{for } s \neq t \end{cases} \qquad (5.5) \\ \mathrm{C}[\mathbf{e}_{1,t}, \mathbf{e}_{2,s}] &= 0 \quad \forall s, t \end{aligned}$$

Lastly, the matrices $\mathbf{A}$, $\mathbf{C}$, $\boldsymbol{\Sigma}_1$ and $\boldsymbol{\Sigma}_2$ are known matrices (Madsen, 2008).

Särkkä (2002) suggests in *Bayesian filtering and smoothing* to use some marginal distributions for the three different procedures in state space representation; filtering, prediction and smoothing. Using marginal distributions will only require a constant number of predictions, and are solving the complex problem. In this project the two first marginal distributions, filtering and prediction, will be presented and used further as this is what Kalman filter apply in its recursive procedure. These distributions can be explained as,

- *Prediction*: Try to predict the future state $\mathbf{X}_{t+i}$ while being in the current state, $\mathbf{X}_t$. The marginal distribution for the $i$'th future state when being in state $t$ is given as, $p(\mathbf{x}_{t+i}|\mathbf{y}_1, \mathbf{y}_2, \ldots, \mathbf{y}_t)$.
- *Filtering*: The prediction in the current position, $\mathbf{X}_t$, can be corrected based on the knowledge obtained in the observed data, $\mathbf{Y}_t$. The marginal distribution in state $t$ is given as, $p(\mathbf{x}_t|\mathbf{y}_1, \mathbf{y}_2, \ldots, \mathbf{y}_t)$.

In the Kalman filter, working for linear systems as in Equation (5.2) and (5.3), the correction is a linear combination between the old prediction and the current prediction error which will be seen in the next section.

## 5.2 Kalman Filter

The marginal distribution $p(\mathbf{x}_t|\mathbf{y}_{1:t})$ that solves the filtering problem in Section 5.1 should be computed at time $t$ for state $\mathbf{X}_t$. Each time step is computed with respect to the previous observation until the current time $t$. The Bayesian filtering can be arranged as a Kalman filter which is a closed form solution to the filtering problem, and uses the same equations from the state space representation, Equation (5.2) and (5.3).

To obtain the optimal reconstruction and prediction with Kalman filtering, and also other closed form solutions for the Bayesian inference, prediction and reconstruction steps access the previous estimations. Before starting the recursion of these steps the prior knowledge in the model is defined as,

$$\text{Initialisation: } \begin{cases} \hat{\mathbf{X}}_{1|0} = & \mathrm{E}[\mathbf{X_1}] = \boldsymbol{\mu}_0 \\ \boldsymbol{\Sigma}^{xx}_{1|0} = & \mathrm{V}[\mathbf{X}_1] = \mathbf{V}_0 \\ \boldsymbol{\Sigma}^{yy}_{1|0} = & \mathbf{C}\boldsymbol{\Sigma}^{xx}_{1|0}\mathbf{C}^T + \boldsymbol{\Sigma}_2 \end{cases} \tag{5.6}$$

Here $\boldsymbol{\mu}_0$ and $\mathbf{V}_0$ are respectively the mean and covariance of $\mathbf{X}_1$, and $\boldsymbol{\Sigma}_2$ is the same as defined in Equation (5.5).

The prediction of a future value of $\mathbf{X}_t$ uses Equation (5.2) when updating for the next time step. In addition to predicting the next step the covariance in this step should also be updated and the updates are,

$$\text{Prediction: } \begin{cases} \hat{\mathbf{X}}_{t+1|t} = & \mathbf{A}\hat{\mathbf{X}}_{t|t} \\ \boldsymbol{\Sigma}^{xx}_{t+1|t} = & \mathbf{A}\boldsymbol{\Sigma}^{xx}_{t|t}\mathbf{A}^T + \boldsymbol{\Sigma}_1 \\ \boldsymbol{\Sigma}^{yy}_{t+1|t} = & \mathbf{C}\boldsymbol{\Sigma}^{xx}_{t+1|t}\mathbf{C}^T + \boldsymbol{\Sigma}_2 \end{cases} \tag{5.7}$$

where $\hat{\mathbf{X}}_{t+1|t}$ is the prediction for the next time step, $\boldsymbol{\Sigma}^{xx}_{t+1|t}$ and $\boldsymbol{\Sigma}^{yy}_{t+1|t}$ are the covariances for the variable $\mathbf{X}_t$ and observation $\mathbf{Y}_t$ respectively.

After prediction of the states, the estimates should be revised by adding a correction to the update. This is achieved by using the Kalman gain. The equations for the optimal reconstruction of the system $\hat{\mathbf{X}}_{t|t}$ and covariance $\mathbf{\Sigma}^{xx}_{t|t}$ are,

$$\text{Reconstruction: } \begin{cases} \mathbf{K}_t = & \mathbf{\Sigma}^{xx}_{1|t-1}\mathbf{C}^T\left(\mathbf{\Sigma}^{yy}_{t|t-1}\right)^{-1} \\ \hat{\mathbf{X}}_{t|t} = & \hat{\mathbf{X}}_{t|t-1} + \mathbf{K}_t\left(\mathbf{Y}_t - \mathbf{C}\hat{\mathbf{X}}_{t|t-1}\right), \\ \mathbf{\Sigma}^{xx}_{t|t} = & \mathbf{\Sigma}^{xx}_{t|t-1} - \mathbf{K}_t\mathbf{\Sigma}^{yy}_{t|t-1}\mathbf{K}_t^T \end{cases} \tag{5.8}$$

where $\mathbf{K}_t$ is the Kalman gain correcting the estimated state.

The prediction and reconstruction step in Equation (5.7) and (5.8) are used together when there are observations in the system. The reconstruction step uses $\mathbf{Y}_t$ when correcting the prediction. Therefore, when observations are missing, or we are predicting future states, the prediction step will only be considered. This is relevant when monitoring on-line processes that are predicting future states. Based on these predictions the model can plan ahead and decide because of the knowledge obtained in current time step.

## 5.3 Seasonal Kalman Filter

Before introducing the multivariate seasonal Kalman filter, an univariate seasonal model with the augmented formulations should be presented. Section 4.1 present a $24$ hour seasonal univariate ARMA model in Equation (4.6). This model look back at observations $24$ hours earlier, and also at observations one hour earlier. The seasonal model is put into state space form and formulated with principles from (4.1),

$$\begin{aligned} (1-\Phi_{24}\mathbf{B}^{24})(1-\phi_1\mathbf{B})\mathbf{X}_t =& u_t \\ (1-\phi_1\mathbf{B}-\Phi_{24}\mathbf{B}^{24}+\phi_1\Phi_{24}\mathbf{B}^{25})\mathbf{X}_t =& u_t \\ X_t-\phi_1X_{t-1}-\Phi_{24}X_{t-24}+\phi_1\Phi_{24}X_{t-25} =& u_t, \end{aligned} \tag{5.9}$$

where $\phi_1$ and $\Phi_{24}$ are respectively the weights for one hour and 24 hour terms. The state space equation have to be transformed to make it accessible and understandable for the algorithm presented in Section 5.2. Equation (5.2) and (5.3) need to be studied in order to fit the seasonality. The adjustment is that $\mathbf{A}$, $\mathbf{e}_{1,t}$ and $\mathbf{C}$ are matrices. The first two are respectively $25 \times 25$ and the latter matrix is $25 \times 1$. The reason for expansion into matrices is in order to keep track of the seasonality seen in Equation (5.9). For the system equation, with respect to $X_{t-1}$, $X_{t-24}$

and $X_{t-25}$, the recursion $24$ hours back is formulated as,

$$\begin{aligned}
\mathrm{X}_t &= \phi_1 \mathrm{X}_{t-1} + \Phi_{24} \mathrm{X}_{t-24} - \phi_1 \Phi_{24} \mathrm{X}_{t-25} \\
\mathrm{X}_{t-1} &= \mathrm{X}_{t-1} \\
\mathrm{X}_{t-2} &= \mathrm{X}_{t-2} \\
&\vdots \\
\mathrm{X}_{t-24} &= \mathrm{X}_{t-24}.
\end{aligned}$$

Hence, by defining $\mathbf{X}_t = (\mathrm{X}_t, \mathrm{X}_{t-1}, \ldots, \mathrm{X}_{t-24})$, $\mathbf{A}$ is a $25 \times 25$ matrix due to the seasonality. This also impacts the observation variables at the given time, so $\mathbf{C}$ will be $25 \times 1$. The matrices become,

$$\mathbf{A} = \begin{bmatrix}
\phi_1 & 0 & 0 & \ldots & 0 & \Phi_{24} & -\phi_1 \Phi_{24} \\
1 & 0 & 0 & \ldots & 0 & 0 & 0 \\
0 & 1 & 0 & \ldots & 0 & 0 & 0 \\
\vdots & & \ddots & & & & \vdots \\
\vdots & & & \ddots & & & \vdots \\
0 & 0 & 0 & \ldots & 1 & 0 & 0 \\
0 & 0 & 0 & \ldots & 0 & 1 & 0
\end{bmatrix}$$

$$\mathbf{C} = \begin{bmatrix} 1 & 0 & 0 \ldots & 0 & 0 \end{bmatrix}$$

In addition to the matrices corresponding to the state space model the variance of the random noise should also be written with respect to the augmented form with seasonality. The variance to the process is of the size $25 \times 25$ as it consider the uncertainty in the system we are working on. Because the variance of the process should be counted for one time, at the current time $t$, $\sigma^2_{\text{Pro}}$ will only be mentioned in position $(1, 1)$ in the matrix. The other variance $\sigma^2_{\text{Obs}}$ are with respect to the observation and of the size $1 \times 1$ as it is only one observation for each time step.

$$\mathbf{\Sigma}_1 = \begin{bmatrix}
\sigma^2_{\text{Pro}} & 0 & \ldots & 0 & 0 \\
0 & 0 & \ldots & 0 & 0 \\
\vdots & & \ddots & & \vdots \\
0 & 0 & \ldots & 0 & 0
\end{bmatrix}$$

$$\mathbf{\Sigma}_2 = \sigma^2_{\text{Obs}}$$

Finally, the seasonal ARMA model from Equation (4.6) can be formulated on a state space

form with 25 latent variables at each time step. The values that are used for $\phi_1$ and $\Phi_{24}$ can be chosen from a fitted ARMA$(1,0) \times (1,0)$ model. Additionally, the seasonal representation of Kalman filter with the augmented version can be extended further to a multivariate seasonal Kalman filter.

## 5.4 Multivariate Seasonal Kalman Filter

The data used in this project are multivariate with two observations, temperature and humidity. Additionally, the results in Section 4.4.2 suggest a multivariate ARMA$(1,0) \times (1,0)$ model. Thus, a multivariate seasonal Kalman filter should be implemented in the on-line monitoring. This requires the results in Section 5.3 to be augmented further. Equation (5.9) present the seasonal ARMA$(1,0) \times (1,0)$ model on state space form with $\mathbf{X}_t = (\mathrm{X}_t, \mathrm{X}_{t-1}, \ldots, \mathrm{X}_{t-24})$ for respectively one variable.

Before introducing the full system with complete extension of matrices a simple case with dependency only on the previous lag is considered, meaning a bivariate AR(1) model. Define $\mathbf{X}_{j,t}$ with $j \in \{A, B\}$ at time $t$ as,

$$\mathbf{X}_t = \begin{bmatrix} X_{A,t} \\ X_{B,t} \end{bmatrix}. \tag{5.10}$$

The computed weights with dependency to the previous lag are defined as $\phi_{j,1}$ and $\phi_{j'j,1}$ with $j' \in \{A, B\} \neq j$. The latter weight resemble the contribution of the alternate variable $j'$ when predicting the status on variable $j$. Defining the observations $\mathbf{Y}_{j,t}$ similarly as Equation (5.10). Then the total set of system and observation equations for a bivariate AR(1) model are similar to Equation (5.2) and (5.3) and becomes,

$$\begin{bmatrix} X_{A,t} \\ X_{B,t} \end{bmatrix} = \begin{bmatrix} \phi_{A,1} & \phi_{AB,1} \\ \phi_{BA,1} & \phi_{B,1} \end{bmatrix} \begin{bmatrix} X_{A,t-1} \\ X_{B,t-1} \end{bmatrix} \tag{5.11}$$

$$\begin{bmatrix} Y_{A,t} \\ Y_{B,t} \end{bmatrix} = \begin{bmatrix} 1 & 0 \\ 0 & 1 \end{bmatrix} \begin{bmatrix} X_{A,t} \\ X_{B,t} \end{bmatrix}. \tag{5.12}$$

The weights in $\mathbf{A}$ are computed when fitting a model with marima in R. Further, the recursion in Equation (5.7) and (5.8) require covariances for $\mathbf{X}_t$ and $\mathbf{Y}_t$, the uncertainty in process and observation, respectively $\mathbf{\Sigma}_1$ and $\mathbf{\Sigma}_2$,

$$\mathbf{\Sigma}_1 = \begin{bmatrix} \sigma^2_{A,\text{Pro}} & \sigma^2_{AB,\text{Pro}} \\ \sigma^2_{BA,\text{Pro}} & \sigma^2_{B,\text{Pro}} \end{bmatrix} \tag{5.13}$$

$$\mathbf{\Sigma}_2 = \begin{bmatrix} \sigma^2_{A,\text{Obs}} & 0 \\ 0 & \sigma^2_{B,\text{Obs}} \end{bmatrix} \tag{5.14}$$

To accommodate the requirements from Section 4.3 the bivariate model should increase number of dependent lags into a $24$ hour seasonality. Including the seasonal dependency $\mathbf{X}_t$ should be extended to,

$$\mathbf{X}_t = \begin{bmatrix} X_{A,t} \\ X_{B,t} \\ X_{A,t-1} \\ X_{B,t-1} \\ \vdots \\ X_{A,t-24} \\ X_{B,t-24} \end{bmatrix}$$

The size of $\mathbf{A}$ in Equation (5.11) is $2 \times 2$ because the two variables are only depending on the previous lag. If number of dependent lags is increased, then each time step for a bivariate system will have a sub-matrix of size $2 \times 2$ together forming $\mathbf{A}$. Thus, with the increase of $\mathbf{X}_t$ into a $50 \times 1$ matrix $\mathbf{A}$ becomes $50 \times 50$. For simplicity, assume $\mathbf{A}$ can be organised with sub-matrices of $2 \times 2$ as,

$$\mathbf{a}_i = \begin{bmatrix} \phi_{A,i} & \phi_{AB,i} \\ \phi_{BA,i} & \phi_{B,i} \end{bmatrix} \tag{5.15}$$

with $i$ indicating which lag current time are dependent on and how much weighted it is. Adding these matrices together would form $\mathbf{A}$,

$$\mathbf{A} = \begin{bmatrix} \mathbf{a}_1 & \mathbf{0} & \dots & \mathbf{0} & \mathbf{a}_{24} & \mathbf{a}_1\mathbf{a}_{24} \\ \mathbf{I} & \mathbf{0} & \dots & \mathbf{0} & \mathbf{0} & \mathbf{0} \\ \mathbf{0} & \mathbf{I} & \dots & \mathbf{0} & \mathbf{0} & \mathbf{0} \\ \vdots & & \ddots & & & \vdots \\ \vdots & & & \ddots & & \vdots \\ \mathbf{0} & \mathbf{0} & \dots & \mathbf{I} & \mathbf{0} & \mathbf{0} \\ \mathbf{0} & \mathbf{0} & \dots & \mathbf{0} & \mathbf{I} & \mathbf{0} \end{bmatrix} \tag{5.16}$$

with $\mathbf{I}$ and $\mathbf{0}$ as respectively the identity and zero matrix with size $2 \times 2$.

Then $\mathrm{C}$ in the observation equation becomes $2 \times 50$,

$$\mathrm{C} = \begin{bmatrix} 1 & 0 & 0 & \dots & 0 & 0 & 0 \\ 0 & 1 & 0 & \dots & 0 & 0 & 0 \end{bmatrix}$$

The covariances for $\mathbf{X}_t$ and $\mathbf{Y}_t$ follow the same procedure as when increasing into a seasonal

univariate model and use the covariances from Equation (5.13) and (5.14),

$$\boldsymbol{\Sigma}_1 = \begin{bmatrix} \begin{bmatrix} \sigma^2_{A,\text{Pro}} & \sigma^2_{AB,\text{Pro}} \\ \sigma^2_{BA,\text{Pro}} & \sigma^2_{B,\text{Pro}} \end{bmatrix} & \begin{bmatrix} 0 & 0 \\ 0 & 0 \end{bmatrix} & \cdots & \begin{bmatrix} 0 & 0 \\ 0 & 0 \end{bmatrix} \\ \begin{bmatrix} 0 & 0 \\ 0 & 0 \end{bmatrix} & \begin{bmatrix} 0 & 0 \\ 0 & 0 \end{bmatrix} & \cdots & \begin{bmatrix} 0 & 0 \\ 0 & 0 \end{bmatrix} \\ \vdots & & \ddots & \vdots \\ \begin{bmatrix} 0 & 0 \\ 0 & 0 \end{bmatrix} & \begin{bmatrix} 0 & 0 \\ 0 & 0 \end{bmatrix} & \cdots & \begin{bmatrix} 0 & 0 \\ 0 & 0 \end{bmatrix} \end{bmatrix}$$

$$\boldsymbol{\Sigma}_2 = \begin{bmatrix} \sigma^2_{A,\text{Obs}} & 0 \\ 0 & \sigma^2_{B,\text{Obs}} \end{bmatrix}$$

In summary, the bivariate SAR$(1) \times (1)$ model can be formulated on a state space form with 25 latent observations for both variables at each time step. Recall Section 4.4.2 with model fitting and constructing models. The values that are used in the Kalman filter were chosen from the fitted multivariate ARMA$(1, 0) \times (1, 0)$ with the 100 first data points from the north-facing solar panel. The weights are,

$$\mathbf{a}_1 = \begin{bmatrix} -1.002 & -0.029 \\ 0.0 & -0.866 \end{bmatrix}$$
$$\mathbf{a}_{24} = \begin{bmatrix} -0.389 & 0.023 \\ 0.0 & -0.360 \end{bmatrix}$$

This shows that following observations are more dependent on the previous time step than $24$ hours earlier. In addition, the two variables are mostly explained by their previous observations, and $\phi_{AB,1}$ and $\phi_{AB,24}$ are small so most probably insignificant during monitoring. The linear state space model makes it possible for us to use methods, such as the Kalman filter, when studying on-line monitoring schemes.

Chapter 6

# Monitoring

The models and methods that have been presented in the previous chapters are based on collected data and have been implemented into an on-line monitoring process, with a goal of reducing the number of observations and maximising energy output. Collecting information is done by either measuring observations or predicting observations using the predictive model from Section 5.4. This on-line monitoring can possibly take part in a bigger IoT system to obtain efficient data collection and monitoring of devices in systems such as smart houses.

In this chapter we will look into what happens when monitoring an on-line process with criteria to obtain *i)* energy surplus and *ii)* accuracy on predictions. The criteria use a threshold to tell when to observe the temperature and humidity rather than just predicting future observations without conducting measurement at the current time. To have models with a specific purpose, that make decisions based on the value of information, can assist the data collecting and make the monitoring more energy efficient (Eidsvik et al., 2015). Because there are multiple preferences in this monitoring the threshold could be combined into a multicriteria optimisation with a trade-off between the different objectives. As there are possibilities to obtain various optimal solutions, similar principles as in a Pareto optimal solution is considered (Doumpos and Zopounidis, 2014).

In all scenarios the principles and equations from Section 5.2 and 5.4 are used, Equation (5.6), (5.7) and (5.8). Temperature and humidity observations from the first 100 hours in the north-facing solar panel collected in September have been used to construct the model. The proceeding data are used for monitoring over a 7 days interval. Because the model is implemented with respect to an energy surplus, no energy will be saved to charge the battery, thus, the battery percentage will either be constant or diminish. This on-line monitoring has been implemented to a general bivariate case and any data with a 24-hour seasonal trend could in principle be used in this optimisation.

This chapter will start by presenting the two different objectives, maximising energy output and reducing the number of observations, and how they are computed. Further, three scenarios with different weights will be examined; close to the different objectives, *i)* or *ii)*, and a case

with both objectives treated equally. The last part in this chapter will consist of a comparison between the different constraints. The solutions will be compared with the total amount of energy surplus and RSS defined in Equation (4.19) computed for temperature and humidity.

## 6.1 Objectives

Composing energy efficient processes with required performance accuracy depend on how the system is defined and the given constraints. Because the two objectives, prediction accuracy and energy surplus, have different goals their constraints are defined individually in the following sections. A generic flow of the on-line monitoring is presented as a decision tree in Figure 6.1. The tree visualise the process handled at each time step during the monitoring. The first step

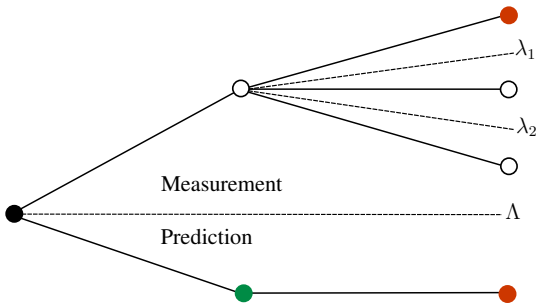


**Figure 6.1:** Visualising the behaviour of the monitoring and how decisions are managed based on the comparison with the threshold values $\Lambda$, $\lambda_1$ and $\lambda_2$. Green circle indicate if a prediction is executed and red circle if an observation is made, and some battery percentage is transmitted.

at threshold $\Lambda$ decides whether to *a)* measure temperature and humidity or *b)* predict the next observations. Prediction is indicated by a point coloured green. The model will always give a surplus of energy when predicting, which is symbolised with a red point in the figure. However, if the decision is to measure the next temperature and humidity there are several outcomes, a surplus of energy, no surplus of energy or a diminishing level on the battery charging percentage. The latter case arises when the intake on the battery is lower than what is required to operate the system. The red coloured point for measurements is also representing the surplus of energy in this instance. Table 6.1 presents the four different scenarios during monitoring from Figure 6.1 which will be used when presenting the results in the on-line monitoring in the following sections.

**Table 6.1:** Table presenting the information that can be read from Figure 6.1. Here $\overline{\text{Red}}$ and $\overline{\text{Green}}$ correspond to the decisions that are not coloured.

| Circle | Description |
|---|---|
| $\circ_{\text{Red}}$ | Transferred energy surplus |
| $\circ_{\overline{\text{Red}}}$ | Less or just enough energy to operate the system |
| $\circ_{\text{Green}}$ | Predicting |
| $\circ_{\overline{\text{Green}}}$ | Measuring |

During monitoring, the two objectives will activate threshold $\Lambda$ at different performances. Nevertheless, the consequence of reaching the threshold is similar, and a generic process for all monitoring cases is outlined in Algorithm 1. The same threshold values from Figure 6.1 are also used in this representation. This monitoring is repeated until iteration length $T$ is reached, which in this case is 7 days.

**Algorithm 1** Pseudo code for on-line monitoring

```
Initialise:
    Iteration length T
    Threshold Λ, λ1 and λ2
    Time step t0
    Data points for X_Temp and X_Humi at t0
    Gradient on battery, Grad_Bat, at t0
while t < T do
    if P(X_Temp, X_Humi) and/or Grad_Bat < Λ then
        Measure X_Temp and X_Humi at t + 1 and t + 2
        Compute Grad_Bat
        if Grad_Bat is < λ2 then
            Battery is reduced
        else if Grad_Bat is > λ1 then
            Energy transfer
            Battery is constant
        else
            No energy transfer
            Battery is constant
        t ← t + 2
    else
        Use predictive model to predict X_Temp and X_Humi at t + 1
        Compute predicted Grad_Bat
        t ← t + 1
```

In the following sections the two objectives will be illustrated and defined separately. Their respective activation thresholds, $P(X_{\text{Temp}}, X_{\text{Humi}})$ and $\text{Grad}_{\text{Bat}}$, will be presented more in depth. Additionally, results on the monitoring is commented and compared with each other before combining them into a monitoring with multicriteria constraints.

### 6.1.1 Energy Surplus

Energy surplus appears when the solar panel system produces more energy than it takes to keep the battery discharging at a constant level. One looks at whether the battery status increases or decreases, without considering the uncertainty in the predictions. The threshold $\Lambda$ will be activated if the predicted battery status increases sufficiently to obtain energy surplus in addition to measure observations. To avoid confusion, in this section $\Lambda = \Lambda_{\text{Bat}}$. From Chapter 2 it was specified that humidity and temperature are correlated with the battery status in the solar

panel. Thus, we can formulate a linear model on the battery, $X_{\text{Bat}}$, with respect to measured or predicted temperature and humidity, $X_{\text{Temp}}$ and $X_{\text{Humi}}$. The linear model is,

$$X_{\text{Bat}} = 99.39 - 0.31X_{\text{Temp}} - 0.10X_{\text{Humi}}. \tag{6.1}$$

To verify the variation on the previous and current battery status, either measured or predicted, temperature and humidity observations are inserted into the model and the current and previous battery status are divided on each other. Define$X_{\text{Bat}_1}$ and $X_{\text{Bat}_2}$ as respectively the previous and current computed battery percentage, and $\Lambda_{\text{Battery}} = 1$ as the threshold for activation as in Figure 6.1 and Algorithm 1. The threshold can be formulated as,

$$\frac{X_{\text{Bat}_1}}{X_{\text{Bat}_2}} < \Lambda_{\text{Battery}}. \tag{6.2}$$

Hence, the division explains the relationship between the current and previous battery status, i.e. if current battery is lower than the previous battery status we have a decreasing slope and would request to use the predictive model as presented in Algorithm 1.

In addition to this division, as the threshold is activated when the division indicates an increase in the battery, the computation has to look at the battery amount used in operating the sensor as well. In Figure 6.2 three intervals on battery status from randomly selected nights are plotted. These instances follow a slope $a_{\text{slope}}$ more or less with $0.99$ reduction per time step and correspond to the battery usage of the system when there is no possibility of charging.

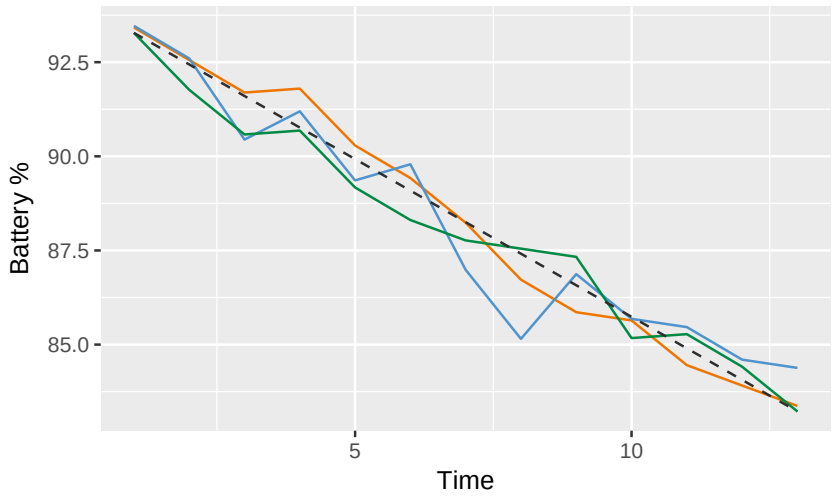


**Figure 6.2:** Three selected night intervals with a decreasing trend are plotted together in different colours. The dashed line has a reduction of 0.99 percentage points each time step, and are plotted to visualise the decrease in the battery percentage.

Energy output is computed at each hour with the discovery from Figure 6.2 and Equation (6.1) and (6.2), computed as,

$$X_{\text{Surplus}} = \frac{X_{\text{Bat}_2}}{X_{\text{Bat}_1}} - 0.99\beta, \quad \text{with} \quad \beta \in \{0, 1\}. \tag{6.3}$$

The binary variable $\beta$ indicate if a prediction(0) or a measurement(1) is conducted. The relationship between the customised energy surplus $X_{\text{Surplus}}$ in this thesis and the true energy surplus is unknown. Here energy surplus is measured as the accumulated effort to avoid the battery to discharge. The battery discharging is measured as a relative change in the battery charging and as such is measured as a percentage. Based on this assumption, energy surplus will then be dependent on the battery characteristics that is not investigated further in this thesis. Hence, any inference done on energy output and surplus is solely based on a comparison between different scenarios studied here.

If threshold in Equation (6.2) is not activated it suggests using the predictive model. This will always give an energy surplus, as there are no operational costs on the system. However, if the threshold is activated it should be verified that the slope is large enough to measure temperature and humidity and also get some energy surplus. Thus, an additional threshold is added,

$$\frac{X_{\text{Bat}_2}}{X_{\text{Bat}_1}} < \lambda_2, \tag{6.4}$$

here $\lambda_2 = a_{\text{slope}}$ and the inequality sign verify if the decrease is lower than operating the system. $X_{\text{Bat}_1}$ and $X_{\text{Bat}_2}$ are now computed with the new observations. In Figure 6.1 another threshold was also mentioned, $\lambda_1$, and are the same value as $\Lambda_{\text{Battery}}$ and verify if there is some energy output after getting the new observations. The final instance, when neither of the thresholds are activated, indicate that we have just enough energy to operate the system.

The monitoring and results are obtained from various assumptions on the battery. Some of the assumptions have already been presented and verified, such as the linear model from Equation (6.1) and $a_{\text{slope}}$ in Figure 6.2. Additionally, some other assumptions are presented in the following.

**Battery Assumptions**

- The battery percentage will never increase during this monitoring.
- Transfer of energy surplus from battery charging percentage is $1:1$.
- Conducting a prediction would mean that 100% of the energy from the solar panels is energy surplus.
- Battery performance can be presented as a linear model with respect to humidity and temperature observations.
- Battery usage when it is not charging has a slope of 0.99 reductions per time step.
- Battery percentage cannot go above 100%.

In this display, we have chosen the uncertainty of the battery status computed from the temperature variance introduced in Section 5.4, with a $95\%$ prediction interval increasing with expanding the number of predictions. Simulations are computed with $150$ iterations and the presented thresholds from (6.2) and (6.4). The red and green dots in Figure 6.1 are taken into consideration and are also plotted when showing the performance of the simulations.

Figure 6.3 shows the performance of the observations and predictions respectively for temperature and humidity, and Figure 6.4 presents the status on the battery and the energy surplus development. It can be seen that the battery remains constant during the whole monitoring. This is because the threshold would allow for measurements exclusively when battery slope is increasing, which only happens at the beginning of the monitoring. The monitoring decides, after $75$ hours, to only include predictions causing large uncertainty and unreliable model performance. This could be because temperature and humidity are inverse correlated and after $75$ hours the contrast between them become smaller. Then, computing the relationship between current and previous predictions with Equation 6.1 becomes less distinctive. Thus, the model would decide to predict and transfer energy. Additionally, the only instance that would cause a decrease is if the new measured observations is lower than what is required in operating the system causing a reducing slope. In this monitoring it occurs one time, at around $75$ hours.

The red dots plotted in all figures represent the surplus of energy and a blank space between indicating that there is only enough to operate the system. This monitoring seems to transfer energy to other instances most of the time, which is the purpose of the model as no other requirements are specified, and total amount of transferred energy is above $100$. However, the uncertainty in the battery status also increases when the number of predictions increases. Thus, there is a reason to doubt if the battery really is constant during the 7 days of monitoring. Additionally, the green dots represent if predictions take place and blank spaces are when the threshold is activated and an observation is added. The total RSS from Equation (4.19) from Section 4.4.2 becomes $\text{RSS}_{\text{Temp}} = 896.41$ and $\text{RSS}_{\text{Humi}} = 90871.88$, which is too high, and is because this model lack in tracking the performance of temperature and humidity. Therefore, it should be considered to include some constraints on the uncertainty.

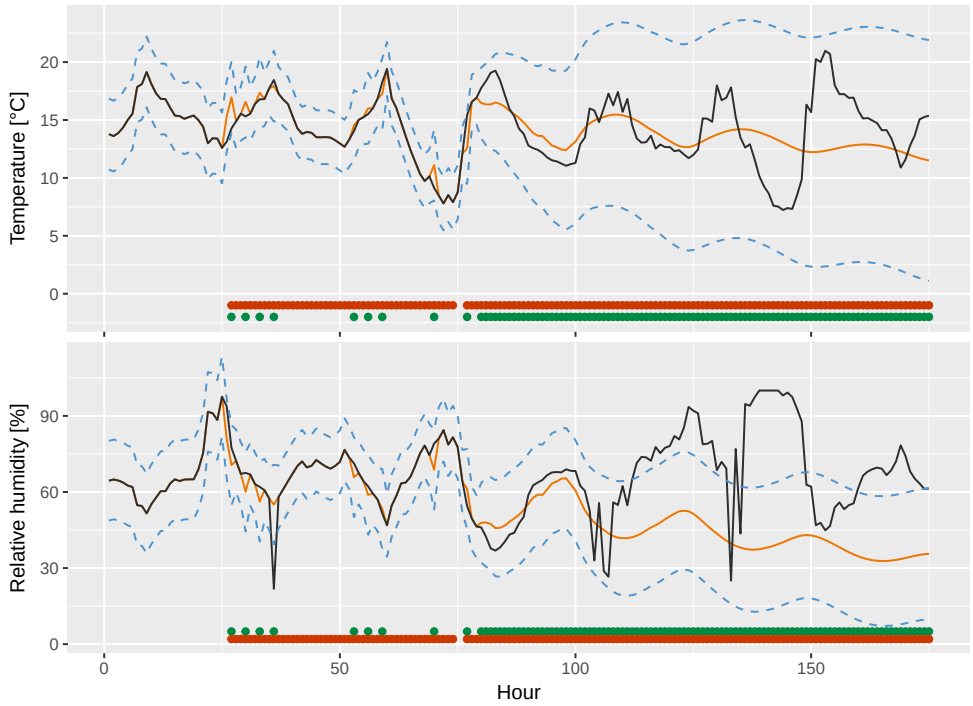


**Figure 6.3:** Predicted temperature and relative humidity plotted in orange with a 95% prediction interval presented in dotted blue lines. The black line is the real data collected from the solar panel. The red and green circles represent the decisions presented in Figure 6.1 and Table 6.1.

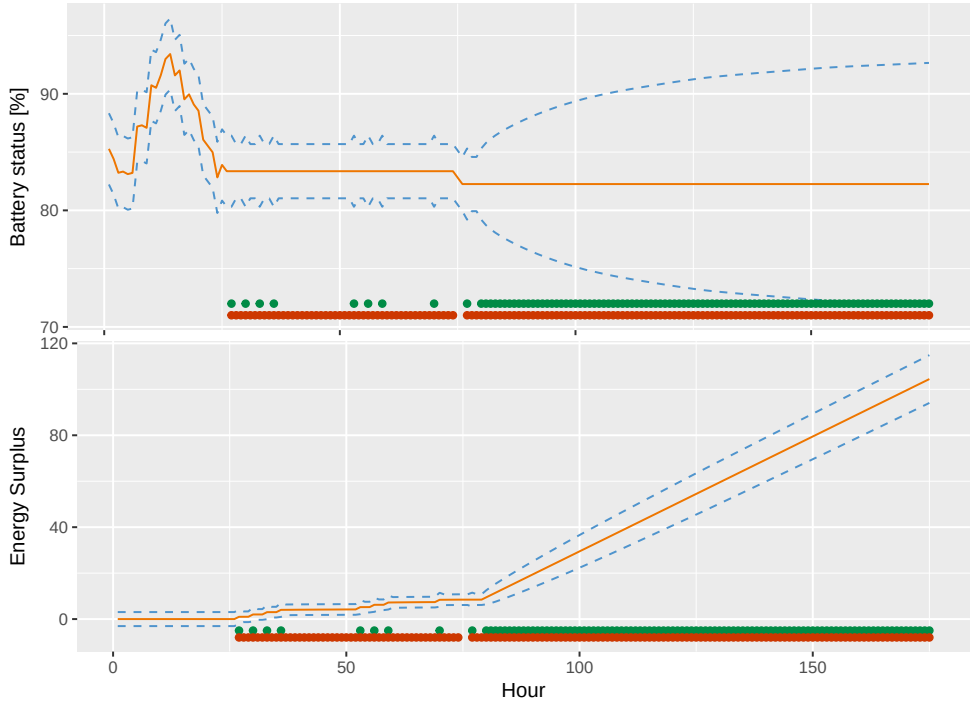


**Figure 6.4:** Behaviour of the battery when threshold (6.2) and (6.4) are used as activation threshold. Orange line in the upper plot is assumed battery status while lower plot is the development of accumulated energy surplus. Dotted blue lines are 95% prediction interval computed from the variance of the temperature. The red and green circles represent the decisions presented in Figure 6.1 and Table 6.1.

### 6.1.2 Prediction Accuracy

One method to obtain energy-efficient processes would be to reduce the number of measurements as presented in Section 6.1.1. The optimal procedure would be to have accurate predictions most of the time and ignore the possibility of measuring. However, this would result in a significant weakness of the performance as visualised in Figure 6.5. This can be solved with a trade-off between measurements and predictions, to make sure that enough information is stored in the model.

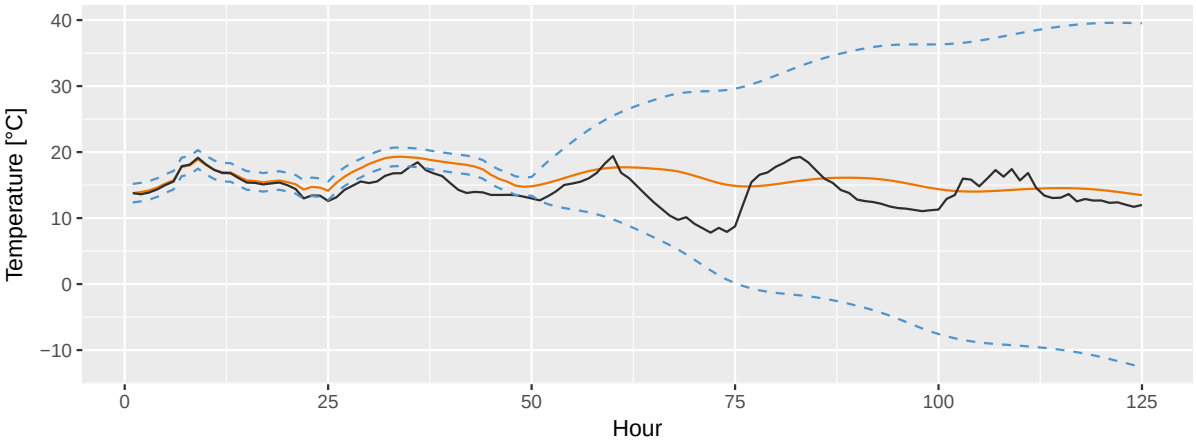


**Figure 6.5:** Performance of the Kalman filter when predicting 100 hours ahead. The black line is the observed temperature while the orange is the predicted temperatures. The dashed blue lines are the corresponding 95% prediction interval.

To validate the future actions, whether to predict or measure temperature and humidity observations, a multivariate normal distribution is introduced. The multivariate probability in this scenario computes the probability of staying in a specified interval and compare with the threshold $\Lambda = \Lambda_{\text{Prediction}}$ from Figure 6.1. The probability with a threshold is formulated as,

$$X_{\text{Prob}} = P\left(X_{\text{Temp}} \in [\xi_{T_1}, \xi_{T_2}], X_{\text{Humi}} \in [\xi_{H_1}, \xi_{H_2}]\right) < \Lambda_{\text{Prediction}}. \tag{6.5}$$

$\xi$ with either $T$ or $H$ indicate boundary of respectively temperature and humidity with 1 and 2 representing the lower and upper bound. $\Lambda_{\text{Prediction}}$ is the activation threshold when the probability of staying within the interval is too low. The dynamic variance with respect to number of predictions is also considered for each computation. The goal of the monitoring constraint is to predict an event that is outside defined boundaries $\xi$, i.e. if the probability of being inside $\xi$ is less than $\Lambda_{\text{Prediction}}$ observations should be added into the model.

The sizes of the two boundaries $\xi_T$ and $\xi_H$ are chosen from the data seen in the $100$ first hours when constructing the model, and try to capture the area where most of the normal behaviour is occurring. The boundaries are seen in Figure 6.6 with the $100$ first hours plotted for temperature and humidity, and are respectively $\xi_T \in [12, 18]$ and $\xi_H \in [35, 75]$. If the computed probability is below $\Lambda_{\text{Prediction}}$ it means that the predictions or observations could be outside this domain and

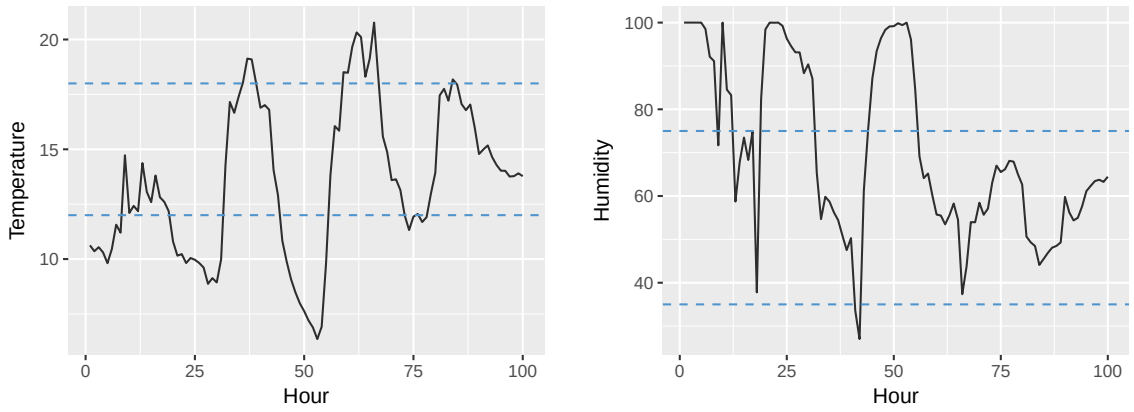


**(a)** Temperature with interval $\xi_T \in [12, 18]$ **(b)** Humidity with interval $\xi_H \in [35, 75]$

**Figure 6.6:** Presenting the 100 first hours with the chosen intervals for $[\xi_{T_1}, \xi_{T_2}]$ and $[\xi_{H_1}, \xi_{H_2}]$ to capture the typical tendency.

we should collecte measurements the next time.

To visualise the performance of Equation (6.5) temperature and humidity have been predicted using a different number of prediction length and is seen in Figure 6.7. The predictions are terminated at the same time step, and it can be seen that they have different predicted temperature and humidity. The difference between the plots emphasises how the uncertainty increase with increased prediction length. Looking at the first instance with one prediction, the prediction has more than $0.5$ expectation of being in the interval. Further, the red density plot with $5$ predictions is closer within the interval. As the uncertainty increases when raising the number of prediction the density cover a bigger region. This also applies to the latter example with $20$ predictions plotted in green.

Based on the three predictions in Figure 6.7, increasing the number of predictions from one to $5$ increases the uncertainty a lot, while going from $5$ to $20$ does not impact the uncertainty that

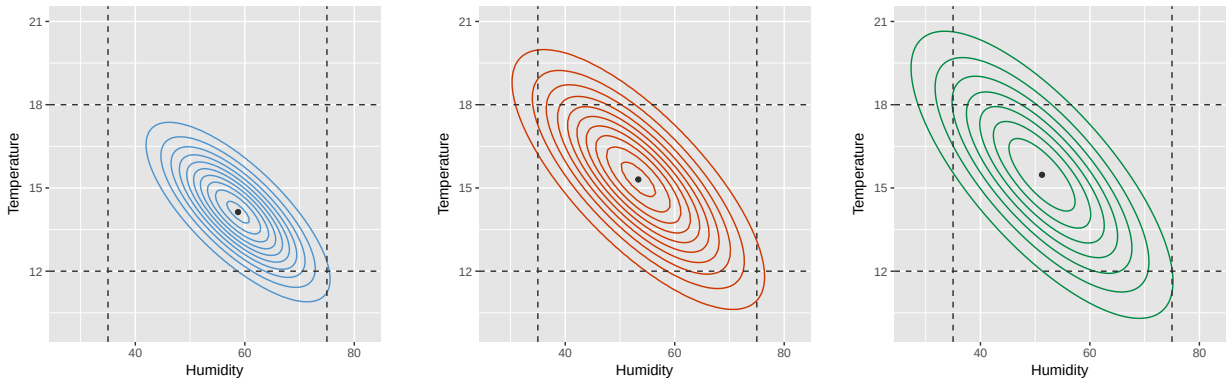


**(a)** one prediction. **(b)** 5 predictions. **(c)** 20 predictions.

**Figure 6.7:** Three instances with their respective densities when predicting $1$, $5$ or $20$ hours ahead with the Kalman filter and ending at the same time. The dashed lines are the two intervals, $[\xi_{T_1}, \xi_{T_2}]$ and $[\xi_{H_1}, \xi_{H_2}]$ presented in Figure 6.6, and are used when predicting the probability in Equation (6.5).

much. Nevertheless, increasing number of consecutively predictions above $5$ will only occur with small values of $\Lambda_{\text{Prediction}}$ because of the large uncertainty.

To validate the monitoring performance Algorithm 1 is used with constraint from Equation (6.5) with chosen criteria for $\Lambda_{\text{Prediction}} = 0.8$. The boundaries as presented in Figure 6.6 still applies in this constraint. The other thresholds, $\lambda_1$ and $\lambda_2$, are the same as presented in Figure 6.1 and Section 6.1.1. The red and green dots from Figure 6.1 and Table 6.2 are also presented in the following figures to demonstrate the performance. The results after monitoring with these constraints can be seen in Figure 6.8 and 6.9, with respectively the performance on temperature and humidity, and the development on battery during monitoring and increased status on transferred energy.

The objective in this section is constructed to keep prediction accuracy at a stable level and measure observations only when the temperature and humidity are expected to be outside the boundaries. Thus, the performance of temperature and humidity in Figure 6.8 should follow the real values more closely than in Figure 6.3, and also keep the uncertainty small. This is actually the case as the green dots are fewer and more separate with this objective. For comparison, the RSS for temperature and humidity in this scenario is $\text{RSS}_{\text{Temp}} = 108.83$ and $\text{RSS}_{\text{Humi}} = 3221.84$, which is remarkably reduced. As threshold (6.5) do not consider explicitly the battery status, the battery performance in Figure 6.9 decrease at several situations. Additionally, even though the amount of red points is high for both objectives the amount of transferred energy is remarkably reduced when comparing with Figure 6.4. In Figure 6.4 the total amount of transferred energy is above $100$ while the amount in Figure 6.9 rarely reaches $30$.

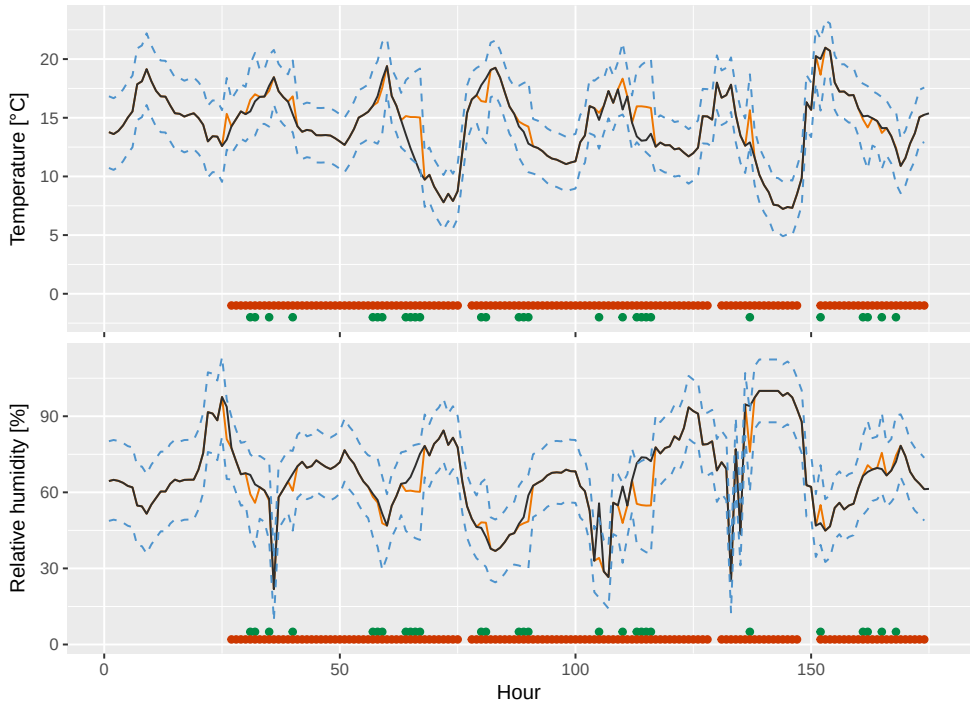


**Figure 6.8:** Predicted temperature and relative humidity plotted in orange with a 95% prediction interval presented in dotted blue lines. The black line is the real data collected from the solar panel. The red and green circles represent the decisions presented in Figure 6.1 and Table 6.1.

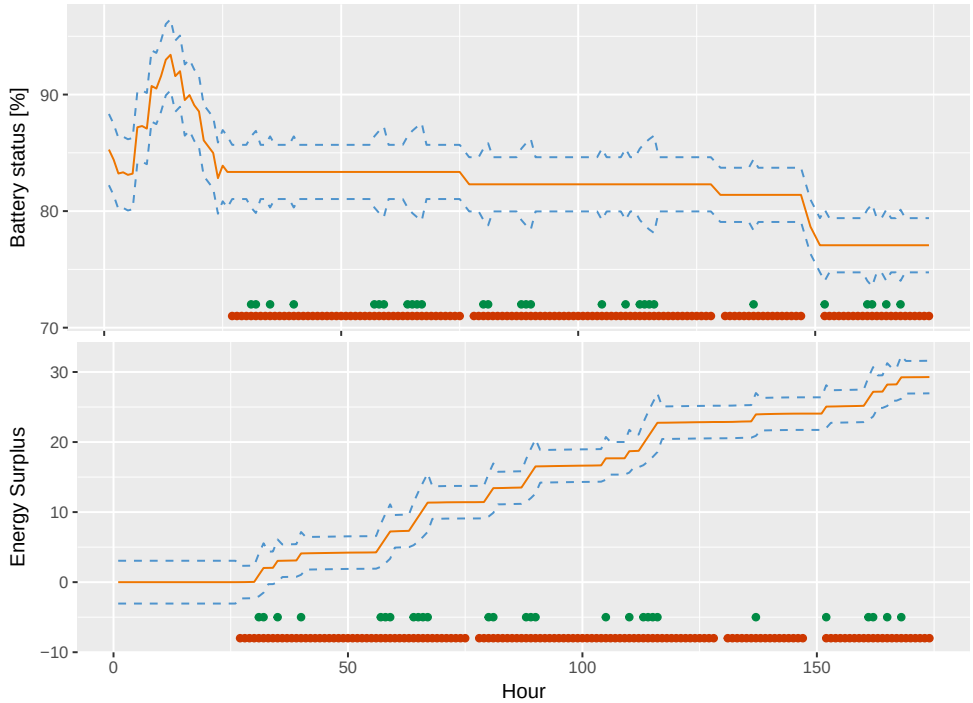


**Figure 6.9:** Behaviour of the battery when threshold (6.2) and (6.4) are used as activation threshold. Orange line in the upper plot is assumed battery status while lower plot is the development of accumulated energy surplus. Dotted blue lines are 95% prediction interval computed from the variance of the temperature. The red and green circles represent the decisions presented in Figure 6.1 and Table 6.1.

## 6.2 Multicriteria Constraint

The two scenarios presented in Section 6.1.1 and 6.1.2 both look at two relevant goals *i)* to obtain energy output, and *ii)* to keep the certainty in the model. It was specified that they both obtain their required objective, however, because of that, they disregard some other relevant requirements. The two models combined together in a multicriteria constraint investigate the possibility to hold a trustworthy model at the same time as obtaining energy surplus. A weighted average $\alpha$ and $(1-\alpha)$ multiplied to the two objectives in the multicriteria constraint introduce the possibility to investigate different performances with respect to *i)* and *ii)*. The principles from the decision tree in Figure 6.1 are used, here $\Lambda = \Lambda_{\text{Multi}}$, and $\lambda_1$ and $\lambda_2$ are as presented in Section 6.1.1.

In Section 6.1.1 and 6.1.2 the output from Equation (6.2) and (6.5) is either TRUE or FALSE. This is not applicable when multiplying with weights. Thus, they have to be transformed into a numeric value to verify if the threshold should be activated. In Equation (6.5) the output is a probability with values between $[0, 1]$, while the interval in Equation (6.2) is $[0.92, 1.02]$. The latter instance is mapped to the first interval and applied to the weighted average. With this adjustment the inequality and multicriteria constraint becomes,

$$\alpha \frac{X_{\text{Bat}_1}/X_{\text{Bat}_2} - 0.92}{1.02 - 0.92} + (1-\alpha)X_{\text{Prob}} \leq \Lambda_{\text{Multi}}. \tag{6.6}$$

Here $X_{\text{Bat}_1}$, $X_{\text{Bat}_2}$ and $X_{\text{Prob}}$ are computed as presented in Equation (6.2) and (6.5) with the same interval for $\xi_{\text{T}}$ and $\xi_{\text{H}}$. The constraints presented in this section have threshold $\Lambda_{\text{Multi}} = 0.8$. However, the threshold could be selected to be any value between $[0, 1]$. Additionally, $\alpha \in [0, 1]$ is the weight that carry out the trade-off between battery surplus and prediction accuracy, i.e. $\alpha = 0.8$ would weight energy surplus as more important.

The suggested multicriteria constraint in Equation (6.6) is added in Algorithm 1. Three cases with different values of $\alpha = 0.2,\ 0.5$ and $0.8$ have been computed and their performances are presented in Table 6.2, along with the results from Section 6.1.1 and 6.1.2 with $\alpha = 0.0,\ 1.0$. To verify their performance different realisations have been computed such as the RSS for

**Table 6.2:** Table presenting the results after monitoring over 150 time steps. RSS is computed from Equation (4.19), Battery and $X_{\text{Surplus}}$ are computed as presented in Section 6.1.1 and # for respectively Predictions and Transfers are the colouring from Table 6.1.

| $\alpha$ | **0.0** | **0.2** | **0.5** | **0.8** | **1.0** |
|---|---|---|---|---|---|
| $\text{RSS}_{\text{Temp}}$ | 108.83 | 76.29 | 156.34 | 148.94 | 881.42 |
| $\text{RSS}_{\text{Humi}}$ | 3221.84 | 2383.63 | 2373.54 | 3142.04 | 90207.68 |
| Battery | 77.07 | 77.31 | 81.35 | 78.62 | 82.26 |
| $X_{\text{Surplus}}$ | 29.28 | 23.36 | 21.39 | 34.21 | 103.47 |
| #Predictions | 28.00 | 22.00 | 22.00 | 36.00 | 104.00 |
| #Transfers | 140.00 | 140.00 | 44.00 | 142.00 | 146.00 |

temperature and humidity, final status on battery and total accumulated energy surplus when reaching iteration length $T$. To see the performance on the different monitoring schemes see Appendix A.

The total performance on #Transfers is mostly the same for all instances except for $\alpha = 0.5$ and correspond to the number of energy transfers represented as the red dots in Figure 6.3 and 6.8. A model with $\alpha = 0.5$ would preferably add measurements, and still get surplus of energy, as the increase in the battery is greater than the use of measurements. With $\text{RSS}_{\text{Humi}} = 2373.54$ and $\text{RSS}_{\text{Temp}} = 156.34$ the performance in the latter RSS is actually worse than monitoring with $\alpha = 0.8$. Even though the final battery percentage with weight on the battery is more reduced than with $\alpha = 0.5$ the amount of energy surplus is higher and fulfilling its purpose from Equation (6.6). Nevertheless, the monitoring model with $\alpha = 0.8$ seems to miss some of the behaviours as the battery is reduced to $78\%$, and in several decisions, the model should have selected the predictive model.

Looking at the model with smallest value on $\text{RSS}_{\text{Temp}}$ and $\text{RSS}_{\text{Humi}}$ this is with $\alpha = 0.2$ and it is expected that the monitoring performance for this model is better. Monitoring with $\alpha = 0.0$ is actually worse than with $\alpha = 0.2$. Surprisingly, the energy surplus with $\alpha = 0.2$ is greater than monitoring with $\alpha = 0.5$, which actually is the model with the lowest surplus of all constraints. It can be noted that the performance between $\alpha = 0.8$ and $\alpha = 1.0$ for all computed results is very disparate. Hence, to obtain large amount of energy surplus, with $\Lambda_{\text{Multi}} = 0.8$, it requires an $\alpha$ close to 1. Without looking at $\alpha = 1$, the predictive error represented with the averaged RSS from the other constraints never reaches $2000$. Hence, it can be assumed that a model with $\text{RSS}_{\text{Avg}} > 50000$ would not give enough prediction accuracy. From observations in Table 6.2 it appears that there are several options to consider when finding the optimal weight of $\alpha$ and it would be difficult to draw a conclusion from this table.

## 6.3 Comparing Models

Considering the multicriteria optimisation in Section 6.2, performance of constraints with different designated $\alpha$ can be seen in Table 6.2. It is difficult to draw a conclusion which model would be the preferred and the optimal size of $\alpha$. Nevertheless, it is possible to define objectives that can give guidance in finding optimal solutions. It would depend on the decision makers preferences, preferred energy surplus or accuracy. With respect to prediction accuracy, the criteria can be focused on RSS for temperature and humidity, and energy output would be represented by the accumulated energy surplus. Thus, the requirements become,

$$\min \quad \text{RSS}_{\text{Temp}} \tag{6.7}$$

$$\min \quad \text{RSS}_{\text{Humi}} \tag{6.8}$$

$$\max \quad \text{Energy Surplus.} \tag{6.9}$$

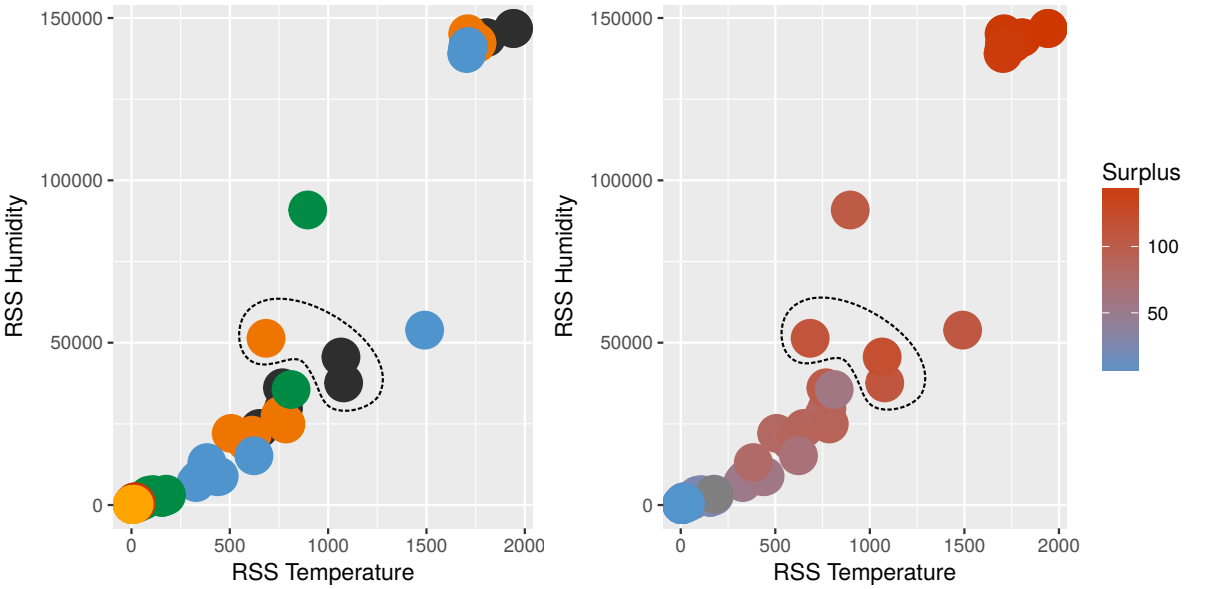


**Figure 6.10:** Results after monitoring with different values of $\alpha$ and $\Lambda_{\text{Multi}}$. Each graph have used Equation (6.6) with different values of $\alpha = 0, 0.1, \ldots, 0.9, 1$. Left: The values used as a threshold are $\Lambda_{\text{Multi}} = 0.5, 0.6, 0.7, 0.8, 0.9, 1.0$ and have colours; black(0.5), orange(0.6), blue(0.7), green(0.8), red(0.9) and yellow(1.0). Right; The colouring corresponds to total surplus after monitoring with red as the highest and blue with the lowest amount.

To verify the performance of the monitoring over $150$ time steps different values of $\alpha$ and $\Lambda_{\text{Multi}}$ are used and plotted in Figure 6.10. In this figure, the realisation from $\text{RSS}_{\text{Temp}}$ and $\text{RSS}_{\text{Humi}}$ are plotted against each other. Each colour corresponds to different threshold values computed with an increasing value of $\alpha = 0, 0.1, \ldots, 0.9, 1$. The threshold is managed for $\Lambda_{\text{Multi}} = 0.5, 0.6, 0.7, 0.8, 0.9$. Additionally, to verify which constraint is optimal when also looking at energy surplus a density plot with graded colouring can be seen in the right Figure.

The desired model could have requirements purely on prediction accuracy and would prefer a model to the bottom left corner. However, the best results with respect to the maximum and minimum objectives seem to be the three constraints plotted inside the dotted black circle, which also keeps the assumed requirements on $\text{RSS}_{\text{Avg}} < 50000$. It can be seen that there are different values for threshold $\Lambda_{\text{Multi}}$, and when studying their respective $\alpha$ they are also different. The results are with,

$$\text{Black}_1: \quad \Lambda_{\text{Multi}} = 0.5, \quad \alpha = 0.3 \tag{6.10}$$

$$\text{Black}_2: \quad \Lambda_{\text{Multi}} = 0.5, \quad \alpha = 0.4 \tag{6.11}$$

$$\text{Orange}: \quad \Lambda_{\text{Multi}} = 0.6, \quad \alpha = 0.5. \tag{6.12}$$

Thus, it appears that there are more than one monitoring that could give results to consider further. These thresholds, with their respective values for $\alpha$, seem to be the best results when solely considering the three objectives, RSS and energy surplus from Figure 6.10.

The performance of the monitoring in Equation (6.10), (6.11) and (6.12) have the same problem as was discussed in Section 6.1.1, the predictions do not follow the real data. Figure A.7, A.9 and A.11 are included in the Appendix A for a completeness of verification. This problem was also presented when discussing the prediction accuracy in Section 6.1.2, a large number of consecutively predictions will occur with small values of $\Lambda_{\text{Multi}}$ because this will allow for large uncertainties. Small threshold values is a mutual incident for the three constraints. Hence, it is advised to find a model with less prediction error, however, this will give a reduced amount of energy surplus.

Another method of visualising performances is presented in Figure 6.11. In this figure, the averaged RSS of temperature and humidity is computed and plotted against total energy surplus. The black circle presented in Figure 6.10 encircle the same points with $\Lambda_{\text{Multi}} = 0.5$, and are presented to visualise the change on the axis. From Table 6.2 and Figure 6.10 it is seen that the RSS for temperature and humidity are disparate. Hence, their respective RSS will not represent the same magnitude of the error. To verify the best performance a situation that would be similar to a Pareto optimal solution is studied, as we have two objective functions and a trade-off is needed to find the preferred solution. A preferred model would maintain the premise with a larger $\Lambda_{\text{Multi}}$ and have $\text{RSS}_{\text{Avg}} < 50000$. Hence, with respect to maximising energy output and minimising prediction error, the most preferable result is encircled with a dashed red line and have $\Lambda_{\text{Multi}} = 0.7$ and $\alpha = 0.4$. A presentation of this monitoring is displayed in Figure 6.12 and 6.13. It can be seen that with this constraint the predictions do

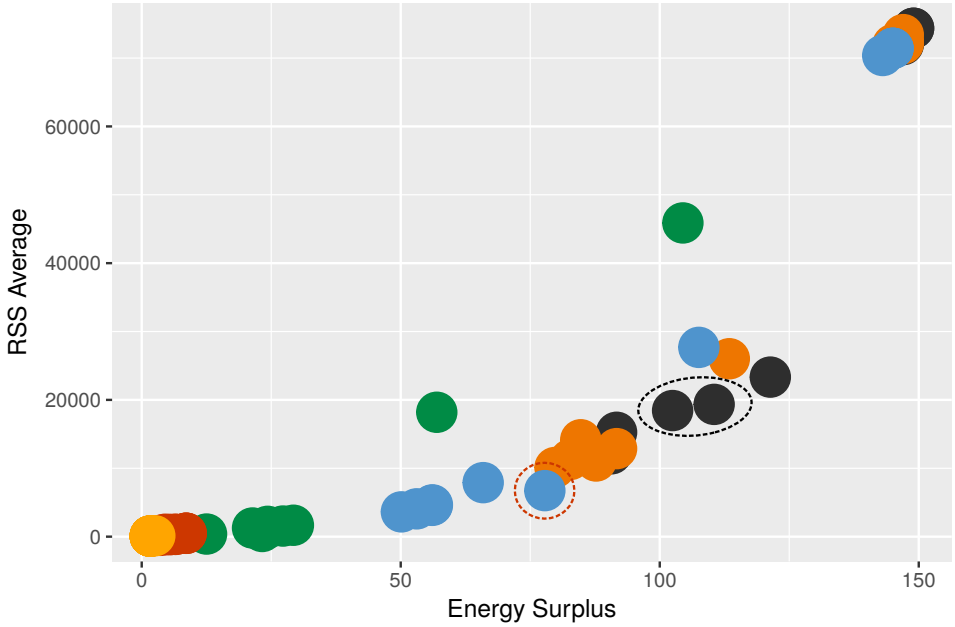


**Figure 6.11:** Averaged RSS with temperature and humidity are plotted against amount of transferred energy. Colours correspond to the same instances as presented in Figure 6.10, and the dashed black circle encircle the same points in this figure. Red dashed circle encircle the model with $\Lambda_{\text{Multi}} = 0.7$ and $\alpha = 0.4$.

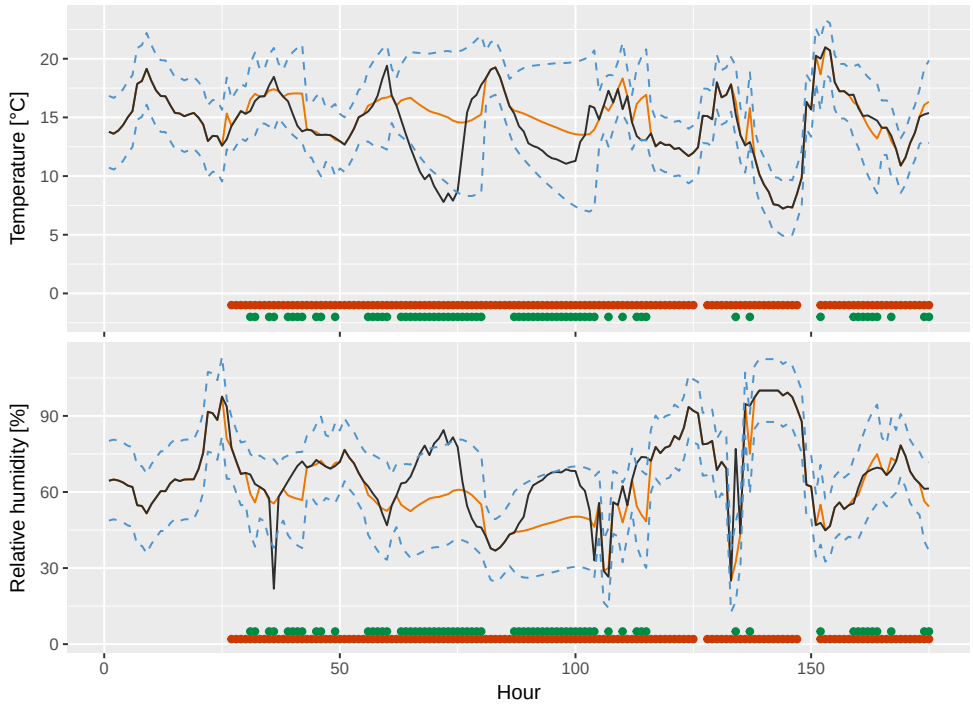


**Figure 6.12:** Predicted temperature and relative humidity plotted in orange with a 95% prediction interval presented in dotted blue lines. The black line is the real data collected from the solar panel. The red and green circles represent the decisions presented in Figure 6.1 and Table 6.1.

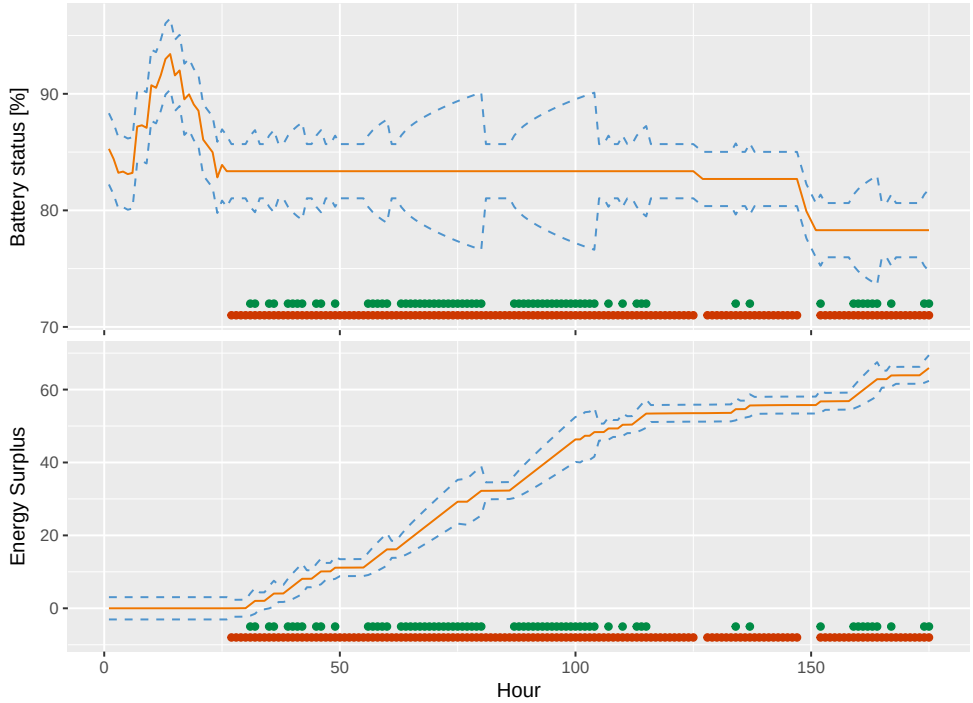


**Figure 6.13:** Behaviour of the battery when threshold (6.2) and (6.4) are used as activation threshold. Orange line in the upper plot is assumed battery status while lower plot is the development of accumulated energy surplus. Dotted blue lines are 95% prediction interval computed from the variance of the temperature. The red and green circles represent the decisions presented in Figure 6.1 and Table 6.1.

not capture all of the behaviour withing the boundary that were presented in Section 6.1.2, but it decides to measure observations when the probability of staying within the boundary is too low. The general performance is acceptable with $\text{RSS}_{\text{Avg}} = 7898.6$ and the accumulated energy surplus as $65.9$.

The obvious jump on energy surplus that could be seen in Table 6.2 can also be seen in Figure 6.10 and 6.11. The large amount is obtained when $\Lambda_{\text{Multi}} = 0.5, 0.6, 0.7$. When studying the size on $\alpha$ this high energy surplus is obtained with $\alpha > 0.5$, meaning weighting energy surplus. Additionally, from Equation (6.5) the multivariate probability would only be activated when the probability of staying within the interval is small. Hence, with small $\alpha$ and large $\Lambda_{\text{Multi}}$ this would impose better prediction accuracy. In conclusion, the optimal constraint is dependent on what the preferred goal is, whether this is to obtain a high amount of energy surplus or minimising the predictive error.

Chapter 7

# Closing Remarks

The aim of this thesis was to describe energy efficient monitoring strategies that perform predictions with required certainty and thereby minimises the energy consumption for doing measurements and data savings. These objectives have been combined together into a multicriteria constraint. Because a trade-off between optimal solutions was required, a situation similar to a Pareto optimal solution was considered in this study.

## 7.1 Conclusion

Sensors collect data continuously and share it on platforms that can draw knowledge from it. The idea of monitoring time series online was motivated by discussions about IoT and how to make measurements and information gathering from IoT sensors more energy efficient. The goal was to find methods and develop models restricting devices from doing measurements and data savings repeatedly in a linear fashion, and only saves data from measurements when necessary. Despite limitations on data collection, such a smart model should predict future states satisfactory, thereby optimising the transfer of surplus energy to other instances.

Data collected from solar panels placed at the rooftop at NTNU have been used to construct multivariate time series models for temperature and humidity. The models have been adapted into an on-line monitoring algorithm with predictions computed from a seasonal multivariate Kalman filter. To restrain data collection, the model was able to work as a power management system where we know the operational cost of the system and thus can optimise the energy that can be harvested from the environment.

The two criteria to obtain *i)* energy surplus and *ii)* prediction accuracy have been combined together into a multicriteria constraint and a weighted average multiplied to the two objectives indicate what importance to contribute most during the monitoring. This constraint provides information to the event- and self-triggering controls which decide what to do at the current time. Several instances with different weights and triggering controls have been monitored, and the predicted error for temperature and humidity have been compared with the total amount

of transferred energy. The optimal solution would be to obtain maximised energy surplus and minimise the prediction error. However, there were no obvious unique optimal solution and a trade-off between the different monitoring results was considered.

At first it appeared to be three ideal solutions, however, their prediction error was too high and some more constraint on prediction accuracy was considered. Thus, the most optimal constraint was with threshold $\Lambda_{\text{Multi}} = 0.7$ and $\alpha = 0.4$, and obtained averaged Residual Sum of Squares as $\text{RSS}_{\text{Avg}} = 7898.6$ and total energy surplus $65.9$. Moreover, the optimal trigger and weight settings depends on the goals of the decision maker. As an example, there might be energy optimisation in low absorption periods and high amount of data collection in surplus periods.

## 7.2 Further Work

There are several possible extensions of the current work and the monitoring algorithm can be developed further with additional features. With better domain knowledge and technical information about the battery, solar panels and sensor communication, it would have been possible to set more accurate assumptions in the model. It is also possible to consider an extension of the probability boundaries to get a broader specifications for the prediction accuracy.

It was specified in this monitoring that the battery percentage would continuously decrease. This will be challenging when the battery percentage reaches a low percentage. One solution could be to add a threshold when reaching a specific low percentage and force the model to charge until reaching a specified high percentage again. To obtain models that could effectively charge the battery would require more information about the battery characteristics in itself and how temperature and humidity affect the charging status. This also includes knowledge about whether there is some system delay when charging the battery and consuming energy from the environment.

The solar panels placed at NTNU have no possibility to export the accumulated energy surplus to other instances because they are not connected to any other system. Instead, the energy surplus could be utilised for different tasks within the sensor that requires more energy than usual operational cost, for instance collecting more information to develop the model or software update on the sensor. Update on the multivariate seasonal Autoregressive Moving Average model could for instance be to add weather forecasts that could improve the predictions. This would require a new implemented model that weight on accuracy on the included forecasts. It is also possible to increase the sensor network to include multiple sensors. This would require another form of power management, because communication between the nodes would require different workload on the system (Sinha and Chandrakasan, 2001). Based on information obtained from the predictive models the sensor could plan ahead and save energy before carrying out these tasks.

With some of these improvements in place we can foresee the possibility to connect such a

monitoring algorithms into an IoT arrangement serving systems like a smart house (Vinodhan and Vinnarasi, 2016). This would first of all constrain data collection even more and could further save energy, both from reducing operational cost and also because energy surplus in one device could share energy with other devices. Other systems where the communication between sensors is relevant, and data collection have to be managed in order to obtain sustainable operation, could be when monitoring road network either as a traffic management system (Sharif et al., 2018) or winter road maintenance when power supply is decreased (Chapman et al., 2014). In this thesis it has been assumed that there is no energy loss transferring energy. However, in real life this is not the case. Hence, to get a broader understanding of the total amount of transferred energy some additional analysis should be considered. This would especially apply when selecting appropriate models with weight on how to utilise the energy surplus.

# Bibliography

Al-Kuwari, M., Ramadan, A., Ismael, Y., Al-Sughair, L., Gastli, A., Benammar, M., 2018. Smart-home automation using iot-based sensing and monitoring platform. In: Compatibility, Power Electronics and Power Engineering (CPE-POWERENG), 2018 IEEE 12th International Conference on. IEEE, pp. 1–6.

Bandyopadhyay, D., Sen, J., 2011. Internet of things: Applications and challenges in technology and standardization. Wireless Personal Communications 58 (1), 49–69.

Brockwell, P. J., Davis, Richard, D. A., 2002. Introduction to Time Series and Forecasting, 2nd Edition. Springer Texts in Statistics. Springer.

Brockwell, P. J., Davis, R. A., 1991. Time Series: Theory and Methods, 2nd Edition. Springer Texts in Statistics. Springer.

Chapman, L., Young, D., Muller, C., Rose, P., Lucas, C., Walden, J., 2014. Winter road maintenance and the internet of things. In: Proc. 17th Standing Int. Road Weather Commission (SIRWEC) Conf.

Doumpos, M., Zopounidis, C., 2014. Multicriteria Analysis in Finance, 2nd Edition. ProQuest Ebook Central. Springer.

Durbin, J., Koopman, S. J., 2001. Time series analysis by state space methods. Oxford statistical science series. Oxford University Press, Oxford.

Eidsvik, J., Martinelli, G., Bhattacharjya, D., 2017. Sequential information gathering schemes for spatial risk and decision analysis applications. Stochastic Environmental Research and Risk Assessment, 1–15.

Eidsvik, J., Mukerji, T., Bhattacharjya, D., 2015. Value of Information in the Earth Science, 1st Edition. Cambridge University Press.

Everitt, B. S., 2014. The Cambridge Dictionary of Statistics, 3rd Edition. Cambridge University Press.

Grosswindhagera, S., Voigtb, A., Kozeka, M., 2011. Online short-term forecast of system heat load in district heating networks. Tsp 1, 2.

Harvey, A. C., 1990. Forecasting, Structural Time Series Models and the Kalman Filter. Cambridge University Press.

Hastie, T., Tibshirani, Robert, Friedman, J., 2001. The Elements of Statistical Learning. Springer Series in Statistics. Springer New York Inc., New York, NY, USA.

Heemels, W., Johansson, K. H., Tabuada, P., 2012. An introduction to event-triggered and self-triggered control. In: Decision and Control (CDC), 2012 IEEE 51st Annual Conference on. IEEE, pp. 3270–3285.

Härdle, W. K., Simar, L., 2015. Applied Multivariate Statistical Analysis. Springer, Berlin, Heidelberg.

Kansal, A., Hsu, J., Zahedi, S., Srivastava, M. B., Sep. 2007. Power management in energy harvesting sensor networks. ACM Trans. Embed. Comput. Syst. 6 (4).

Madsen, H., 2008. Time Series Analysis, 1st Edition. Chapmann & Hall /CRC Taylor & Francis Group.

Särkkä, S., 2002. Bayesian Filtering and Smoothing, 2nd Edition. Cambridge University Press.

Sharif, A., Li, J. P., Sharif, M. I., Jan 2018. Internet of Things network cognition and traffic management system. Cluster Computing.

Sinha, A., Chandrakasan, A., Mar. 2001. Dynamic power management in wireless sensor networks. IEEE Des. Test 18 (2), 62–74.

Smith, P. J., Arnfield, A. J., et al., 2018. Climate.

Teixeira, T., Hachem, S., Issarny, V., Georgantas, N., 2011. Service oriented middleware for the internet of things: a perspective. Towards a Service-Based Internet, 220–229.

The Norwegian Meteorological Institute and NRK, 2018. Weather statistics for trondheim.

Vinodhan, D., Vinnarasi, A., 2016. Iot based smart home.

Waspmote Technical Guide v7.6, 2018.

Weber, R. H., Weber, R., 2010. Internet of things. Vol. 12. Springer.

Wei, W. W., 1985. Inverse and partial lag autocorrelation for vector time series. In: Proceedings of the Business and Economic Statistics Section. The Association, p. 233.

Wei, W. W., 2006. Time Series Analysis: univariate and multivariate methods, 2nd Edition. Pearson Education.

Xu, B., Da Xu, L., Cai, H., Xie, C., Hu, J., Bu, F., 2014. Ubiquitous data accessing method in iot-based information system for emergency medical services. IEEE Transactions on Industrial Informatics 10 (2), 1578–1586.

Appendix A

# Appendix

## A.1 Multicriteria Constraints

### A.1.1 Equally Weighted

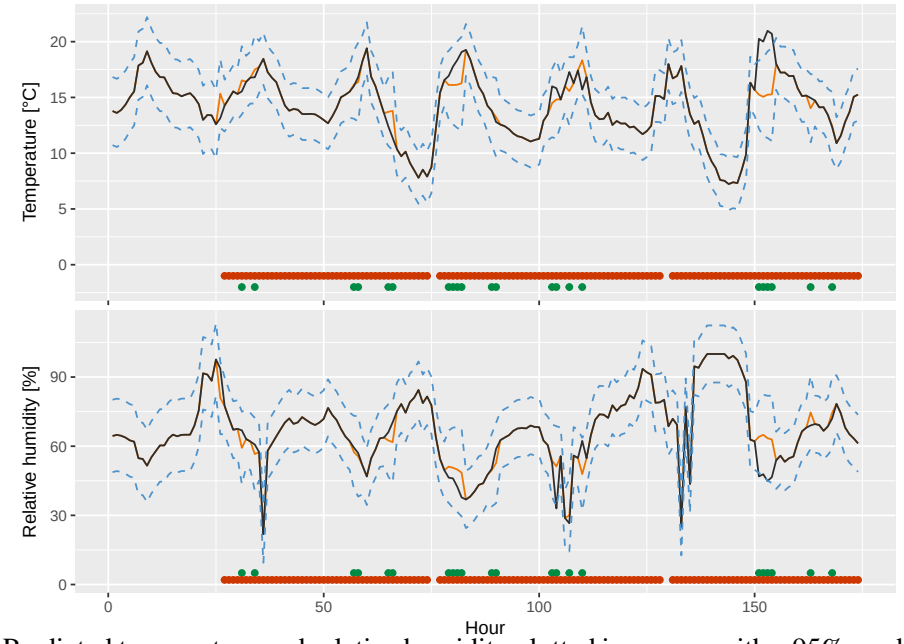


**Figure A.1:** Predicted temperature and relative humidity plotted in orange with a 95% prediction interval presented in dotted blue lines. The black line is the real data collected from the solar panel. The red and green circles represent the decisions presented in Figure 6.1 and Table 6.1.

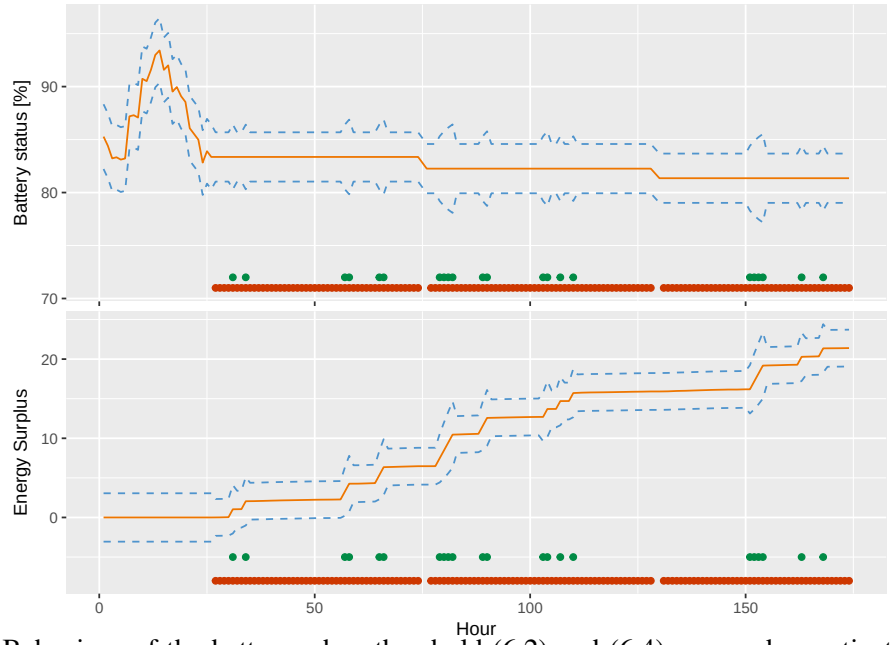


**Figure A.2:** Behaviour of the battery when threshold (6.2) and (6.4) are used as activation threshold. Orange line in the upper plot is assumed battery status while lower plot is the development of accumulated energy surplus. Dotted blue lines are 95% prediction interval computed from the variance of the temperature. The red and green circles represent the decisions presented in Figure 6.1 and Table 6.1.

### A.1.2 Weight on Energy Surplus

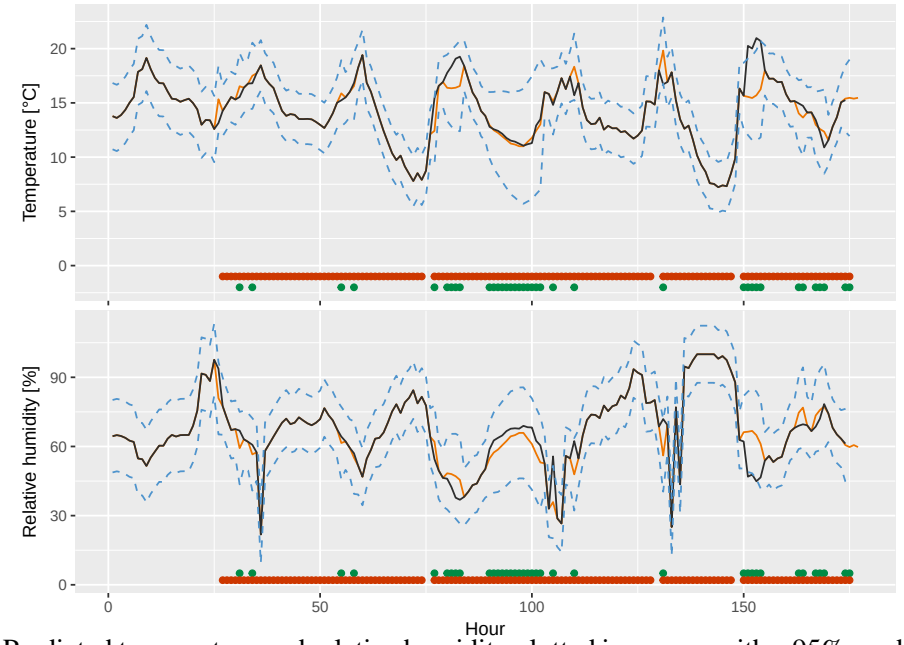


**Figure A.3:** Predicted temperature and relative humidity plotted in orange with a 95% prediction interval presented in dotted blue lines. The black line is the real data collected from the solar panel. The red and green circles represent the decisions presented in Figure 6.1 and Table 6.1.

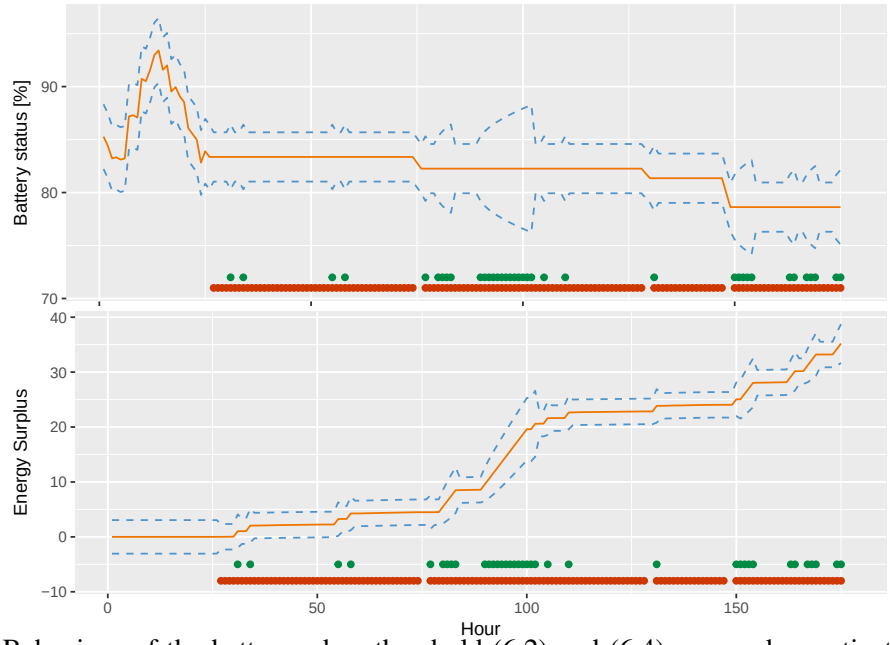


**Figure A.4:** Behaviour of the battery when threshold (6.2) and (6.4) are used as activation threshold. Orange line in the upper plot is assumed battery status while lower plot is the development of accumulated energy surplus. Dotted blue lines are 95% prediction interval computed from the variance of the temperature. The red and green circles represent the decisions presented in Figure 6.1 and Table 6.1.

### A.1.3 Weight on Prediction Accuracy

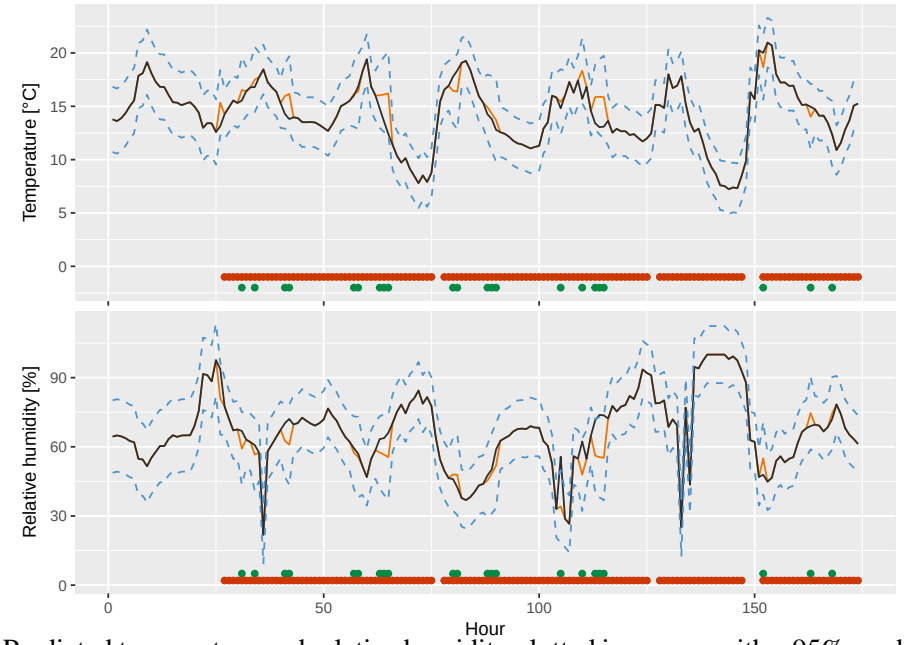


**Figure A.5:** Predicted temperature and relative humidity plotted in orange with a 95% prediction interval presented in dotted blue lines. The black line is the real data collected from the solar panel. The red and green circles represent the decisions presented in Figure 6.1 and Table 6.1.

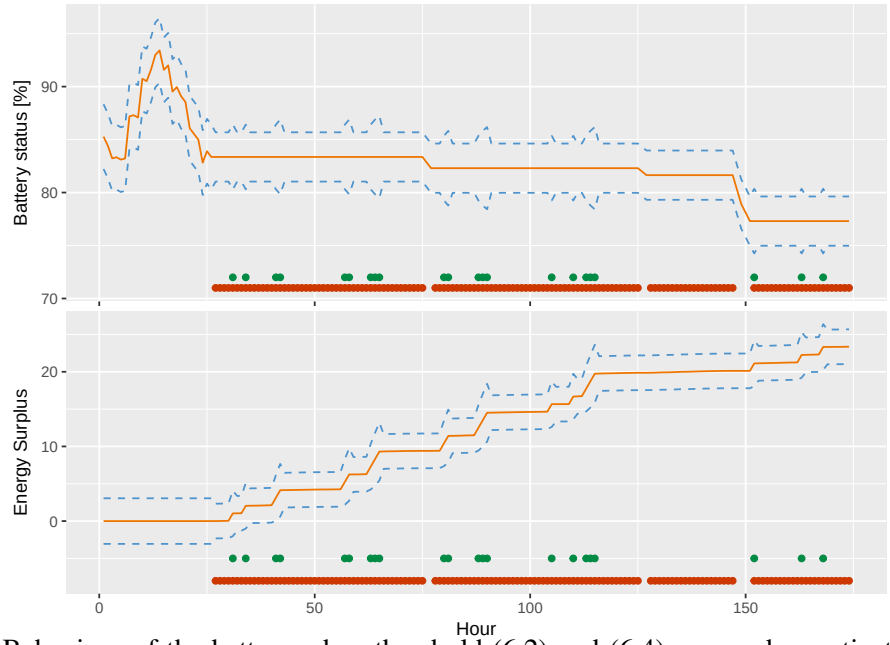


**Figure A.6:** Behaviour of the battery when threshold (6.2) and (6.4) are used as activation threshold. Orange line in the upper plot is assumed battery status while lower plot is the development of accumulated energy surplus. Dotted blue lines are 95% prediction interval computed from the variance of the temperature. The red and green circles represent the decisions presented in Figure 6.1 and Table 6.1.

## A.2 Comparing Models

### A.2.1 Optimal with $\Lambda_{\textbf{Multi}} = 0.5$ and $\alpha = 0.3$

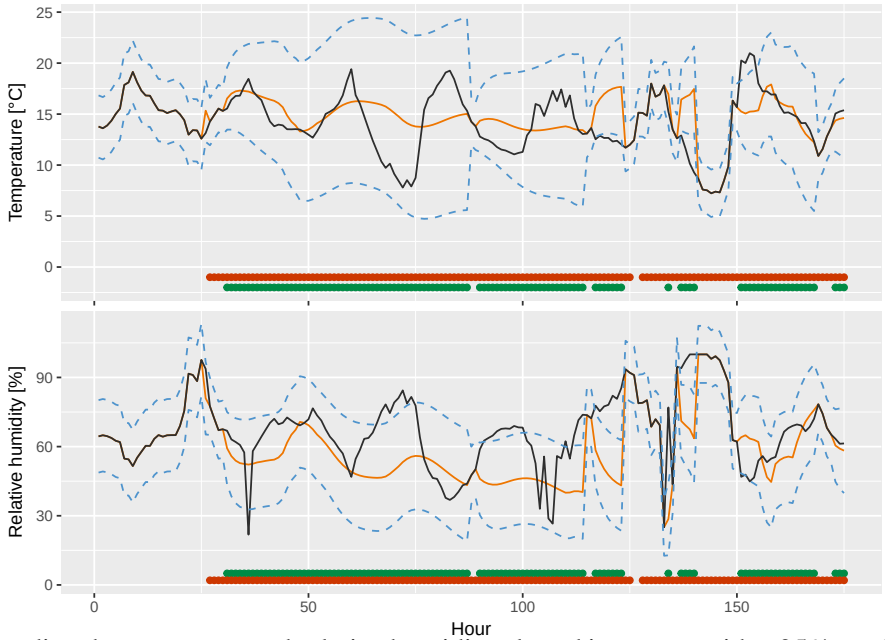


**Figure A.7:** Predicted temperature and relative humidity plotted in orange with a 95% prediction interval presented in dotted blue lines. The black line is the real data collected from the solar panel. The red and green circles represent the decisions presented in Figure 6.1 and Table 6.1.

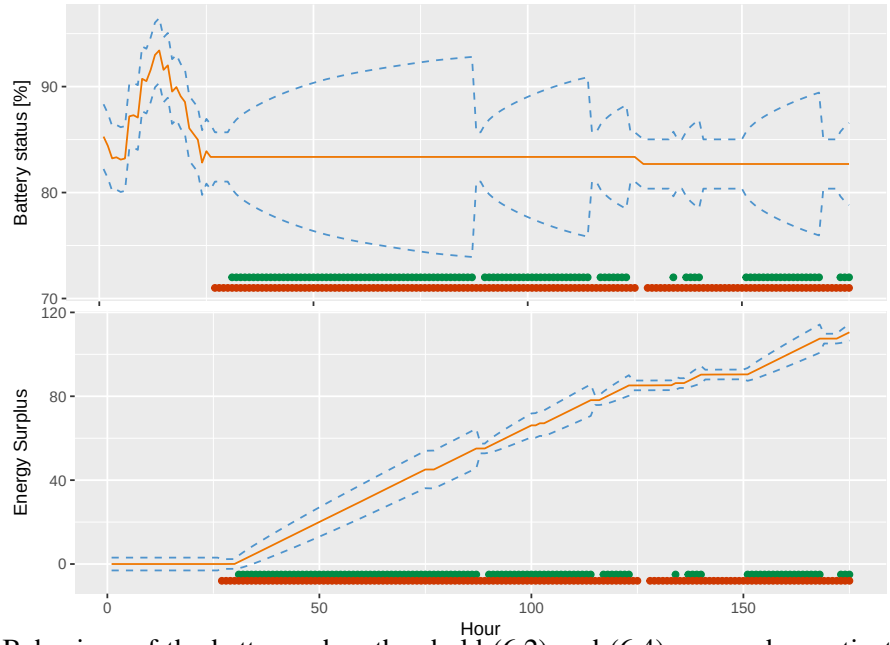


**Figure A.8:** Behaviour of the battery when threshold (6.2) and (6.4) are used as activation threshold. Orange line in the upper plot is assumed battery status while lower plot is the development of accumulated energy surplus. Dotted blue lines are 95% prediction interval computed from the variance of the temperature. The red and green circles represent the decisions presented in Figure 6.1 and Table 6.1.

### A.2.2 Optimal with $\Lambda_{\text{Multi}} = 0.5$ and $\alpha = 0.4$

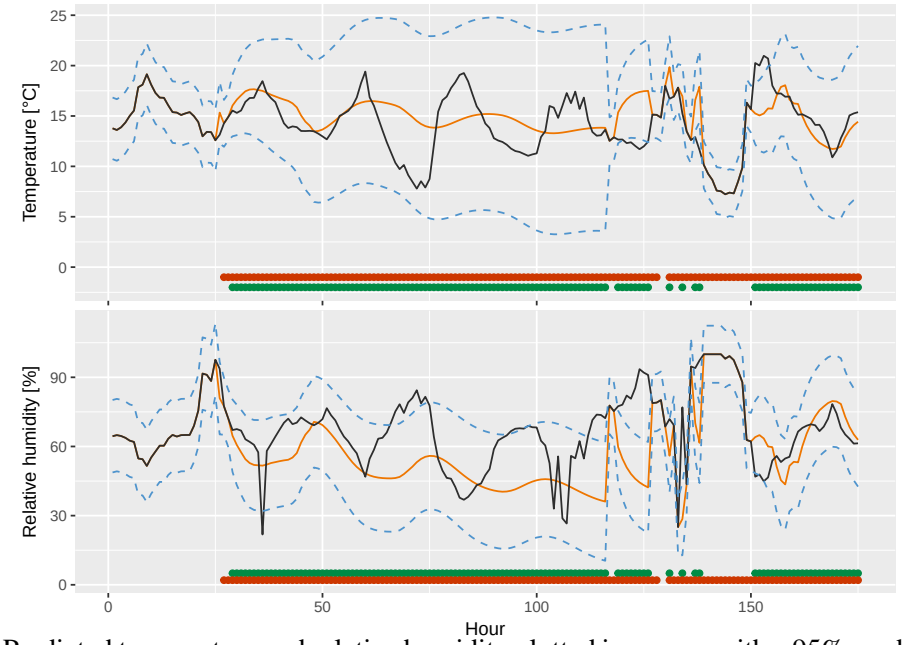


**Figure A.9:** Predicted temperature and relative humidity plotted in orange with a 95% prediction interval presented in dotted blue lines. The black line is the real data collected from the solar panel. The red and green circles represent the decisions presented in Figure 6.1 and Table 6.1.

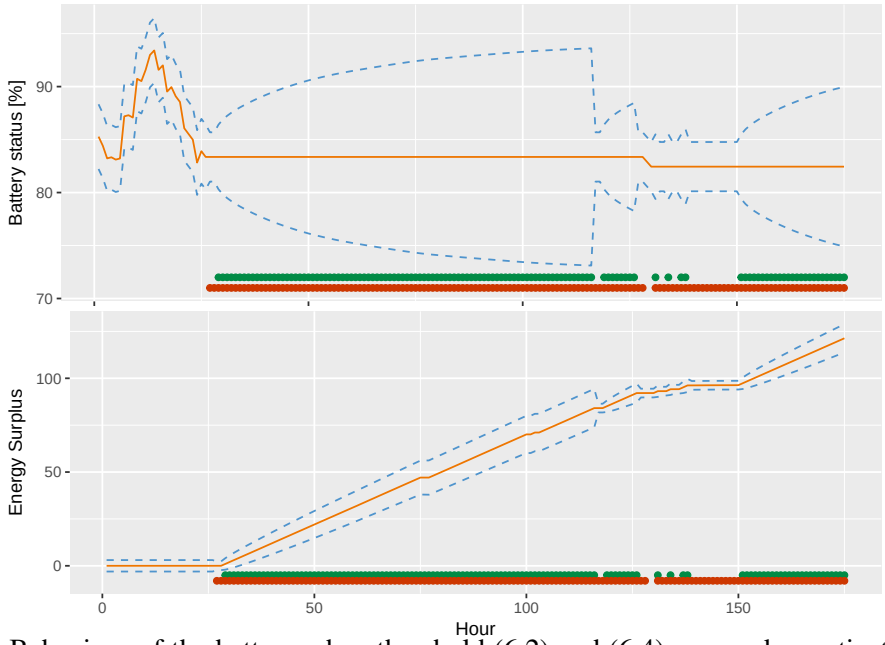


**Figure A.10:** Behaviour of the battery when threshold (6.2) and (6.4) are used as activation threshold. Orange line in the upper plot is assumed battery status while lower plot is the development of accumulated energy surplus. Dotted blue lines are 95% prediction interval computed from the variance of the temperature. The red and green circles represent the decisions presented in Figure 6.1 and Table 6.1.

### A.2.3 Optimal with $\Lambda_{\text{Multi}} = 0.6$ and $\alpha = 0.5$

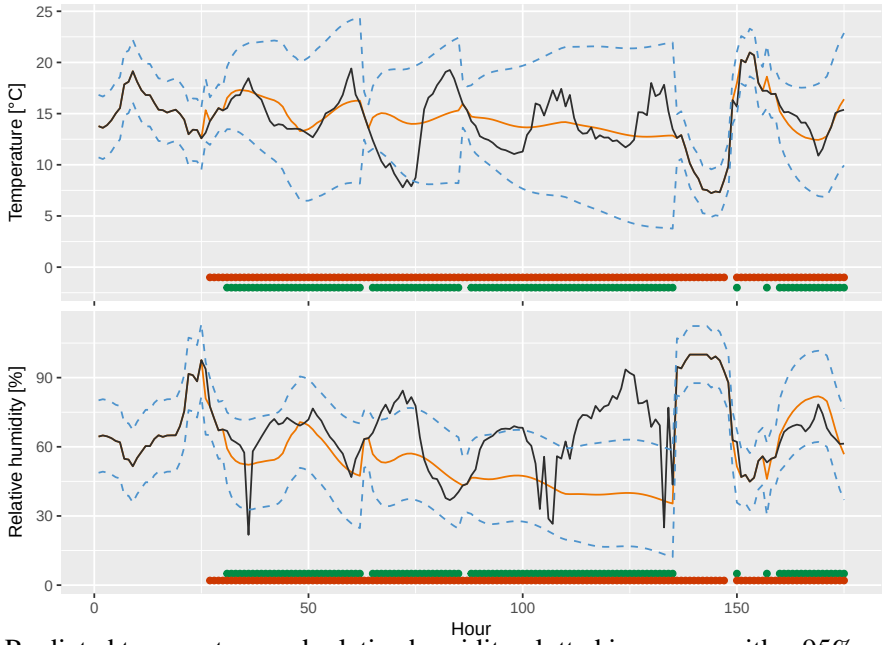


**Figure A.11:** Predicted temperature and relative humidity plotted in orange with a 95% prediction interval presented in dotted blue lines. The black line is the real data collected from the solar panel. The red and green circles represent the decisions presented in Figure 6.1 and Table 6.1.

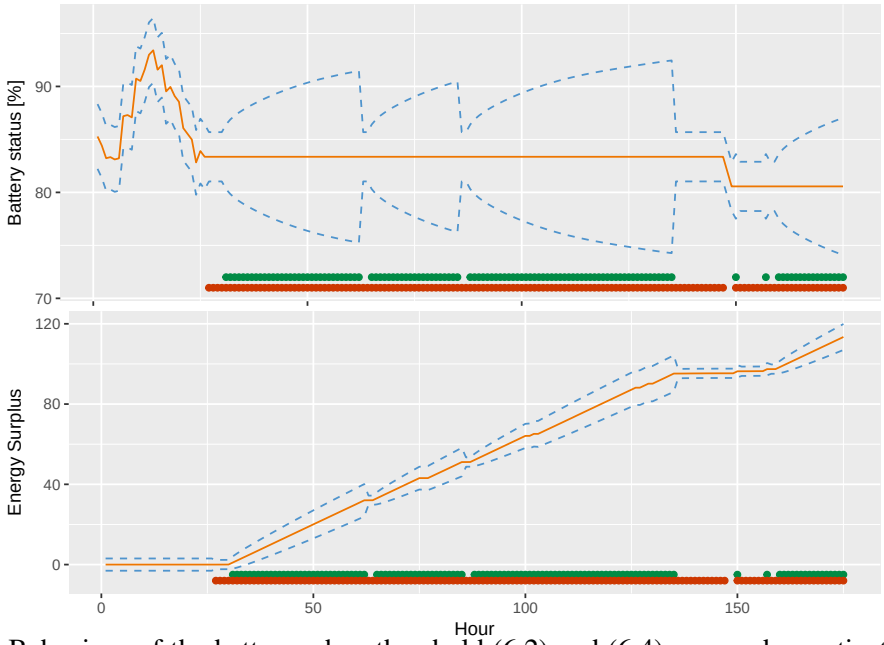


**Figure A.12:** Behaviour of the battery when threshold (6.2) and (6.4) are used as activation threshold. Orange line in the upper plot is assumed battery status while lower plot is the development of accumulated energy surplus. Dotted blue lines are 95% prediction interval computed from the variance of the temperature. The red and green circles represent the decisions presented in Figure 6.1 and Table 6.1.